AN ABSTRACT OF THE DISSERTATION OF

Lei Chen for the degree of Doctor of Philosophy in Chemistry presented on March 1, 2016.

Title: Catching Ions in Superfluid Helium Droplets

Abstract approved:

_____

Wei Kong

In this dissertation, I describe the experimental investigation of catching ions in superfluid helium droplets. The ultimate goal of our project is to build a coherent electron diffraction apparatus for atomic structure determination from oriented single macromolecules. This involves generating protein ions from electrospray ionization (ESI) and doping them in helium droplets. The doped droplets are then oriented by an elliptically polarized laser and exposed to a coherent electron beam for diffraction. The specific goal of my project is to explore the methods for sample preparation. I have started by exploring the doping conditions for continuous cesium ions from a thermionic emission source and then moved on to pulsed ions from an ESI source. I have also characterized the size and size distribution of the doped droplets. The relative ion doping efficiency of the continuous cesium ions is determined by both the kinetic energy of the ions and the size of the droplets. For reserpine and substance P from the ESI source, we have succeeded with a simple experimental setup by stopping the ions in the droplet beam with a DC bias. The resulting doping efficiency

is observed to scale with the residence time of the ion beam in the droplet beam. To further control the size of the ion doped droplets for diffraction, I also have performed an exploratory experiment of collisional size reduction of ion doped droplets. These exercises and the resulting theoretical understanding of the doping mechanism of cations in superfluid helium droplets will be fundamental for the next stage of the overall project.

Catching Ions in Superfluid Helium Droplets

by

Lei Chen

A DISSERTATION

submitted to

Oregon State University

in partial fulfillment of
the requirements for the
degree of

Doctor of Philosophy

Presented March 1, 2016
Commencement June 2016

Doctor of Philosophy dissertation of Lei Chen presented on March 1, 2016

APPROVED:

Major Professor, representing Chemistry

Chair of the Department of Chemistry

Dean of the Graduate School

I understand that my dissertation will become part of the permanent collection of Oregon State University libraries. My signature below authorizes release of my dissertation to any reader upon request.

Lei Chen, Author

ACKNOWLEDGEMENTS

During the past six years' study for my Ph. D in chemistry, there are many people I would like to acknowledge for helping me to finish this difficult but invaluable challenge.

Firstly, I would like to express my sincere appreciation to my advisor Professor Wei Kong for her patience, motivation and willingness to answer all my questions. She is always supportive and encouraging with my study, research as well as the writing of this thesis. Her advice on my research and my life has been invaluable.

I also would like to thank Dr. Jie Zhang. She helped me to familiarize with the lab and guided me in research and problem solving. My special thanks also go to my lab mates: Dr. Colin Harthcock and Mr. Yunteng He. They are always willing to help. Specially, I would like to acknowledge Bill Freund who helped me design complicated parts and make functional electronic circuits. I also would like to thank Dr. Valery Voinov who supported and guided my research on mass spectrometry. Of course, without Larry's help, I cannot have those delicate parts out of thin air.

I would also like to thank my thesis committee: Dr. Chong Fang, Dr. Sean Burrows and Dr. William Warnes for their insightful comments and advice.

Finally, I would like to acknowledge the support of my family. Thanks to my parents, my husband and my daughter. They have always encouraged me to pursue the difficult challenges and they brought the sunshine into my life.

TABLE OF CONTENTS

Page

TABLE OF CONTENTS (Continued)

Page

TABLE OF CONTENTS (Continued)

Page

TABLE OF CONTENTS (Continued)

Page

LIST OF FIGURES

LIST OF FIGURES (Continued)

LIST OF FIGURES (Continued)

LIST OF TABLES

Table Page

Chapter 1 Introduction

1.1 Motivation

Structural properties and folding dynamics of biological molecules are of central importance to the understanding of their physiological functions, pertaining to health, aging, disease, and healing. For example, more than 50% of all modern drugs have been developed based on knowledge of three-dimensional (3D) structures of membrane proteins.[1] Although with the progress in the field of proteomics and genomics, the primary structure of almost all biological molecules can be determined, we still do not possess the knowledge of calculating the 3D structures of most proteins based on their primary structure. On the other hand, misfolding is considered a key step in a series of neurodegenerative diseases, including the mad cow disease, Parkinson's disease, and Alzheimer's disease.[2]

Experimental measurements of protein 3D structures constitute a major branch of research activities in biological research. To date, of all the proteins in a human body, about 6% has been structurally determined using a gamut of techniques, and the lion's share, more than 88% of the structures deposited in the protein databank, are determined by X-ray diffraction (XRD) of three-dimensional crystals.[3] Other methods suffer considerably more constraints and are hence less productive. For example, cryo-electron microscopy (cryo-EM) has been rapidly developed in recent years. However, it still suffers from severe radiation damage and hence offers limited resolution.[4] As a spectroscopic technique, nuclear magnetic resonance (NMR)

is advantageous in several ways, but ultimately, it has limited usage for large sized proteins due to the difficulty in data interpretation. Currently, the molecular weight limit of NMR is about 100 kDa.

The technique of X-ray crystallography has had a history of over half a century. It relies on the Bragg diffraction of single crystals for structure determination. Although conceptually the technique is still burdened with the "phase problem",[5] with the advent of computers, the introduction of synchrotron radiation sources, and the invention of many experimental approaches, this problem is practically solved. The remaining issue that limits the progress of XRD is the availability of single crystals. This problem is particularly salient for proteins because crystallization is unpredictable if possible at all for many large fragile biological molecules.

To fundamentally circumvent the crystallization problem, to achieve crystallography without crystals, researchers have explored two general methods, relying on coherent diffraction of non-periodical systems – single molecules.[6-7] Non-crystalline samples generate speckled continuous Fraunhofer diffraction patterns instead of discrete Bragg diffraction patterns. In the early 1980s, methods to reconstruct the sample structure, including the algorithm of phase retrieval via oversampling, have been developed.[6-9] In 1999, Miao *et al*[10] investigated the X-ray diffraction pattern of a non-crystalline gold nanoparticle by using this oversampling method, demonstrating for the first time the possibility of this general approach.

Following the work by Miao et al, in 2000, Neutze *et al*[7] proposed the "diffract and destroy" approach for single molecules by relying on intense X-ray sources such as X-ray free electron lasers (XFEL). The authors proposed that sufficient diffraction information can be obtained from a single femtosecond X-ray pulse before the protein molecules or small assemblies are destroyed in the radiation field. Compared with a conventional light source, an XFEL produces a larger number of photons focused on a sample and squeezes time into a few femtoseconds, which efficiently assists with the study of dynamics of atomic and molecular processes. Later, Fratalocchi and Ruocco[11] showed that given the current level of radiation from a contemporary XFEL, attosecond pulses are required for single molecule diffraction.

Another method has been proposed by Spence and Doak[6] in 2004, similar to the idea of serial crystallography. They proposed to store single biological molecules within vitreous ice jackets. The molecules can then be aligned by a polarized laser, and electron diffraction patterns can be accumulated from a stream of identically aligned molecules. A key feature of this method[6] is sample alignment or orientation. In conventional crystallography, a single crystal is placed onto a substrate and oriented by a rotating sample stage (goniometer). However, if the sample is a single molecule, diffraction from the substrate is likely to be stronger than that from the molecule. Therefore, substrate free sample orientation and reorientation are required for this type of single molecule serial crystallography.

The method of using uniform electric and magnetic fields to control the orientation of molecule has been developed in the last two decades.[12-14] For

clarification, in this thesis, orientation means a distinction between the head and tail of a molecule, while alignment makes no such distinction. In DC field induced orientation, the interaction between the permanent dipole of a polar molecule and a strong static field has to be larger than the rotational energy of the molecule. Our research group and the Miller group have pioneered this technique in the gas phase and later in superfluid helium droplets.[15-17] We have also developed the technique of linear dichroism spectroscopy of oriented gas phase molecules for investigations of electronic and vibrational transitions in DC electric fields.[15, 18-19] Similarly, in laser induced alignment, the polarizability anisotropy of the molecule interacts with the electric field of a laser and generates an induced dipole. Different from DC fields, a laser field oscillates at the optical frequency of the laser and hence only the outer layer electrons of a molecule are capable of following the fast oscillating electric field. It is therefore the interaction of the induced dipole with the laser field that contributes to the alignment of the molecular frame.[13, 20-22] Kumarappan *et al*[13] reported alignment of both linear and asymmetric top molecules with long (nanosecond) and short pulses (femtosecond). In the experiment operated by Larsen *et al*[21], 3,4-dibromothiophene has been aligned with an intense nanosecond elliptically polarized laser pulse. More recently, Yang *et al*[14] have demonstrated electron diffraction of laser-aligned molecules in the gas phase.

The key in field induced alignment/orientation is the rotational temperature, and one of the most effective methods of cryogenic cooling is superfluid helium droplets. The internal equilibrium temperature of 0.38 K and the superfluidity of the helium environment are both beneficial for field induced alignment. Helium droplets

are also transparent from the far infrared to the vacuum ultraviolet, ensuring penetration of the laser field for alignment of doped species.[23] The low temperature of helium droplets, even lower than that of liquid helium used in cryo-EM, can also act as a heat sink for the embedded protein, protecting it from radiation damage. Cooling of the internal degrees of freedom of a protein ion can quench the molecular conformation to some degree, although given the high rate of evaporative cooling upon doping, large conformational change during cooling should be minimal. Hence conformational changes in superfluid helium droplets can be safely ignored, and as long as the protein ions can be frozen in their near native conformation upon doping, there should be no further denaturation in superfluid helium droplets.

Based on the above consideration, different from the initial idea of Spence and Doak,[6] we plan to avoid the use of vitreous ice. Instead, we plan to dope the protein ions from an electrospray ionization (ESI) source into superfluid helium droplets, to preserve the conformation of the protein ion and to assist with field induced orientation and alignment. The following is an outline of our approach. Our ultimate goal is to build a functional instrument for coherent electron diffraction from an oriented single macromolecule for structure determination at the atomic resolution.

1.2 Approach

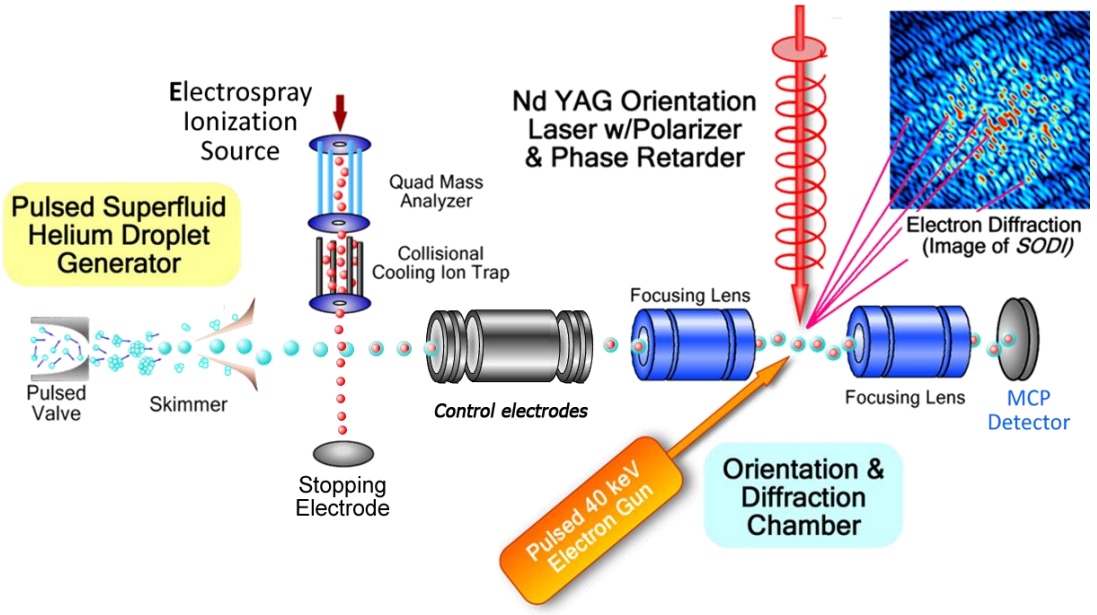

Fig. 1.1. Schematic of the project. Protein ions are generated by an ESI source and doped in superfluid helium droplets. In the orientation/diffraction chamber, all doped droplets are oriented in three dimensions with an elliptically polarized laser and exposed to a high energy electron beam to produce the continuous diffraction patterns. The image is accumulated for the necessary number of repeats until a satisfactory signal-to-noise ratio is obtained. The diffraction pattern on the top right is a simulated result of superoxide dismutase 1(SOD1).

The schematic of our project is shown in Fig. 1.1. macromolecular ions, generated from an standard electrospray ionization source, are introduced into the doping region after passing through a quadrupole mass spectrometer and a collisional ion trap. A pulsed superfluid helium droplet beam is released from a pulsed valve and collides with the packet of ions. The ions can be slowed down and or returned to the droplet beam for increased doping efficiency. The doped droplets are focused into the diffraction region where it overlaps with an elliptically polarized laser for field induced alignment. A high energy electron beam, 40 – 60 eV, is directed to the

overlapping region of the two beams, and the thus generated electron diffraction patterns are accumulated with a phosphorous screen and a CCD camera. This cycle of data acquisition repeats until a sufficiently high quality image from one orientation is obtained, and then the polarization of the laser will be changed for a different orientation. Oversampling of the resulting images generates sufficient data for the iterative algorithm to determine the molecular structure.

From a biophysics point of view, a major concern of this approach is the folding condition of the protein ions from the ESI source. In recent years, extensive efforts have been devoted to the control of the spray process,[24] and evidence of native or near native protein ions has been documented based on ion mobility measurements and hydrogen-deuterium exchange[25-26]. Wyttenbach *et al*[26] have reviewed the gas-phase conformations analyzed by measuring the collision cross section in a high pressure drift tube filled with helium and comparing it to model structure obtained by various theoretical methods such as molecular modeling. By combining ion mobility spectrometry with hydrogen-deuterium exchange-tandem mass spectrometry, Khakinejad *et al*[25] have also determined the structure of a model peptide ion that is KKDDDDIIKIIK. They have observed $[M+4H]^{4+}$ ions with two conformers and $[M+3H]^{3+}$ ions with a predominate conformer as well as an unresolved conformer. To limit unfolding from electrostatic repulsion of bare protein ions, methods of charge reduction have also been developed.[24, 27]

Once the macromolecular ions are sprayed into vacuum, further sample purification can be achieved via a quadrupole mass spectrometer as shown in the

figure, and/or an ion mobility[28-29] or electrostatic deflection [30] for conformation selection. This feature of in-situ purification has the advantage of eliminating the need of high concentration pure proteins, thus superior to other techniques including crystallography, NMR, and cryo-EM.

In 1998, Toennies *et al*[31] reported spectroscopy of doped particles inside superfluid helium droplets produced by supersonic expansion of precooled helium gas (1-20 K) at high pressures (30-60 bar). This work opened a new field of investigation under ultracold temperatures (0.38 K). After colliding with a superfluid helium droplet, a dopant molecule can be trapped inside, transferring its internal and translational energy to the droplet and reaching the same temperature of the droplet via evaporation of surface helium atoms.[23] Bierau *et al*[32] have since further demonstrated that mass selected cations from an ESI source of peptides and proteins can also be doped in superfluid helium droplets. Hence experimental investigations of ultracold cations have become a reality.

In laser induced orientation, the induced dipole, proportional to the polarizability anisotropy $\Delta\alpha'$, determines the degree of alignment. When the laser intensity is sufficiently strong, the angular deviation $<\Delta\theta^2>^{1/2}$ of a sample can be described as,

$$< \Delta\theta^2 >= \frac{k_B T c}{4\pi\Delta\alpha' I} \tag{1.1}$$

where k_B is the Boltzmann constant, T is the rotational temperature of the sample, and I is the intensity of the laser. For a given laser intensity, reducing the sample's

temperature is an effective way to improve the degree of alignment. For example, a small protein such as myoglobin (Mb) or green fluorescent protein can have a polarizability volume on the order 50 nm^3, in a laser field of 10^8 W/cm^3, the corresponding angular deviation is ~37^o at room temperature and ~1^o at 0.38 K. This value is to be compared with that of a small molecule, which has a typical polarizability volume several orders of magnitude smaller than that of proteins, and thus to obtain the same angular deviation, the required laser intensity is several orders of magnitude larger. Although proteins rotate 100 times more slowly than small molecules, the required time for alignment is still only on the order of nanoseconds. Consequently, it is easier to align large proteins than small gas phase molecules.

In the diffraction chamber, a coherent high energy electron beam is synchronized with the laser beam and the helium droplet beam. The resulting electron diffraction pattern is recorded on a phosphorus screen and an EMCCD camera. In conventional gas phase electron diffraction (GED), the intrinsic cylindrical symmetry of the experimental apparatus and the random orientation of the molecules result in diffraction patterns consisting of concentric interference rings. For small molecules, bond lengths can be determined with a precision better than 0.01 Å, thanks to the short wavelength (0.05Å at 60 keV) of the high energy electron beam and the large area of image detectors. For oriented samples, speckles of Fraunhofer diffraction are expected.

In addition to the short wavelength, electrons are more advantageous than x-ray photons for single molecule diffraction because of their larger diffraction cross

sections; by five orders of magnitude! Photons of x-ray sources can only interact with the nuclei, while electrons are affected by both electrons and nuclei of the scattering object. Based on one calculation[11], single molecule diffraction of X-ray photons is unrealistic not because of the flux limit of the radiation source, but because of the extreme intensity of the associated radiation field: distortion of the molecular frame occurs in the attosecond regime, exceeding the duration of femtosecond XFEL pulses. Electron diffraction is therefore the one and only remaining option for single molecule diffraction. However, the high scattering efficiency also limits the penetration depth of the electron beam, and in an electron transmission microscope (TEM), only samples less than 100 nm in thickness can be studied. In addition, radiation damage of electrons is also more severe for TEM than for XRD. Fortunately in our approach, neither of these limits are of any concern, since the dimension of single molecules is only on the order of a few nanometers, and each molecule is only exposed to the electron beam for a few microseconds.

From the resulting continuous electron diffraction pattern, using the oversampling and iterative phase retrieval method, high resolution electron density map can be obtained. Further structure refinement will be the same as that established for conventional crystallography.

1.3 Mission of this thesis

The scope of the overall project is divided into two separate branches, one on the protein source, and the other on diffraction. This thesis is dedicated to the

preparation of protein ions in superfluid helium droplets. Specifically, my mission is to explore the conditions of doping protein ions from an ESI source, characterizing the resulting doped droplets in terms of flux and size, and if necessary, re-conditioning the doped ions for diffraction.

In the framework of this thesis, two major experiments have been performed, although many side projects and iterations, including many failed attempts, have been explored within and outside the work presented here. In the first experiment, we used a continuous cesium ion source from thermionic emission for doping, so to avoid the difficulty in timing a pulsed ESI ion source with a limited ion flux. In the second experiment, we improved by introducing the ESI source but relied on the stable and abundant samples of reserpine and substance P for doping. To our pleasant surprise, the simplest approach of slowing down the ions using just an electrostatic electrode was successful to produce thousands of doped ions. Unfortunately, size measurements from these experiments revealed a high helium content of doped droplets, and hence size reduction became necessary prior to electron diffraction.

At the conclusion of the experimental work of this thesis, the basic idea of protein doping and size control is established. Continuation of this branch of effort will involve doping of a variety of protein ions and perhaps testing of the laser induced alignment effect using spectroscopic techniques. Ultimately, the protein source will be combined with the diffraction chamber for electron diffraction of aligned biomolecules.

1.4 Reference

1. Overington, J. P.; Al-Lazikani, B.; Hopkins, A. L., How many drug targets are there? *Nat Rev Drug Discov* **2006,** *5*, 993-996.
2. Chaudhuri, T.K. and Paul, S., Protein-misfolding disease and chaperone-based therapeutic approaches. FEBS Journal **2006**, 273, 1331-1349.
3. Berman, H. M.; Coimbatore Narayanan, B.; Costanzo, L. D.; Dutta, S.; Ghosh, S.; Hudson, B. P.; Lawson, C. L.; Peisach, E.; Prlić, A.; Rose, P. W.; Shao, C.; Yang, H.; Young, J.; Zardecki, C., Trendspotting in the Protein Data Bank. *FEBS Letters* **2013,** *587*, 1036-1045.
4. Renault, L.; Chou, H.-T.; Chiu, P.-L.; Hill, R. M.; Zeng, X.; Gipson, B.; Zhang, Z. Y.; Cheng, A.; Unger, V.; Stahlberg, H., Milestones in electron crystallography. *J. Comput.-Aided Mol. Des.* **2006,** *20*, 519-527.
5. Atkins, P. P., Julio, *Physical Chemistry, Ninth Edition*. Oxford University Press: Great Britain, 2010.
6. Spence, J. C. H.; Doak, R. B., Single molecule diffraction. *Phys. Rev. Lett.* **2004,** *92*, 198102.
7. Neutze, R.; Wouts, R.; van, d. S. D.; Weckert, E.; Hajdu, J., Potential for biomolecular imaging with femtosecond x-ray pulses. *Nature* **2000,** *406*, 752-757.
8. Miao, J.; Ishikawa, T.; Shen, Q.; Earnest, T., Extending X-ray crystallography to allow the imaging of noncrystalline materials, cells, and single protein complexes. *Annu. Rev. Phys. Chem.* **2008,** *59*, 387-410.
9. Bogan, M. J.; Benner, W. H.; Boutet, S.; Rohner, U.; Frank, M.; Barty, A.; Seibert, M. M.; Maia, F.; Marchesini, S.; Bajt, S.; Woods, B.; Riot, V.; Hau-Riege, S. P.; Svenda, M.; Marklund, E.; Spiller, E.; Hajdu, J.; Chapman, H. N., Single particle x-ray diffractive imaging. *Nano Lett.* **2008,** *8*, 310-316.
10. Miao, J.; Charalambous, P.; Kirz, J.; Sayre, D., Extending the methodology of x-ray crystallography to allow imaging of micrometre-sized non-crystalline specimens. *Nature* **1999,** *400*, 342-344.
11. Fratalocchi, A.; Ruocco, G., Single-molecule imaging with x-ray free-electron lasers: dream or reality? *Phys. Rev. Lett.* **2011,** *106*, 105504.
12. Filsinger, F.; Meijer, G.; Stapelfeldt, H.; Chapman, H. N.; Kuepper, J., State- and conformer-selected beams of aligned and oriented molecules for ultrafast diffraction studies. *Phys. Chem. Chem. Phys.* **2011,** *13*, 2076-2087.
13. Kumarappan, V.; Viftrup, S. S.; Holmegaard, L.; Bisgaard, C. Z.; Stapelfeldt, H., Aligning molecules with long or short laser pulses. *Phys. Scr.* **2007,** *76*, C63-C68.
14. Yang, J.; Makhija, V.; Kumarappan, V.; Centurion, M., Reconstruction of three-dimensional molecular structure from diffraction of laser-aligned molecules. *Struct. Dyn.* **2014,** *1*, 044101/1-044101/10.
15. Kong, W.; Pei, L.; Zhang, J., Linear dichroism spectroscopy of gas phase biological molecules embedded in superfluid helium droplets. *Int. Rev. Phys. Chem.* **2009,** *28*, 33-52.
16. Choi, M. Y.; Miller, R. E., Four tautomers of isolated guanine from infrared laser spectroscopy in helium nanodroplets. *J. Am. Chem. Soc.* **2006,** *128*, 7320-7328.
17. Choi, M. Y.; Miller, R. E., Infrared laser spectroscopy of imidazole complexes in helium nanodroplets: Monomer, dimer, and binary water complexes. *J. Phys. Chem. A* **2006,** *110*, 9344-9351.

18. Choi, M. Y.; Dong, F.; Miller, R. E., Multiple tautomers of cytosine identified and characterized by infrared laser spectroscopy in helium nanodroplets: probing structure using vibrational transition moment angles. *Philos. Transact. A Math. Phys. Eng. Sci.* **2005,** *363*, 393-412; discussion 412-3.
19. Dong, F.; Miller, R. E., Vibrational transition moment angles in isolated biomolecules: A structural tool. *Science* **2002,** *298*, 1227-1230.
20. Sakai, H.; Safvan, C. P.; Larsen, J. J.; Hilligsoe, K. M.; Hald, K.; Stapelfeldt, H., Controlling the alignment of neutral molecules by a strong laser field. *J. Chem. Phys.* **1999,** *110*, 10235-10238.
21. Larsen, J. J.; Hald, K.; Bjerre, N.; Stapelfeldt, H.; Seideman, T., Three dimensional alignment of molecules using elliptically polarized laser fields. *Phys. Rev. Lett.* **2000,** *85*, 2470-2473.
22. Sakai, H.; Larsen, J. J.; Safvan, C. P.; Wendt-Larsen, I.; Stapelfeldt, H.; Kanai, T., Alignment of neutral molecules by a strong nonresonant linearly polarized laser field. *ACS Symp. Ser.* **2002,** *821*, 320-335.
23. Toennies, J. P.; Vilesov, A. F., Matrix techniques: Superfluid helium droplets: A uniquely cold nanomatrix for molecules and molecular complexes. *Angew. Chem., Int. Ed.* **2004,** *43*, 2622-2648.
24. Kaddis, C. S.; Loo, J. A., Native protein MS and ion mobility: Large flying proteins with ESI. *Anal. Chem.* **2007,** *79*, 1778-1784.
25. Khakinejad, M. K., S; Maleki, H; Arndt, J; Donohoe, G; Valentine, S., Combining Ion Mobility Spectrometry with Hydrogen-Deuterium Exchange and Top-Down MS for Peptide Ion Structure Analysis. *J.Am.Soc.Mass Spectrom* **2014,** *25*, 2103-2115.
26. Wyttenbach, T.; Bowers, M. T., Gas-phase conformations: The ion mobility/ion chromatography method. *Top. Curr. Chem.* **2003,** *225*, 207-232.
27. Benesch, J. L. P.; Robinson, C. V., Mass spectrometry of macromolecular assemblies: Preservation and dissociation. *Curr. Opin. Struct. Biol.* **2006,** *16*, 245-251.
28. Burmistrova A, G. V., Duwez AS, De Pauw E., Ion mobility spectrometry reveals duplex DNA dissociation intermediates. *J Am Soc Mass Spectrom.* **2013,** *24*, 1777-1786.
29. Wang, S. C.; Politis, A.; Di, B. N.; Bavro, V. N.; Tucker, S. J.; Booth, P. J.; Barrera, N. P.; Robinson, C. V., Ion Mobility Mass Spectrometry of Two Tetrameric Membrane Protein Complexes Reveals Compact Structures and Differences in Stability and Packing. *J. Am. Chem. Soc.* **2010,** *132*, 15468-15470.
30. Horke, D. T., S; Chang, YP; Stern, S; Mullins, T; Kierspel, T; Küpper, J., Spatial separation of molecular conformers and clusters. *J Vis Exp.* **2014,** *83*, e51137.
31. Toennies, J. P.; Vilesov, A. F., Spectroscopy of atoms and molecules in liquid helium. *Annu. Rev. Phys. Chem.* **1998,** *49*, 1-41.
32. Bierau, F.; Kupser, P.; Meijer, G.; von Helden, G., Catching proteins in liquid helium droplets. *Phys. Rev. Lett.* **2010,** *105*, 133402.

Chapter 2 Superfluid Helium droplets

2.1 Properties of helium

Helium is unique among all chemical substances in that it exists in the liquid state even when its temperature is reduced to near absolute zero Kelvin, as long as the pressure is below 25 bar. In nature, bosonic ^{4}He and fermionic ^{3}He are two stable isotopes of helium, both of which and their mixture can exist in the form of bulk liquids and in finite systems as droplets. The interaction between helium atoms is van der Waals in nature and it is relatively weak: in bulk liquid, the binding energy of ^{4}He is 7.17 K and of ^{3}He is 2.5 K. The binding energies are even smaller in finite sized droplets.[1] The natural abundance of the isotope ^{4}He is 99.999863%, and hence in most helium related experiments, only ^{4}He is considered.

The weak interaction between helium atoms and the high zero point energy of the light element result in a superfluid liquid phase, He-II, at temperatures below 2.17 K, as shown in the phase diagram of Fig. 2.1. The λ line separates the two liquid phases into a normal liquid and a superfluid liquid. In the superfluid phase, heat is transferred by a second sound wave rather than through diffusion, thus superfluid helium has the highest heat conductivity, so high that no temperature gradient is possible while transporting a large amount of heat. Because of the existence of these two liquid phases, Landau introduced a two-fluid model to describe a liquid helium system. The ratio of the respective components depends on the temperature: the fraction of the superfluid fluid phase increases with decreasing temperature.[2]

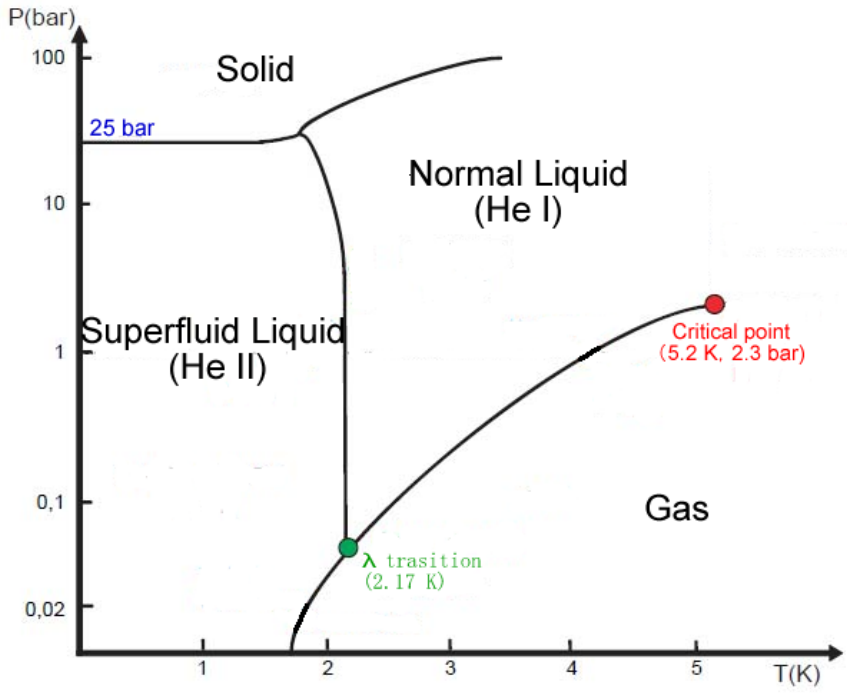

Fig. 2.1. Phase diagram of ^{4}He.

2.2 Superfluidity

A superfluid has zero viscosity. Based on Landau's theory of superfluidity, if a particle moves at a velocity below the critical velocity $v_L = \left(\frac{E}{p}\right)_{min}$, it would fail to excite the fluid via collisions, hence the particle would experience no viscosity from the fluid.[3] The origin of superfluidity can be traced to the dispersion relation obtained from inelastic neutron scattering.[4] Fig. 2.2 shows the relation of collective energy E and momentum p for bulk helium. At low energies, only sound waves -- phonons -- are accessible with a linear dispersion relation $E = pv_s$ where v_s is the velocity of sound. However, at higher energies and momenta, above minimum thresholds Δ and

p_0, "rotons" can contribute to the heat capacity and participate in excitation. The dispersion relation can then be written in the form of

$$E = \Delta + \frac{(p-p_0)^2}{2\mu}, \tag{2.1}$$

where μ is an effective mass that defines the curvature in the region of the threshold minimum. In the measurement by Henshaw and Woods,[4] the excitation energy is about $\frac{\Delta}{k_B} = 8.65\ K$ (k_B is the Boltzmann constant) and the momentum $\frac{p_0}{\hbar} = 19.1\ nm^{-1}$. The Landau critical velocity is given approximately by $v_L = \frac{\Delta}{p_o} \approx 60\ m/s$.[4] That means motion without viscosity will exist only when the relative velocity between the particle and the fluid is below the Landau critical velocity of 60 m/s.

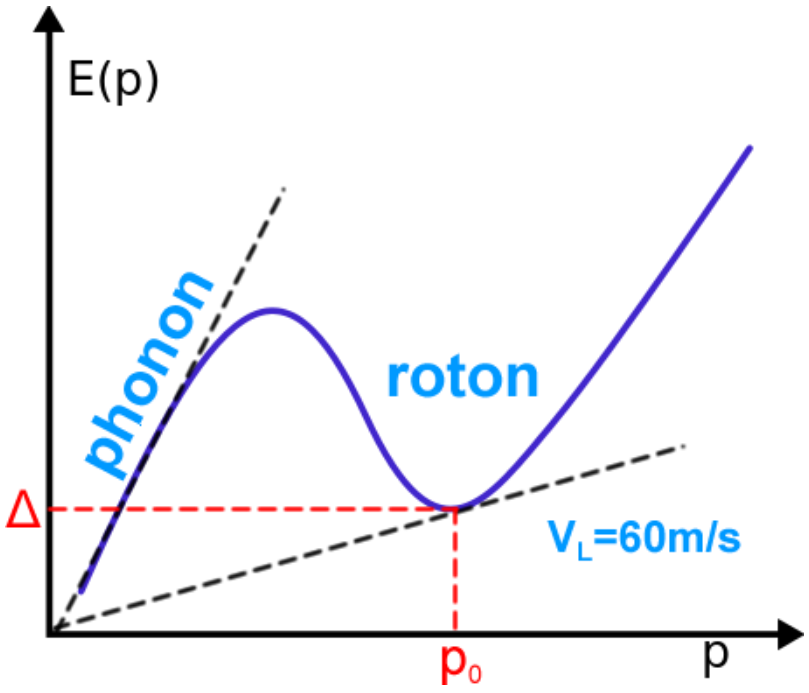

Fig. 2.2. The dispersion relation of helium.[5]

2.3 Structure of helium droplets

A helium cluster is called a droplet when it contains more than 1000 helium atoms. According to the liquid drop model (LDM), the core of a helium droplet forms a sphere with a sharp outer boundary when it is in the ground state. The particle density in the center of a helium droplet is uniform and is close to the bulk liquid value of $\rho = 0.022$ atoms/Å^3. The radius R_d of a droplet core can be calculated by the equation of $R_d = \sqrt[3]{\frac{3N}{4\pi\rho}} = 2.22N^{\frac{1}{3}}$Å, where N is the number of helium atoms of a droplet. For a droplet with N = 1000 atoms, its radius is about 22 Å, so helium droplets are also called nanodroplets. In addition, the density of a helium droplet reduces from 90% to 10% of its bulk value in the surface region, which has a thickness of approximately 10 Å.[6-7] This surface region is typically ignored in most discussions of droplet related properties.

2.4 Collective elementary excitations in a helium droplet

In a helium droplet with a finite size, elementary excitation can be classified as compression modes with higher energies and surface vibrational modes with lower energies, and both are dependent on the size of the droplet.[8] These collective modes are observed when the size of a helium droplet is bigger than 80 atoms. Excitation of these modes is further limited by the evaporation energy, i. e., the binding energy. In Fig. 2.3, the lowest fundamental frequencies of these two types of vibrational modes for different sized droplets are compared with the binding energy of a helium atom

from the surface of a helium cluster (the curve labeled “Evaporation”). At an internal temperature of 0.37 K and within the size range of $N = 10^3$-10^6, only the surface vibrational mode, the “ripplons”, are accessible for excitation. This surface excitation mode plays an important role in the evaporative cooling process of pure droplets and doped droplets.[6, 8] Fig. 2.3 also indicates that with increasing droplet sizes ($N > 10^6$), the compression mode can also be excited at the same low temperature.

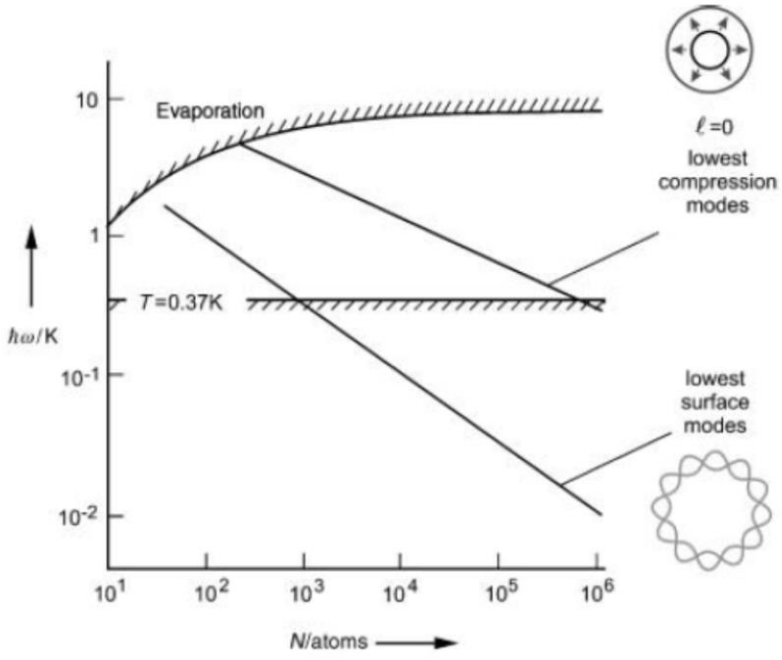

Fig. 2.3. Energies of elementary excitations of a helium droplet as a function of the number of helium atoms in a droplet.[6]

2.5 Terminal temperature of a superfluid helium droplet beam

The terminal temperature of helium droplets is determined by the evaporative cooling kinetics on the droplet surface. In 1990, Brink and Stringari[9] developed a statistical description of helium clusters, and they determined that the internal temperature of a droplet is about 0.4 K. The result is proven by several experiments.[10-13] For example, Hartmann *et al*[10] obtained a rotationally resolved infrared spectrum of SF_6 doped in superfluid helium droplets, and the resulting internal temperature was derived to be around 0.37 K ± 0.05 K.

Brink and Stringari[9] calculated the rate of evaporation of helium droplets at low temperatures by using the Weisskopf formula, which describes the probability per unit time for a cluster He_N with energy E_N to emit an atom with a kinetic energy ε, yielding a cluster of size N-1 with $E_{N-1} = E_N - E_0 - \varepsilon$. Here E_0 (> 0) is the binding energy of the emitted particle. Evaporation terminates when $E_{N-1} \approx E_0$. Based on the density of states of surface ripplons, the energy of a droplet containing N helium atoms can be written as: $E_N = \alpha\beta^{-\frac{7}{3}}N^{\frac{2}{3}}$, where $\alpha = 0.39K^{-\frac{4}{3}}$, and $\beta = \frac{1}{k_B T}$. The binding energy E_0 can be expressed as: $E_0 = -a_v - \frac{2}{3}a_s N^{-\frac{1}{3}}$ with $a_v = -7.15K$ and $a_s = 6.95K$. For a cluster with size of 1000 atoms, the internal temperature will reach to 0.45 K.[9]

2.6 Droplet formation

2.6.1 Formation

Helium droplets are produced by free-jet expansion into vacuum under high pressure and low temperature conditions, and the resulting cluster beam has a high mass flow rate and a high uniform velocity.[14] The gas plume emerging from the high pressure source is divergent during expansion, thus the center of the gas plume is more or less adiabatic, experiencing no energy exchange with the environment. For this reason, the interaction between helium atoms plays a more important role than the collision between helium atoms and the environment. Although theoretically free jet expansion into vacuum is irreversible, in any realistic expansion, a pressure gradient is inevitably formed near the nozzle, and hence the effusing gas from the nozzle experiences a gradual pressure reduction. We can therefore assume that the expansion is reversible, and that the evolution of the gas plume follows an expansion isentrope.[15] The gas plume from the nozzle, first forms a viscous flow at thermodynamic equilibrium, and after condensation and pressure reduction, the plume reaches a quitting surface and forms a free molecular flow. Condensation into helium droplets occurs primarily in the viscous flow region. As the gas plume moves further into the vacuum, a decrease in particle density results in a decrease in the frequency of collision, and eventually all collisions cease.[16] In this region, the beam contains a mix of helium atoms and droplets, and the droplets will be cooled down by evaporation of helium atoms from the surface.[6]

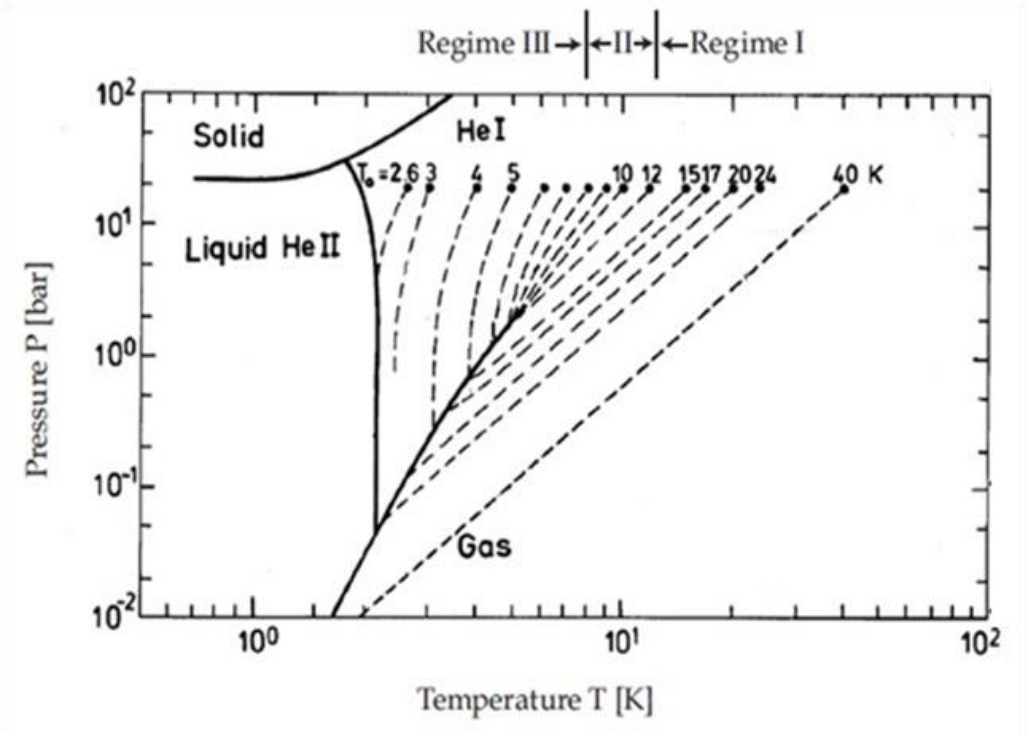

Fig. 2.4.. Expansion isentropes plotted on the phase diagram of ^{4}He. There are three different regions for droplet formation depending on the nozzle temperature.[17]

The mechanism of droplet formation in a free jet is critically affected by the nozzle temperature T_0. Depending on T_0 and hence the resulting isentrope, three different regimes of droplet formation are typically discussed, as shown in Fig. 2.4. When the nozzle temperature is higher than 12 K (regime I), the expansion isentrope stays in the gas phase, and condensation is the only path for droplet formation. In this regime, small clusters form after passing the sonic point of the nozzle.[17] At temperatures below 8 K (regime III), helium in the source is already in the liquid phase, and helium clusters are formed by fragmentation of liquid helium. At even lower temperatures below 4.2 K, Rayleigh oscillations can break up the liquid into large ($N \approx 10^{10}$) uniform sized droplets.[18] Regime II is called supercritical expansion

with source temperatures ranging from 8 K to 12 K. During the expansion, there is no clear separation of liquid and gas, and the expansion is characterized by large density fluctuations.[17] The expansion isentrope passes through or close to the critical point.[19]

2.6.2 Theoretical modeling of regime I

Limited by the available cooling capacity of our cryostat, all of our experiments in this thesis were performed in regime I. In this regime, the mechanism of condensation and cluster formation can be described from both a macroscopic and a microscopic point of view.[16] The phase diagram of Fig. 2.5 illustrates the macroscopic process. Gas expansion starts at a certain point A (P_0,T_0), and with decreasing pressure and temperature, the system follows the isentropic line to point B, which is located on the vapor pressure curve $P_v(T)$. After passing through point B, the gas beam either condenses into normal liquid or remains as supersaturated gas. Supersaturation reaches its limit at point C and all gaseous molecules condense into droplets. The energy released from condensation heats the newly formed clusters and returns the system back to the vapor pressure curve.[16] With continuous decrease in P and T, the mixture of normal cluster and gas moves down to the He II region following the vapor pressure curve. Finally, superfluid droplets appear at the point of λ transition.

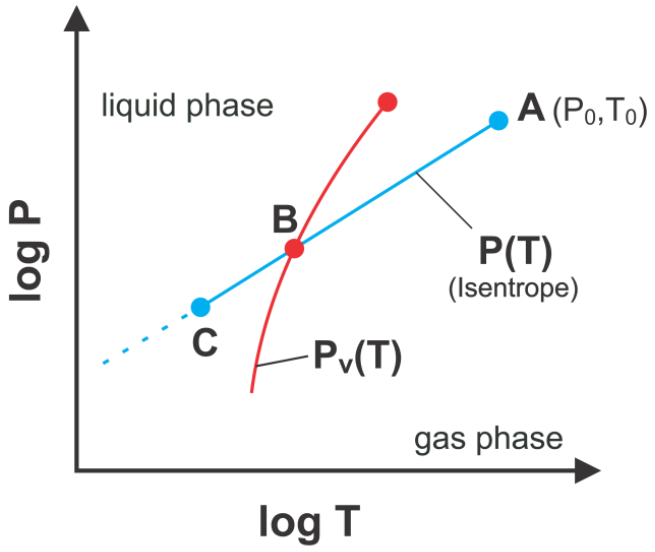

Fig. 2.5. Scheme of the expansion curve P(T) and the vapor pressure curve $P_v(T)$ in a double logarithmic diagram.[16]

The microscopic treatment centers on the nucleation process of gaseous helium. At the very beginning of expansion, or maybe even in the reservoir, dimers are formed by three-body collisions. During the expansion, the preformed dimers serve as condensation nuclei, and as long as the number density of monomers is higher than the number density of clusters, cluster-monomer collision dominates. Hence, clusters just grow successively via accumulation of monomers. With increasing cluster concentration, collisions between clusters start to play an increasingly important role.[16] Eventually, particle collisions will diminish and clusters reach their final sizes. The formation of clusters is related to the rate of three-body collisions Z_3 following $P_0^2 l/T_0^2$,[16] where l is the length of the nozzle. Thus the formation and growth of clusters will be efficiently improved by a higher initial pressure and a lower initial temperature. The internal temperature of this normal helium cluster continues to go

down via evaporation of surface helium atoms until it passes the Lambda line and reaches the terminal temperature of 0.38 K.

2.7 Velocity of droplet beam

2.7.1 General equation

For a pure helium beam, the condensation process should comply with the law of energy conservation, which yields the equation[15]

$$E = U + PV + \frac{1}{2}mN_A v^2, \tag{2.2}$$

where U is the thermal molar energy (translational and internal motions), and P and V are pressure and volume of the gas. The pressure-volume work *PV* is included due to the change in molar volume *V* of the fluid, and the kinetic energy term results from the center-of-mass motion at a mean velocity *v* for N_A particles each with a mass *m*. Introducing enthalpy $H = U + PV$, the center-of-mass motion velocity of the beam is given by[15]

$$v_f = \sqrt{\frac{2(H_0 - H_f)}{N_A m} + v_0^2}\,, \tag{2.3}$$

where H_0 is the enthalpy of fluid. Since the center-of-mass motion in the valve v_0 is zero, the final beam velocity can be written as

$$v_f = \sqrt{\frac{2(H_0 - H_f)}{N_A m}}\,. \tag{2.4}$$

During condensation, the enthalpy of vaporization $\Delta_v H$ is released, therefore, the final beam velocity depends on both the initial conditions determined by P_0 and T_0, and the initial and final status of helium. This means that a cold liquid beam may be faster than a cold gaseous beam.[14-15]

The full-width-at-half-maximum (FWHM) spread of the atomic velocity Δv scales with the final beam temperature, and in general, a helium beam has a sharp velocity distribution with $\frac{\Delta v}{v} \approx 0.01 - 0.03$.[6, 16, 20]

2.7.2 Beam velocities under different expansion conditions

The terminal beam velocities are different for expansions from three different regimes in Fig.2.4. In regime I, assuming ideal gas properties for helium, the enthalpy is $H_0 = \frac{5}{2} k_B T_o$. Since the final temperature is much lower than the initial temperature T_0, the final average beam velocity, without condensation correction, can be written as

$$v_{ave} = \sqrt{\frac{5k_B T_0}{m_{He}}}. \tag{2.5}$$

This average beam velocity is thus only determined by the nozzle temperature and helium atomic mass, not the initial pressure.

The beam velocity in regime III can be derived from hydrodynamics. Assuming the fluid is incompressible and the loss from fluid friction is negligible at any point along the direction of axial flow, the total energy including the internal

energy, kinetic energy and potential energy is conserved. Then, the liquid beam velocity can be derived from the Bernoulli equation,[21]

$$v_l = C\sqrt{\frac{2P_0}{\rho_{M,0}}}, \tag{2.6}$$

where $\rho_{M,0}$ is the mass density and C is the discharge coefficient related to the friction exerted by the orifice. For a smooth orifice, C is equal to 1. In the temperature range from 1.5 K to 4.2 K, the velocity of a liquid beam has been measured by Grisenti *et al*[18]. The authors found that at P_0 = 0.5 bar and T_0 = 1.6 K, the measured lowest beam velocity is 15 m/s, in general agreement with the above equation. The authors have also reported that with decreasing temperature and increasing pressure, the velocity distribution becomes increasingly narrow, resulting in $\frac{\Delta v}{v} < 1\%$.[6, 18]

Unfortunately for regime II, no analytical expression for the beam velocity has been derived in the literature.

2.8 Size and size distribution of a droplet beam

Studies of size and size distribution of helium droplet beams are particularly relevant for doping of droplets. Under different source conditions, the formation mechanism of helium droplets changes from condensation of gas to fragmentation of liquid. As a result, helium droplets can have a wide range of sizes. Unfortunately direct size measurement of bare helium droplets is difficult since a helium droplet is neutral and any collisions with the droplet beam leads to evaporation and hence loss

in mass and size. Nevertheless, several methods of measuring bare droplet sizes and size distributions have been reported in the literature.[7, 22-24]

In regime I of Fig. 2.4, a statistical analysis results in a log-normal function:[22]

$$P_N(N) = (N\sigma\sqrt{2\pi})^{-1} \exp\left[\frac{-(lnN-\mu)^2}{2\sigma^2}\right]. \quad (2.7)$$

Here $P_N(N)$ is the probability of a droplet consisting N helium atoms, and σ and μ are the standard deviation and the mean of the distribution of lnN. The average size of a helium droplet beam $\bar{N}$ and the standard deviation S can be derived as:

$$\bar{N} = \exp(\mu + \frac{\sigma^2}{2}), \quad S = \bar{N}\sqrt{\exp(\sigma^2) - 1}. \quad (2.8)$$

Assuming a value of 0.63 for σ, the relation between the average size and standard deviation is[24]

$$S = 0.69\bar{N}. \quad (2.9)$$

The mean size of a droplet beam and the size distribution parameters σ and μ can be obtained from fittings of experimental results or from theoretical modeling. In the work of Lewerenz et al,[22] size distributions obtained from 3×10^3 to 10^4 have been successfully fitted to the log-normal model at source temperatures from 14 K to 24 K.

Based on thermodynamic and kinetic parameters of the expansion nozzle, a theoretical model has resulted in an average size of:[25]

$$\ln\bar{N} = 2.4ln\Gamma - 3.9, \quad (2.10)$$

where Γ is a dimensionless parameter:[26]

$$\Gamma = K_1^q K_2^{1-q}. \tag{2.11}$$

Here K_1 is the kinetic parameter, K_2 is the thermodynamic parameter, and the value q is variable between 0.6 and 0.8.[25-26] These parameters are defined as:

$$K_1 = n_0 v \left(\frac{d}{a_0}\right) \left(\frac{2\gamma}{\pi m}\right)^{\frac{1}{2}} \left(\frac{T_{ref}}{T_0}\right)^{\frac{3}{4}} \tag{2.12}$$

$$K_2 = \left(\frac{P_0}{A}\right)\left(\frac{T_{ref}}{T_0}\right)^{\frac{5}{2}}. \tag{2.13}$$

where n_0 is the number density, v is the volume per helium atom, d is the diameter of the source-orifice, a_0 is the speed of sound at the source, γ is the droplet surface tension, A is a vapor pressure constant, and T_{ref} is defined as:

$$T_{ref} = \frac{v^{-\frac{2}{3}}\gamma}{k_B}. \tag{2.14}$$

As a reference, for a nozzle of 500 μm in diameter at a stagnation pressure of 50 bar and a source temperature of 14 K, a cluster contains about 4.8×10^4 atoms at Γ = 450.[26] The corresponding parameters of σ and μ can be obtained from Eq. 2.8. In most cases, σ is a constant in the range of 0.55 to 0.75.[22, 24]

In regime III with T_0 < 8 K, the average size and size distribution of droplets formed by fragmentation of a liquid beam is found to be dependent on the surface tension, the nozzle diameter and a characteristic flow speed:

$$\bar{N} = \frac{80\pi}{3}\frac{\gamma}{m}\left(\frac{d}{a_0}\right)^2. \tag{2.15}$$

The size distribution can be theoretically derived as an exponential distribution:[27]

$$P_N(N) = \frac{1}{\bar{N}} \exp(-\frac{N}{\bar{N}}). \quad (2.16)$$

Single exponential distributions from regime III have been generally confirmed from experimental measurements.[27] However, when size-dependent detection efficiency is included in the analysis of the experimental data, including the different ionization cross sections of different sized droplets, slight deviations from single exponential functions are observable.[27]

Typical average sizes increase from regime I (< 10^4) to II (10^5 - 10^6) to III (> 10^6). However, the size distribution with a detailed quantitative description for regime II is still unavailable.

2.9 Beam flux

In a continuous beam, the theoretical total beam flux *I* can be calculated from the flow rate through a nozzle with a diameter *d*:[16,21]

$$\mathrm{I} = \pi(\frac{d}{2})^2 v_x \rho_n, \quad (2.17)$$

Where v_x is the axial velocity of the beam, and ρ_n is the number density of helium. At a stagnation pressure of P_0 = 50 bar and a source temperature T_0 = 14 K, a nozzle with 500 μm dia. can have a total beam flux of 4.8×10^{23} atoms/s. For a pulsed beam, the flux needs to be modified by the duty cycle D_c, which is determined by

$$D_c = \frac{\delta t}{\Delta t} = \delta t \cdot \upsilon, \quad (2.18)$$

where δt is the duration of an ideal rectangular shaped pulse, Δt is the time interval between two successive pulses, and v is the repetition rate.[16] In our case, the pulse valve is operated at a repetition rate of ν =10 Hz with a duration δt =145 μs, and the resulting flux is 7×10^{20} atoms/s.

In practice, the real beam flux of a pulsed valve can be derived from the pressure change ΔP and the available pumping speed of the vacuum system Z_p (in units of m^3 per second). In a chamber of volume V at an ambient temperature T, the resulting beam flux I' can be written as,

$$I' = \frac{\Delta P}{k_B T} \cdot Z_P. \tag{2.19}$$

Typical ionization gauges have response times on the order of seconds, and at a repetition rate of 10 Hz, only an average value for the pressure of the system can be read. Hence in Eq. 2.19, ΔP is the average pressure change between the pulsed valve on and off.

In our experiment, the pressure in the source chamber is changed from 4×10^{-7} Torr to 4×10^{-6} Torr when the pulsed valve is turned on. The absolute change in pressure ΔP is 3.6×10^{-6} Torr. The source chamber with an ambient temperature of T = 300 K is evacuated by two pumps with a total pumping speed of Z_p = 4.2 m^3/s. The resulting flux is about 5×10^{17} atoms/s, which is only 0.05% of the theoretical value. Several factors contribute to this discrepancy. First, the gas pulse is not an ideal square function with clear on and off, and the actual opening time is likely to be shorter than the duration of the electrical pulse of 145 μs. Secondly, due to the conical

tip of the poppet, the real cross section for gas flow is slightly smaller than the diameter of the channel of 500 μm. Both reasons can result in a much lower flux than that from the theoretical calculation of Eq. 2.17. During the experiment, the pressure of the source chamber is read from an ionization gauge mounted far away from the pulsed valve. When the pulsed valve is on, a pressure gradient between the region of the pulsed valve and the ionization gauge develops. Therefore, the pressure change from the ion gauge is probably below the actual value. This means that the calculation of Eq. 2.19 is probably lower than the actual flux. Considering all these factors, a difference of a factor of 20 based on calculations from Eq. 2.17 and 2.19 is still reasonable.

2.10 Doping of helium droplets

Doping of superfluid helium droplets offers the advantage of investigating isolated particles under cryogenic temperatures in a non-perturbing medium. Both neutral particles and ions have been successfully doped in many laboratories.[28-31] The top panel of Fig. 2.6a shows the experimental setup for doping neutral gas-phase particles.[32] A beam of helium droplets produced by supersonic expansion and collimated by a skimmer enters into a pickup cell to collide with gaseous neutral particles. Since the gaseous molecules are neutral, doping of multiple particles may happen and the probability follows Poisson statistics.[22] After collision, the particles are quickly cooled down to the droplet's interior temperature of 0.38 K by transferring their internal energy to the droplets. The doped droplets, largely maintaining their velocity from supersonic expansion and condensation, can be

investigated by several experimental methods, including mass-spectroscopy and laser spectroscopy.

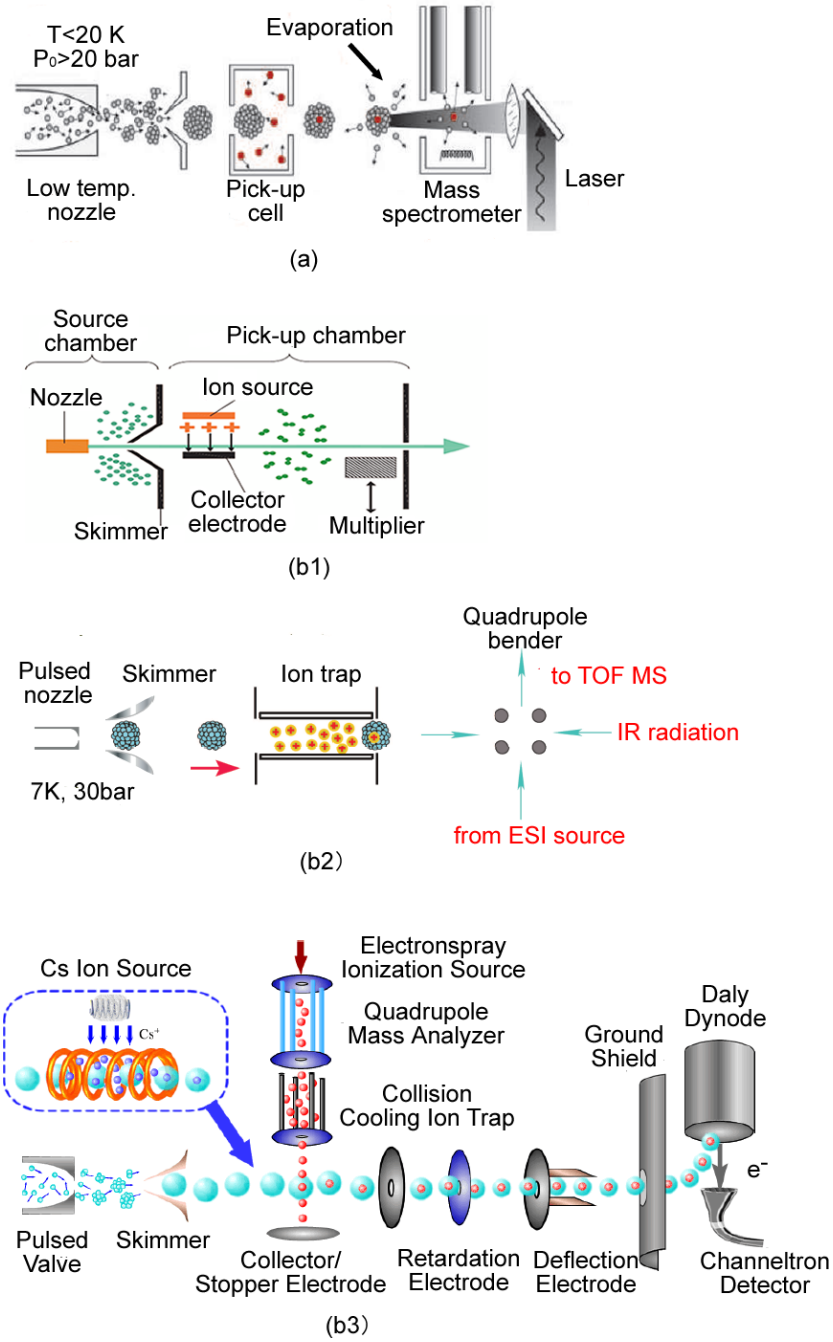

Fig. 2.6 (a) Standard setup for picking up neutral molecules from a gas cell by a passing beam of helium droplets.[32] (b1) Illustration of the experimental setup for doping sodium ions into helium droplets.[33] (b2) An ion trap is used to store ions for pickup.[34] (b3) Experimental apparatus of doping ESI ions directly into superfluid helium droplets without an ion trap.

Generally, two experimental approaches have been reported to obtain ion-doped helium droplets. One way is to ionize doped neutral species inside a droplet,[35-36] and the other method is to dope ions directly into helium droplets.[33-34] The bottom three panels of Fig.2.6 show the three experimental setups for ion doping. In Fig. 2.6b1, sodium ions are generated from a heated tungsten filament coated with a zeolite paste,[33] and opposite to the filament, a cylindrical collector electrode is biased at a negative voltage to confine the ions in the doping region. We have also adopted the thermionic emission method to generate cesium ions for doping. Instead of the straight filament and the cylindrical collector, we shaped the filament into a coil and bent it into a semicircle surrounding the droplet beam. The collector was made into a grid and was concentric with the filament (see chapter 5.4). Under a negative voltage on the collector, cesium ions would oscillate in the region of the droplet beam for effective doping. Fig. 2.6b2 shows the concept of Bierau *et al*[34] in using an ion trap to store ions for pickup. In their experiment, ions are produced from electrospray ionization and are trapped in a hexapole ion trap. The trap consists of six rods that are placed in a 14.1 mm diameter circle and are applied with a radio frequency field of 200 $V_{p\text{-}p}$ and 1.7 MHz. At each end, a stopping electrode biased at 1-3 V above the DC voltage on the rods is used for longitudinal trapping. After picking up an ion, doped droplets can escape from the ion trap only when their kinetic energy exceeds the longitudinal trapping potential energy. In practice, when the stopping voltage is set at 30 V and the velocity of droplet beam is 300 m/s, the minimum size of a droplet passing through the ion trap is about 1.6×10^4 helium atoms. Fig. 2.6b3 shows our experimental apparatus of doping ESI ions directly into helium droplets without an

ion trap. In the doping region, ions were slowed down and even returned by the stopping electrode biased at a positive voltage. This simple design eliminated the need of trap filling and collision gas pumping, and it was also much easier to integrate this doping process with future experiments.

2.11 Structure of doped droplets

In theory, the chemical potential of doping μ, largely determined by the binding energy between the dopant and helium atoms, can be used to determine the position of a dopant, either on the surface or inside the droplet. At $\mu < 0$, the free energy is decreased when a particle is immersed completely inside helium, and the particle prefers to stay in the center of a helium droplet – a heliophilic particle.[6] The dopant attracts the surrounding helium atoms and forces them to be localized, which in turn forms a considerable radial solvation structure of compressed helium atoms.[37-38] This structure is called a "snowball". For positively charged ions, this snowball effect is particularly strong due the large solvation energy and the strong ion-induced dipole interaction. Hence positive ions almost invariably reside inside a droplet.

At $\mu > 0$, a particle only attaches to the surface of a droplet, hence it is called heliophobic. The local repulsion related to the Pauli exclusion principle further induces a spatial separation between the electrons on helium atoms. Ultimately, at the surface of the droplet, a deformation in the form of a dimple is formed, and this structure is called a "bubble".[6, 12] This situation exists for electrons, anions, alkali metal atoms and some alkaline atoms.

Ancilotto et al[39] further constructed a simple model of the interaction between the dopant and the surrounding helium via a Lennard-Jones pair potential. The potential is characterized by a well depth ε and an equilibrium distance R_{min}. They use a dimensionless parameter λ to express the tendency of an impurity to be solvated inside a helium droplet:

$$\lambda = \frac{\rho \varepsilon R_{min}}{\frac{1}{2\overline{6}}\sigma} \tag{2.20}$$

with ρ denoting the number density of helium, and σ the surface tension. When λ > 1.9, the dopant molecule will be solvated in the interior of a helium droplet to form a snowball, and all closed shell atoms and molecules belong to this category. In the snowball structure of SF_6, there are two layers of helium atoms containing 22 and 50 helium atoms each, with a number density of 4 and 1.3 times more than that of the bulk.[40] Path integral Monte Carlo simulation further reveals that the first shell exhibits considerable exchange with the surrounding helium.[41] When λ < 1.9, the dopant stays on the surface, and alkali-metal atoms[42] and their small clusters[43-44] belong to this category.

For charged particles, the effects are much more extreme: some positively ions can be so strongly localized that they move within the helium droplet as a solid entity. In the work of Buzzacchi *et al*[45], the first layer helium atoms surrounding Na^+ and K^+ are completely localized so the snowball can be considered a solid, while those surrounding Li^+ and Cs^+ exhibit multiparticle permutational exchange. Negative

ions and electrons form bubbles on the surface of helium droplets. An electron can produce a large bubble with a void about 34 Å in diameter.[46]

2.12 Reference

1. Barranco, M.; Guardiola, R.; Hernandez, S.; Mayol, R.; Navarro, J.; Pi, M., Helium Nanodroplets: An Overview. *J. Low Temp. Phys.* **2006,** *142*, 1-81.
2. https://en.wikipedia.org/wiki/Superfluid_helium-4.
3. A.M.Guenault, *Basic superfluids*. 2003.
4. Henshaw, D. G.; Woods, A. D. B., Modes of Atomic Motions in Liquid Helium by Inelastic Scattering of Neutrons. *Physical Review* **1961,** *121*, 1266-1274.
5. Takeji Kebukawa, S. Y., Sigenobu Sunakawa, On the excitation energy in liquid helium II. *Progress of Theoretical physics* **1970,** *44*, 565-573.
6. Toennies, J. P.; Vilesov, A. F., Matrix techniques: Superfluid helium droplets: A uniquely cold nanomatrix for molecules and molecular complexes. *Angew. Chem., Int. Ed.* **2004,** *43*, 2622-2648.
7. Harms, J.; Toennies, J. P.; Dalfovo, F., Density of superfluid helium droplets. *Phys. Rev. B: Condens. Matter Mater. Phys.* **1998,** *58*, 3341-3350.
8. Toennies, J. P.; Vilesov, A. F., Novel low-energy vibrational states of foreign particles in fluid 4He clusters. *Chem. Phys. Lett.* **1995,** *235*, 596-603.
9. Brink, D. M. S., S., Density of states and evaporation rate of helium clusters. *Zeitschrift fuer Physik D: Atoms, Molecules and Clusters* **1990,** *15*, 257-263.
10. Hartmann, M.; Miller, R. E.; Toennies, J. P.; Vilesov, A., Rotationally resolved spectroscopy of SF_6 in liquid helium clusters: a molecular probe of cluster temperature. *Phys. Rev. Lett.* **1995,** *75*, 1566-9.
11. Toennies, J. P.; Vilesov, A. F., Spectroscopy of atoms and molecules in liquid helium. *Annu. Rev. Phys. Chem.* **1998,** *49*, 1-41.
12. Northby, J. A., Experimental studies of helium droplets. *The Journal of Chemical Physics* **2001,** *115*, 10065-10077.
13. Callegari, C. L., Kevin K.; Schmied, Roman; Scoles, Giacinto, Helium nanodroplet isolation rovibrational spectroscopy: Methods and recent results. *Journal of Chemical Physics* **2001,** *115*, 10090-10110.
14. Hagena, O. F.; Obert, W., Cluster Formation in Expanding Supersonic Jets: Effect of Pressure, Temperature, Nozzle Size, and Test Gas. *The Journal of Chemical Physics* **1972,** *56*, 1793-1802.
15. Christen, W.; Rademann, K.; Even, U., Supersonic Beams at High Particle Densities: Model Description beyond the Ideal Gas Approximation. *The Journal of Physical Chemistry A* **2010,** *114*, 11189-11201.
16. H.Pauly, *Atom, Molecule and Cluter Beams 1*. Springer Verlag: Berlin, 2000; Vol. 1,2.
17. Buchenau, H.; Knuth, E. L.; Northby, J.; Toennies, J. P.; Winkler, C., Mass spectra and time-of-flight distributions of helium cluster beams. *J. Chem. Phys.* **1990,** *92*, 6875-89.
18. Grisenti, R. E.; Toennies, J. P., Cryogenic Microjet Source for Orthotropic Beams of Ultralarge Superfluid Helium Droplets. *Phys. Rev. Lett.* **2003,** *90*, 234501/1-234501/4.

19. Harms, J.; Toennies, J. P.; Knuth, E. L., Droplets formed in helium free-jet expansions from states near the critical point. *J. Chem. Phys.* **1997,** *106*, 3348-3357.
20. Bruch, L. W.; Schollkopf, W.; Toennies, J. P., The formation of dimers and trimers in free jet 4He cryogenic expansions. *J. Chem. Phys.* **2002,** *117*, 1544-1566.
21. Bierau, F. Trapping biomolecular ions in superfluid helium droplets. Fachbereich Physik der Freien Universitat Berlin, Berlin, 2011.
22. Lewerenz, M.; Schilling, B.; Toennies, J. P., A new scattering deflection method for determining and selecting the sizes of large liquid clusters of helium-4. *Chem. Phys. Lett.* **1993,** *206*, 381-7.
23. Lewerenz, M.; Schilling, B.; Toennies, J. P., Successive capture and coagulation of atoms and molecules to small clusters in large liquid helium clusters. *J. Chem. Phys.* **1995,** *102*, 8191-207.
24. Schollkopf, W.; Toennies, J. P.; Savas, T. A.; Smith, H. I., A cluster size nanofilter with variable openings between 2 and 50 nm. *J. Chem. Phys.* **1998,** *109*, 9252-9257.
25. Knuth, E. L. S., Bernard; Toennies, J. Peter In *On scaling parameters for predicting cluster sizes in free jets*, Rarefied Gas Dynamics, Oxford, Oxford, 1995; pp 270-276.
26. Knuth, E. L., Size correlations for condensation clusters produced in free-jet expansions. *The Journal of Chemical Physics* **1997,** *107*, 9125-9132.
27. Knuth, E. L.; Henne, U., Average size and size distribution of large droplets produced in a free-jet expansion of a liquid. *The Journal of Chemical Physics* **1999,** *110*, 2664-2668.
28. Close, J. D.; Federmann, F.; Hoffmann, K.; Quaas, N., Absorption spectroscopy of C60 molecules isolated in helium droplets. *Chemical Physics Letters* **1997,** *276*, 393-398.
29. Federmann, F.; Hoffmann, K.; Quaas, N.; Toennies, J. P., Spectroscopy of extremely cold silver clusters in helium droplets. *Eur. Phys. J. D* **1999,** *9*, 11-14.
30. Diederich, T.; Doppner, T.; Braune, J.; Tiggesbaumker, J.; Meiwes-Broer, K.-H., Electron Delocalization in Magnesium Clusters Grown in Supercold Helium Droplets. *Phys. Rev. Lett.* **2001,** *86*, 4807-4810.
31. Mueller, S.; Mudrich, M.; Stienkemeier, F., Alkali-helium snowball complexes formed on helium nanodroplets. *J. Chem. Phys.* **2009,** *131*, 044319.
32. Hartmann, M.; Miller, R. E.; Toennies, J. P.; Vilesov, A. F., High-resolution molecular spectroscopy of van der Waals clusters in liquid helium droplets. *Science* **1996,** *272*, 1631-1634.
33. Falconer, T. M.; Lewis, W. K.; Bemish, R. J.; Miller, R. E.; Glish, G. L., Formation of cold ion-neutral clusters using superfluid helium nanodroplets. *Rev. Sci. Instrum.* **2010,** *81*, 054101.
34. Bierau, F.; Kupser, P.; Meijer, G.; von Helden, G., Catching proteins in liquid helium droplets. *Phys. Rev. Lett.* **2010,** *105*, 133402.
35. Callicoatt, B. E.; Forde, K.; Ruchti, T.; Jung, L.; Janda, K. C.; Halberstadt, N., Capture and ionization of argon within liquid helium droplets. *J. Chem. Phys.* **1998,** *108*, 9371-9382.
36. Yang, S.; Brereton, S. M.; Wheeler, M. D.; Ellis, A. M., Soft or hard ionization of molecules in helium nanodroplets? An electron impact investigation of alcohols and ethers. *Phys. Chem. Chem. Phys.* **2005,** *7*, 4082-4088.
37. Pi, M. M., Ricardo; Barranco, Manuel, Structure of large 3He-4He Mixed Drops around a Dopant Molecule. *Physical Review Letters* **1999,** *82*, 3093-3096.
38. Kwon, Y.; Whaley, K. B., Superfluid solvation structure of OCS in helium clusters. *The Journal of Chemical Physics* **2001,** *115*, 10146-10153.

39. Ancilotto, F. L., Peter B.; Cole, Milton W., Physics of solvation. *Journal of Low Temperature Physics* **1995,** *101*, 1123-1146.
40. Garcias, F.; Serra, L.; Casas, M.; Barranco, M., Ground-state properties of doped 3He clusters. *The Journal of Chemical Physics* **1998,** *108*, 9102-9106.
41. Kwon, Y.; Huang, P.; Patel, M. V.; Blume, D.; Whaley, K. B., Quantum solvation and molecular rotations in superfluid helium clusters. *The Journal of Chemical Physics* **2000,** *113*, 6469-6501.
42. Stienkemeier, F.; Higgins, J.; Ernst, W. E.; Scoles, G., Laser spectroscopy of alkali-doped helium clusters. *Phys. Rev. Lett.* **1995,** *74*, 3592-5.
43. Stienkemeier, F.; Ernst, W. E.; Higgins, J.; Scoles, G., On the use of liquid helium cluster beams for the preparation and spectroscopy of the triplet states of alkali dimers and other weakly bound complexes. *J. Chem. Phys.* **1995,** *102*, 615-17.
44. Callegari, C.; Higgins, J.; Stienkemeier, F.; Scoles, G., Beam Depletion Spectroscopy of Alkali Atoms (Li, Na, K) Attached to Highly Quantum Clusters. *J. Phys. Chem. A* **1998,** *102*, 95-101.
45. Buzzacchi, M.; Galli, D. E.; Reatto, L., Alkali ions in superfluid 4He and structure of the snowball. *Phys. Rev. B: Condens. Matter Mater. Phys.* **2001,** *64*, 094512/1-094512/10.
46. Rosenblit, M.; Jortner, J., Dynamics of the Formation of an Electron Bubble in Liquid Helium. *Physical Review Letters* **1995,** *75*, 4079-4082.

Chapter 3 Characterization of helium droplets

In this chapter, some characterization experiments of our helium droplet source are presented. In section 3.1, I will present two experimental methods to confirm the existence of helium droplets. In the next section, the velocities of the helium droplet beam at different source temperatures are presented in a table and are compared with theoretical calculations. Lastly, simulation results of size distributions of pure helium droplets are presented, and two methods of measuring the sizes of ion doped droplets are introduced.

3.1 Detection of pure droplets

In our experiments, superfluid helium droplets are formed by free-jet expansion of ultrahigh purity helium gas through a small nozzle of 500 μm under a high pressure of P_0 = 50 - 65 bar and a low temperature of T_0 = 13 - 20 K. According to the phase diagram of helium, when the pulsed valve is operated under room temperature, only pure helium gas can be obtained from the isentropic expansion. Helium droplets can be produced when the temperature of the helium reservoir drops below 20 K. To detect and distinguish pure helium gas from helium droplets, we use a commercial fast ionization gauge (FIG) as shown in Fig. 3.1.

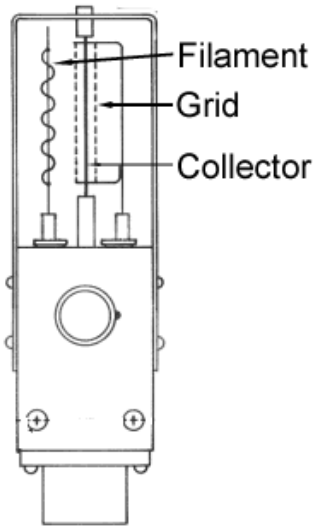

Fig.3.1. Schematic diagram of a commercial fast ionization gauge.

In this fast ion gauge, electrons are emitted from a heated filament and are attracted to the grid by a DC voltage of +150 V. Most electrons oscillate in and out of the grid, and during this oscillatory motion, they collide with and ionize any neutral molecule in the vicinity. The resulting charged particles are then collected by a central needle detector. The ion current, directly proportional to the concentration of neutral species in the vicinity, is amplified and converted into a voltage signal in-situ.

The response time of the ionization gauge is important in determining the intensity of a neutral molecular beam. Otherwise, only an average pressure rise in the vacuum chamber can be measured. The FIG uses a smaller grid than regular ionization gauges, and the amplifier for the ion signal is located directly underneath the ionization region. With both features, the response time of the FIG is on the order of microseconds.

During the experiment, we observed that when the source temperature was varied from 300 K to 13 K, the signal was delayed by 2.3 ms, as shown in Fig. 3.2.

Knowing the distance between the detector and the pulsed valve, and the response time of the FIG, we can then calculate the velocity difference under the two different conditions.

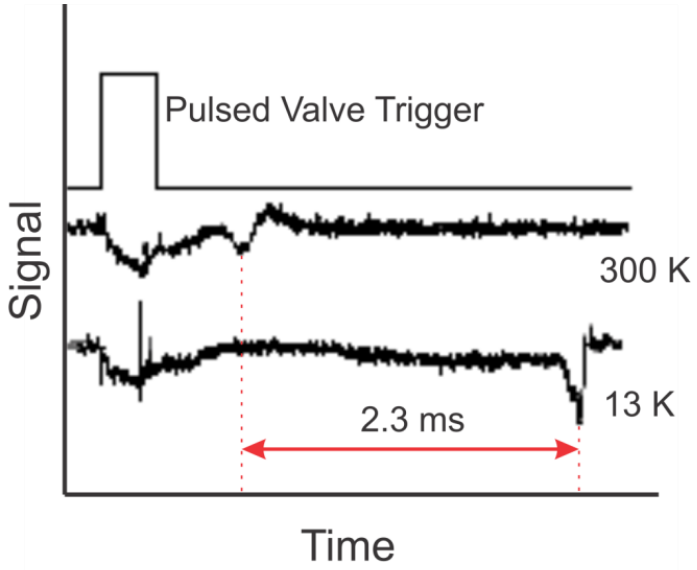

Fig.3.2. When the source temperature varied from 300 K to 13 K, the pulsed gas signal was delayed by 2.3 ms

Another method of investigating the formation of helium droplets is to use ion doped droplets. Without any droplet, there would be no pickup hence no signal from ion doped droplets. Only in the presence of droplet can ions be absorbed and carried into the detector region. This method is also used to measure the velocity of the droplet beam, as will be explained in the next section and in Chapter 5.

3.2 Velocity measurements

To measure the average velocity of a droplet beam, we can vary the location of the ion source-detector assembly and monitor the arrival time of the droplets. For

this method, we have to assume that the pickup process does not affect the speed of the droplet beam. The correlation between the position and arrival time is sufficient for velocity determination:

$$< v >= \frac{S_1 - S_2}{\Delta T_m}, \tag{3.1}$$

where S_1 (37 cm) is the distance from the nozzle to the first position of the ion source-detector assembly, S_2 (74 cm) is the distance from the nozzle to the second position, and ΔT_m is the difference in arrival time of the doped droplets on the target. The flight time of the doped droplet from the ion source to the detector is neglected because this gap is much smaller than the distance between the pulsed valve and the ion detector. The range of initial temperatures in our experiment is from 13 K to 20 K, which means that the droplets are formed by gas condensation. The theoretical velocity can be calculated by Eq. 2.11, which only depends on the initial source temperature. Table 3.1 shows the comparison between measured velocity and theoretical velocity of the pure droplet beam.

Table.3.1. The arrival times of doped droplets at two positions in the source temperature range from 13.2 K to 17 K. The measured velocity and theoretical velocity are calculated based on Eq. 3.1 and Eq. 2.11

Nozzle temperature(K)	Arrival time at P1 (ms)	Arrival time at P2 (ms)	Measured velocity (m/s)	Theoretical velocity (m/s)
13.2	1.405	2.402	371	375
14	1.360	2.300	388	380
15	1.325	2.23	400	393
16	1.290	2.178	411	406
17	1.250	2.114	422	419

At a fixed pressure of 50 bar, the measured velocity ranges from 371 m/s at 13.2 K to 422 m/s at 17 K. In comparison, the theoretical value based on Eq. 2.11 is from 375 m/s to 419 m/s. By changing the initial pressure from 35 to 65 bar, the velocity of the droplet beam has no detectable change. The agreement between theory and experiment is quite satisfactory.

3.3 Droplet size distribution

It is difficult to directly measure the size of helium droplets because the droplets are not charged and the atoms are loosely bound in a droplet. For droplets with less than 100 helium atoms, diffraction through a nano-scale transmission grating has been used based on the wave nature of any particle.[1-2] To analyze larger droplets containing more than 1000 helium atoms, deflection due to scattering by a monoenergetic atomic beam has been reported.[3-5] For doped droplets in some cases, the average size can be deduced by the pickup statistics based on the dopant concentration obtained from electron impact ionization[6] or laser-induced fluorescence.[7] For example, in the work of Yang *et al*,[6] droplet sizes have been deduced by exploiting the distribution of doped water clusters in droplets based on mass spectrometry. In the work of Slipchenko *et al*,[7] the average droplet size has been studied from the dependence of the LIF intensity on the pressure of a clustering agent argon in the doping chamber. Additional pick-up of Ar atoms causes formation of complexes of Ar and phthalocyanine, resulting in a frequency shift for absorption. Hence, the LIF intensity due to pure phthalocyanine embedded in droplets decreases with increasing Ar pressure.

In our project, we did not directly measure the size and size distribution of pure helium droplets. Instead, we simulated the size distribution in the temperature range of 14 K to 20 K according to the scaling parameter and the log-normal distribution (see chapter 2). Table 3.2 lists the parameters used in the simulation based on the experimental conditions, and Fig.3.3 shows the resulting distribution at each temperature. With decreasing nozzle temperature, the distribution gets narrower with larger sized droplets.

Table.3.2. Parameters in the simulation of helium droplet size distribution

Q	n_0 (/Å^3)	ν (cm^3/mol)	d (μm)	a_0 (m/s)	γ (N/m)	M (kg)	T_{ref} (K)	P_0 (bar)	A (bar)	σ
0.6	0.022	27.37	500	340	3.5×10^{-4}	6.68×10^{-27}	3.23	55	7.8	0.77

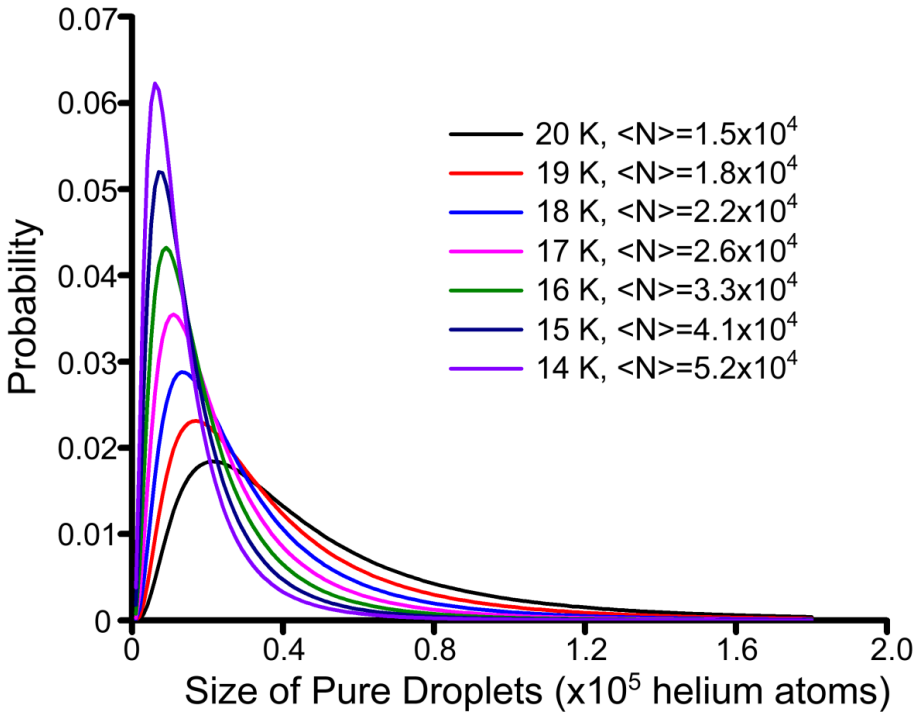

Fig.3.3. Simulation results of size distribution of pure helium droplets with varying source temperatures.

Experimentally, we only attempted to characterize the size distribution of ion doped droplets, since ion doped droplets are charged, and electrostatic manipulation becomes viable. Two direct methods have been used, including beam deflection and beam retardation. In the deflection experiment, we installed a set of deflectors parallel to the doped beam, and a small area charge detector perpendicular to the beam. As shown in Fig.3.4, with voltage U applied on the top deflector, a transverse velocity v_y is gained by the traversing ions. Depending on the mass-to-charge ratio, smaller ion doped droplets are deflected away from the detector. Thus a correlation between the detected doped droplets and a lower size limit can be established at each

deflection voltage. In our setup, the deflector electrodes are L_1 = 40 mm long and are separated by a distance D = 40 mm. The detector of S = 4 mm long is located L_2 = 60 mm downstream from the end of the deflectors. The bottom deflector electrode is grounded, while the top one is biased from -2200 V to +2200 V. The total deflection $S_1 + S_2$ depends on the original beam velocity V_x, the droplet mass m and charge Z:

$$\frac{1}{2}S = S1 + S2 = \frac{ZqU(L_1^2 + 2L_1L_2)}{2DmV_x^2} \tag{3.2}$$

Eq.3.2 provides a lower size limit for the detected ion doped droplets. For example, at U = +500 V, the corresponding lower size limit is about 6.7×10^6 helium/droplet.

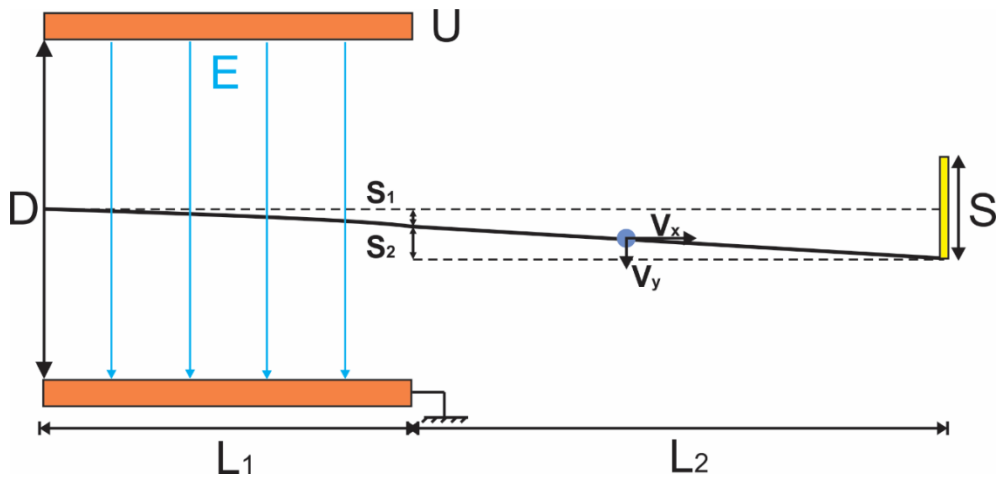

Fig.3.4. Setup of the electrostatic deflection experiment.

The second method to measure the size of doped droplets is to use a biased mesh as an energy filter. The kinetic energy of doped droplets depends on the droplet mass (size) and velocity. Since the droplets move at a constant group velocity after doping, only those with sufficient mass can pass through the biased retardation electrode. In this setup, the retardation electrode is made of a copper plate with a

central circular hole of 38 mm in diameter. The hole is covered with a fine mesh of 50 × 50 mesh plain and 0.025 mm in wire diameter. The current generated by the larger ions passing through the mesh can be measured by a copper target. To prevent the electric field of the retardation electrode from affecting the detection efficiency of the copper target for different sized ions, a coarse mesh of 16×16 mesh plain and 0.25 mm in wire diameter is placed 2 mm in front of the copper target. At a nozzle temperature of 14 K, each helium atom in the droplet has a kinetic energy of about 3.01 meV. To pass through the retardation electrode of 1000 V, the corresponding size of the doped droplet is about 3.3×10^5 helium/droplet.

The average size from the doping experiment of cesium (chapter 6) is 100 times larger than that of the pure droplets from calculation (Fig. 3.3) at a source temperature of 14 K. The difference is related to evaporation of helium atoms upon ion pickup and size dependent pickup efficiencies. An ion with a kinetic energy of 100 V requires 6.5×10^5 helium atoms to be cooled down to 0.38 K. This means that for droplets smaller than 6.5×10^5, all helium atoms will be evaporated in the cooling process, and only for droplets larger than 6.5×10^5, they can pass through the grid and be detected. In addition, smaller droplets have smaller pickup cross sections and hence are more likely to fail in picking up any dopant molecules. Moreover, the experimental setup is intrinsically discriminatory against smaller sized ion doped droplets because of the trapping potential for ions in the ion source: the trapping potential is also effective in preventing smaller doped droplets from escaping the doping region. When the grid is applied with a voltage of -200 V, only doped droplets containing more than 10^6 atoms can efficiently pass through the doping region and

arrive at the detector. All these factors tend to shift the average size of the doped droplets to a larger value.

3.4 Reference

1. Schoellkopf, W.; Toennies, J. P., Nondestructive mass selection of small van der Waals clusters. *Science* **1994,** *266*, 1345-8.
2. Kornilov, O.; Toennies, J. P., Matter-wave diffraction of quantum magical helium clusters. *Europhys. News* **2007,** *38*, 22-27.
3. Lewerenz, M.; Schilling, B.; Toennies, J. P., A new scattering deflection method for determining and selecting the sizes of large liquid clusters of helium-4. *Chem. Phys. Lett.* **1993,** *206*, 381-7.
4. Lewerenz, M.; Schilling, B.; Toennies, J. P., Successive capture and coagulation of atoms and molecules to small clusters in large liquid helium clusters. *J. Chem. Phys.* **1995,** *102*, 8191-207.
5. Harms, J.; Toennies, J. P.; Dalfovo, F., Density of superfluid helium droplets. *Phys. Rev. B: Condens. Matter Mater. Phys.* **1998,** *58*, 3341-3350.
6. Yang, S.; Brereton, S. M.; Ellis, A. M., Controlled growth of helium nanodroplets from a pulsed source. *Rev. Sci. Instrum.* **2005,** *76*, 104102.
7. Slipchenko, M. N.; Kuma, S.; Momose, T.; Vilesov, A. F., Intense pulsed helium droplet beams. *Rev. Sci. Instrum.* **2002,** *73*, 3600-3605.

Chapter 4 ESI source

Doping of protein ions requires an electrospray ionization source. For this purpose, we have taken and modified a surplus mass spectrometer (BioTOF, Bruker Daltonics). The time-of-flight segment of the BioTOF is replaced by our own detection and analysis components for doped droplets, and a new interface is created between the ESI source and our droplet source. The Fig. 4.1 is a schematic description of the ESI system including the ion source and the downstream quadrupole system.

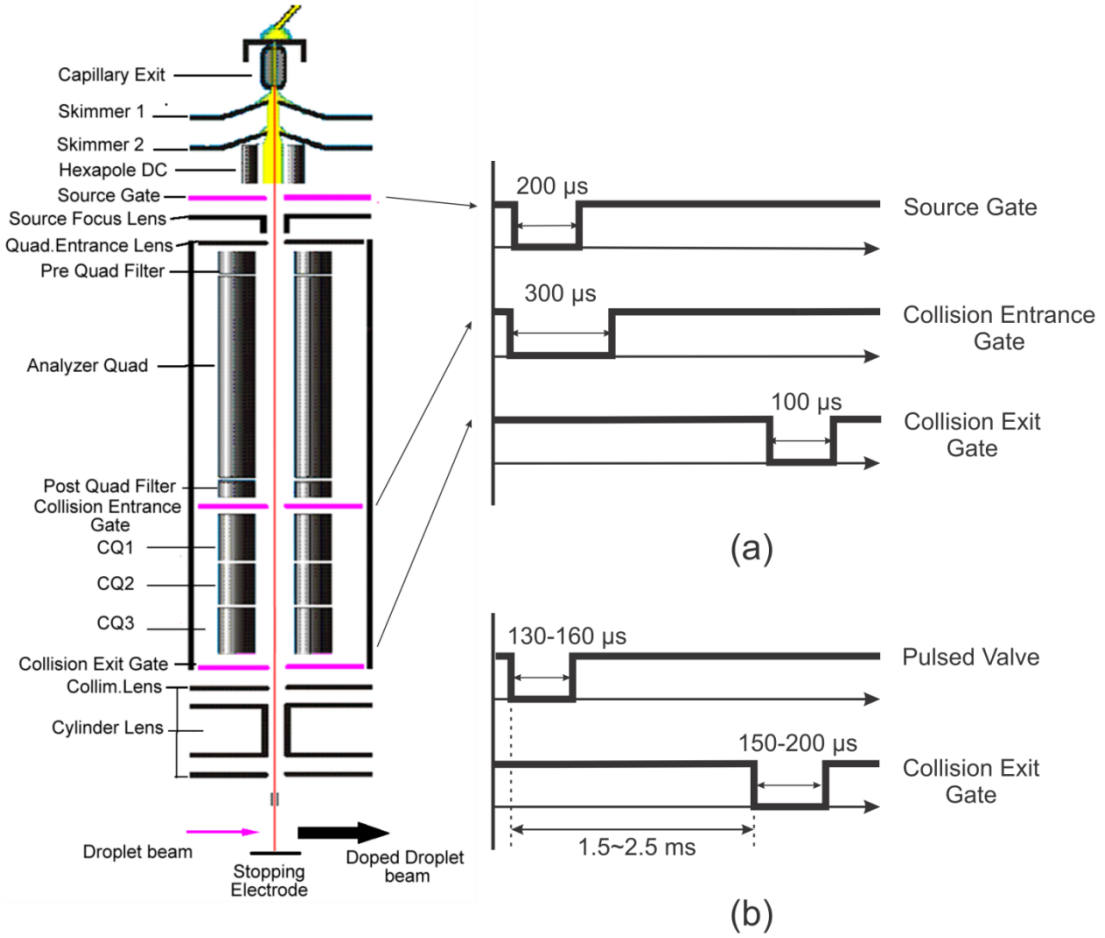

Fig.4.1. Left side: a schematic description of the ESI system including the ion source and the downstream quadrupole system. Right side: time sequence. (a) the original pulse sequence of the source gate, collision entrance gate and collision exit gate. (b) the source gate and the collision entrance gate are kept the same, but the collision exit gate is about 1.8 ms after the trigger of the pulsed valve.

4.1 Electrospray ionization

Electrospray ionization is a soft ionization technique for generating and transferring ions from solution into the gas phase. The mechanism of electrospray ionization is shown in Figure 4.2.

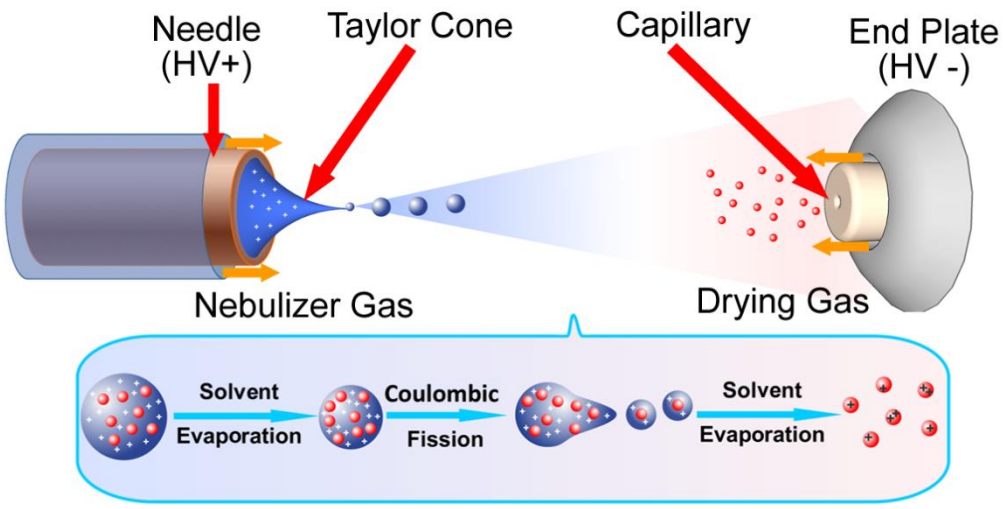

Fig.4.2. Schematic of electrospray ionization.

The sample of interest was dissolved in an appropriate solvent and then pushed into a metal capillary (needle) by a glass syringe (SGE Analytical Science, 500R-GT-LC), which was driven by a syringe pump (Kd Scientific, 781100). Typically, the optimal speed of sample spray in our experiment was about 100-200 µl/hour. In our instrument, the needle was biased at ground, and the endplate and capillary were set to a voltage of about -4 kV to -5 kV. As a result of the potential gradient between the needle and the endplate, partial separation between positive and negative electrolyte ions occurred at the tip of the needle. In the positive ion mode, when the sum of the repulsive forces between the positive ions at the surface and the attraction from the electric field was larger than the surface tension, the liquid will form into a cone -- the Taylor cone.[1] Highly charged droplets were then released from the Taylor cone and continued to reduce their sizes by solvent evaporation during flight toward the analyzer region of the mass spectrometer. Concurrent with the flow of the solution

droplet, a nebulizer gas (N_2) at a pressure of ~35 psi was applied to assist with droplet release from the Taylor cone. In the opposite direction, a stream of nitrogen drying gas with a temperature of 200^{o}C was added to aid with the size reduction of the liquid droplet. Solvent evaporation led to increased surface charge density. When the droplet radius was decreased close to the Rayleigh limit, Coulombic repulsion between charges on the surface would overcome the surface tension and induce fission:

$$q_s = 8\pi(\varepsilon_0 \gamma R^3)^{1/2} \quad (4.1)$$

where q_s is the surface charge, ε_0 is the vacuum permittivity, γ is the surface tension and R is the droplet radius. For example, when the droplet radius for an electrolyte NaCl was 0.28 μm, the number of charge on the surface was 1.3×10^4.[1] This process of size reduction and Coulomb fission repeated in cascade, until bare ions were left. The emitted ions were then collimated by a skimmer cone and then were accelerated into the hexapole ion guide.

4.2 Quadrupole mass filter and/or ion trap

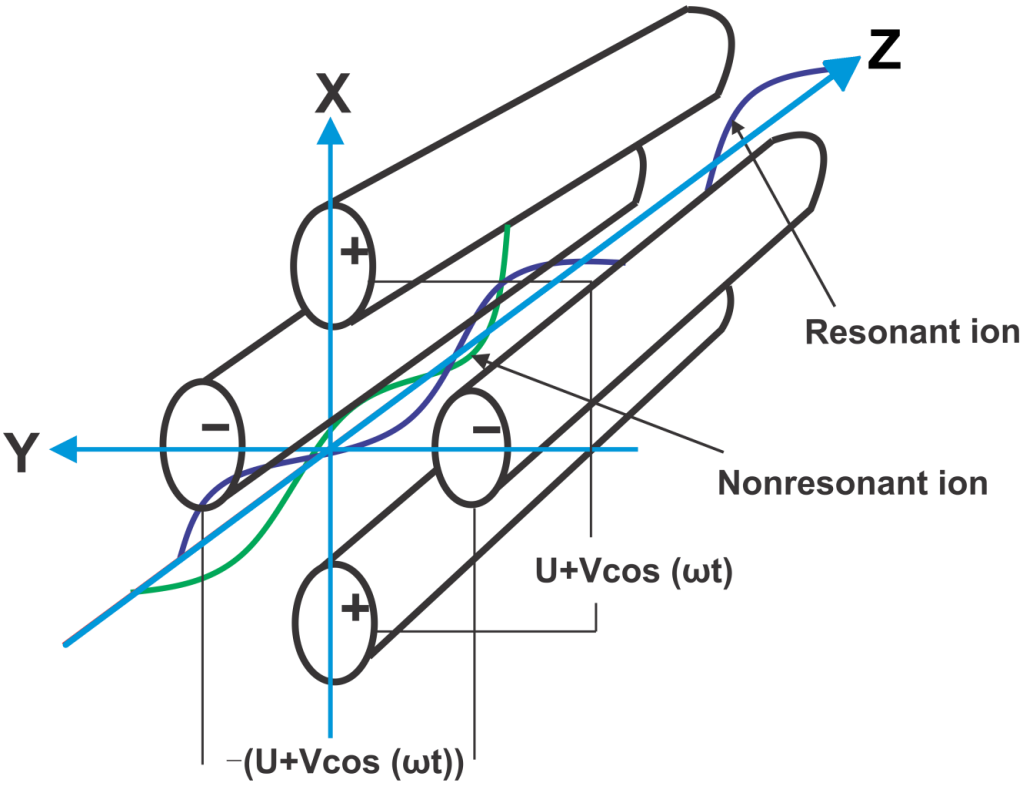

Fig.4.3. Schematic of a linear quadrupole mass filter. Resonant ions (blue trace) pass through the quadrupole, while nonresonant ions (green trace) are eliminated by either colliding with the poles or escaping from the gap between the poles.

A quadrupole mass selector is widely used in mass spectrometry. It consists of 4 parallel metal rods arranged in a circle separated by a specific distance as shown in Fig. 4.3, and each pair of rods is connected with a DC and a RF power supply. One pair of rods has a potential of U+Vcos(ωt) and the other has a potential of opposite polarity –(U+Vcos(ωt)), where U is the DC voltage and Vcos(ωt) is the AC voltage with an amplitude V and a frequency ω. In the x-z plane of Fig.4.3, the movement of the ions varies with the electric field and can be determined from Mathieu's differential equation,

$$\frac{d^2x}{d\tau^2} + (a_x + 2q_x cos2\tau)x = 0 \qquad (4.2)$$

where we define parameters τ, a and q such that $\tau = \frac{\omega t}{2}$, $a = \frac{4eU}{\omega^2 r_0^2 m}$, $q = \frac{2eV}{\omega^2 r_0^2 m}$ and a/q = 2U/V. Here, m is the mass of an ion, e is the charge of an ion, r_0 is the distance from the center axis (z axis) to the surface of any electrode. For an ion with a mass-to-charge ratio determined by m/e, in a fixed frequency RF field, solutions of the Mathieu's differential equation contain both bound (stable traces within the spaced confined by the rods with $x < r_0$,) and unbound traces (unstable traces with ions hitting the electrodes or escapes from the space between the rods, $x > r_0$) depending on the biases on the rods. The bound solutions form a region of stability, as shown in Fig.4.4. As long as the voltage settings on the rods for the chosen ion are within the stable region (shaded area), the chosen ions can pass through the mass selector.

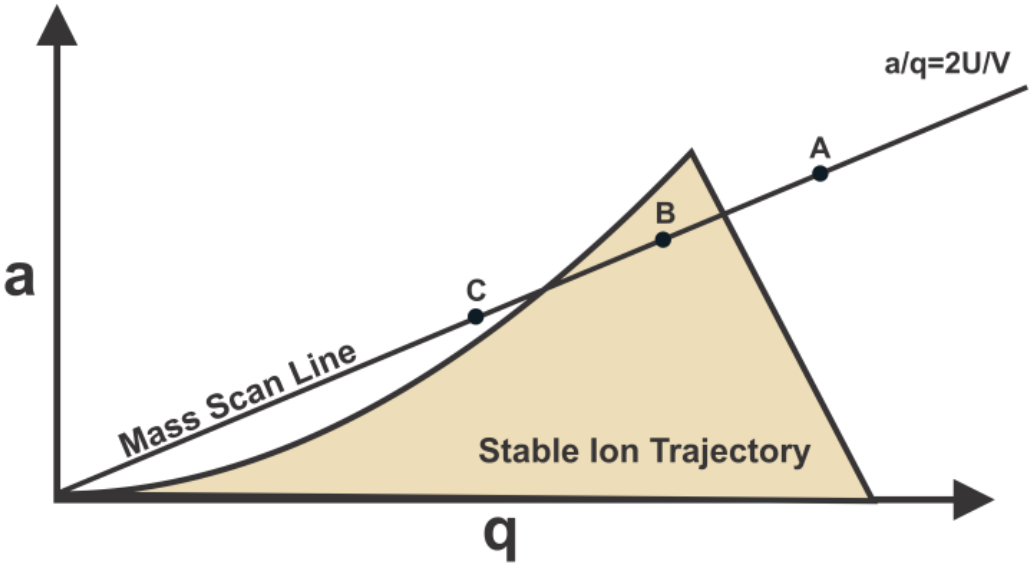

Fig.4.4. Stability diagram of a quadrupole mass selector. A mass scan line is also shown.

The region of stability is dependent on the mass-to-charge ratio of an ion, hence different ions are stable at different a or q values forming different shaded areas on the figure. The slope of the mass scan line is defined as $\frac{a}{q} = \frac{2U}{V}$. By scanning the values of a or q while maintaining the same a/q ratio, only ions with a specific mass-to-charge ratio (point B on the mass scan line in Fig. 4.4) trace a stable path within the volume of the quadruple and pass through the quadrupole without hitting the rods or escaping the confines of the rods. Hence only these ions are guided out of the quadruple and are detected.[2-3]

On the other hand, when only RF bias is supplied to the quadrupole, all ions with stability regions containing the corresponding q value of the RF field can pass through the quadrupole. This is the basic principle of a quadrupole ion guide. It is important to note that in this mode of operation, not all ions can pass through the ion guide, since the RF field defines the value of q, and ions with stability regions outside the value of q are still going to be terminated inside the ion guide.

The same design is also used to trap ions inside the volume of a quadrupole set. This is achieved by adding two gate electrodes usually a few Volts above the DC voltage on the rods for longitudinal trapping. However, as the ions move inside the space confined by the rods powered by RF fields, they can escape the confinement of the rods by gaining kinetic energies from the RF field over time. For this reason, operations of a quadrupole ion trap require the presence of a collision gas to reduce the kinetic energy of the trapped ions.[3-4]

In the BioTOF, a quadrupole mass analyzer is located downstream from the ESI source, and three tandem quadrupoles (triple quad) are located further downstream. These quadrupoles can be used as traps, for ion storage or for collision-induced dissociation. These quadrupoles are shown as CQ1, CQ2 and CQ3 in Fig.4.1. During operation, the vacuum level of the triple quad changes from 2×10^{-6} torr to 2×10^{-5} torr when the nitrogen collision gas is introduced. Typically the quadrupoles are driven with an RF voltage of 200 V_{p-p} at 1.0 MHz and a DC voltage of 20 – 50 V for the mass range between 400 – 2000 Dalton.

The BioTOF can be operated in two different modes: MS and MS/MS. In the MS mode, the analyzer quadrupole operates with RF only, i. e. as an ion guide for transmission. Then the ions are stored in the triple quad cooled by dry nitrogen. Collisions with room temperature gas reduce the divergence in the velocity of the trapped ions, which improves the resolution of the Time-of-Flight analyzer of the original mass spectrometer. This feature is also beneficial to our own ion doping experiment, for synchronization with the pulsed droplet beam, and for efficient control of trajectories and energies during doping. In the MS/MS mode, the analyzer quadrupole functions as a mass filter to select a specific precursor ion. Then the ions are introduced into the triple quad for collisional fragmentation, and the resulting fragments are analyzed by the original TOF analyzer. For our application, this mode of operation could be used to choose a particular charged state of a protein from the ESI source, although at the present stage with small peptides and other molecules, this feature is not being used.

4.3 Electrostatic focusing with an Einzel lens

To focus or collimate a diverging ion beam, Einzel lenses are typically used. An Einzel lens consists of three or more coaxial cylinders with the same opening. In most cases, the two end cylinders are biased at the same potential, generating a symmetric electric field in the ion path. Therefore, this lens set has no net acceleration and is hence named "Einzel lens".[5] The focusing effect of an einzel lens depends on the combination of cylinder lengths, voltages and openings.

In the BioTOF, an Einzel lens containing two plate electrodes (collimator lens) set at the same voltage of -35 V and a cylindrical metal tube (cylinder lens) at -250 V sandwiched in between, as shown in Fig.4.1, is located downstream from the triple quad. By tuning both voltages, ions with different energies can be collimated and/or focused to provide the most efficient overlapping with helium droplets, resulting in most efficient doping.

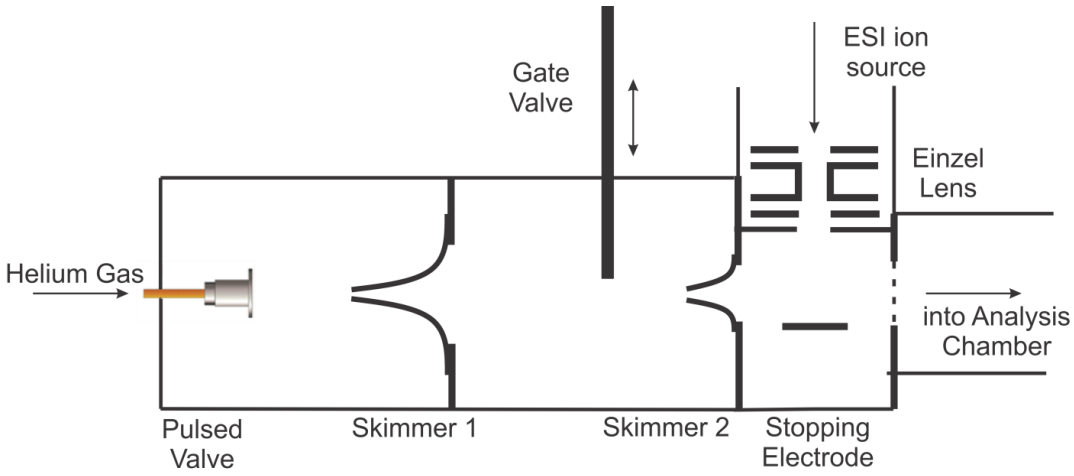

Fig.4.5. The interface region between the droplet source and the ESI ion source.

Fig. 4.5 shows the interface region between the droplet source and the ESI ion source. A gate valve separates the droplet source from the ion source for independent diagnosis. Helium droplets generated from the pulsed valve and collimated by skimmers 1 and 2 are directed into the doping region. Skimmer 2 has the additional effect of limiting the gas load of the doping region for ion pickup. Mass selected ions from the ESI source are focused into the doping region by the Einzel lens. The ion beam can be stopped and/or slowed down by a biased stopping electrode. The doping chamber and the analysis chamber are separated by a grounded ring electrode covered with a mesh. After doping, the ion-doped droplet passes through the mesh into the analysis chamber.

In our adaption, released ions from the ion trap passed through the Einzel lens into the path of the droplet beam. In Fig.4.1(a), the original control program of the BioTOF limited the repetition rate to be above 30 Hz. However, to synchronize with the pulsed valve of the helium droplet source at 10 Hz, the exit gate with an opening duration of 150~200 μs was now triggered by a delay generator (EG&G Princeton applied research, 9650A) 1 - 2 ms after the trigger of the pulsed valve, as shown in Fig.4.1(b). The exact timing of the exit gate was dependent on the temperature of the pulsed valve, and at 15 K, the delay time was 1.8 ms.

4.4 Characterization of the ESI source: absolute ion count

In the doping region, a collector electrode of 36 mm × 36 mm made of stainless steel was placed 4 mm off the path of the droplet beam and aligned with the

ion beam, as shown in Fig.4.1. Two methods with different degrees of amplification were used to measure the total number of ions outside the ESI assembly: one was to use a charge sensitive amplifier (CoolFET, A250CF), and the other was to use an oscilloscope through a DC blocking capacitor of 3000 pF. The circuit diagram for the latter is shown in Fig.4.6. The capacitor allowed the oscilloscope to watch voltage variations on the target independent of the bias voltage. The pulsed ion current coming from the target was shared unequally between the oscilloscope and the bias power supply. Because the impedance of the blocking capacitor and the oscilloscope was much less than that of the bias circuit (44 megaOhms), most of the pulsed current arrived at the scope for measurement.

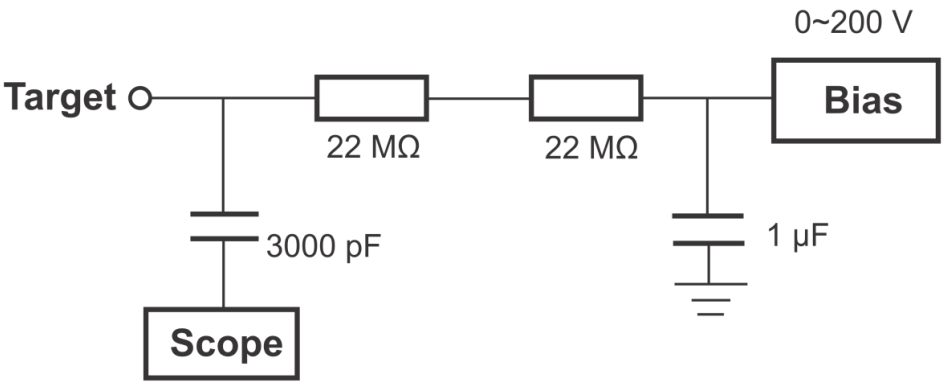

Fig.4.6. Circuit diagram for measuring the number of ions from the ESI source.

During the experiment, the charge amplifier was typically used first when optimizing the conditions for generating ions, because of its higher amplification capability and better signal-to-noise ratio. However, when the voltage signal from the charge amplifier reached 4 V, the charge amplifier was saturated, and the oscilloscope had to be used. Bias on the stopper electrode was typically applied during the doping

experiment: the voltage was to slow down, stop and even return the incoming ions hence to increase the doping efficiency (chapter 7).

4.5 Reference

1. Kebarle, P., A brief overview of the present status of the mechanism involved in electrospray mass spectrometry. *J. Mass Spectrom* **2000,** *35*, 804-817.
2. Miller, P. E.; Denton, M. B., The quadrupole mass filter: Basic operating concepts. *Journal of Chemical Education* **1986,** *63*, 617.
3. Gross, J. H., *Mass Spectrometry*. Springer: New York, 2011.
4. Bierau, F.; Kupser, P.; Meijer, G.; von Helden, G., Catching proteins in liquid helium droplets. *Phys. Rev. Lett.* **2010,** *105*, 133402.
5. Sise, O.; Ulu, M.; Dogan, M., Multi-element cylindrical electrostatic lens systems for focusing and controlling charged particles. *Nuclear Instruments and Methods in Physics Research Section A: Accelerators, Spectrometers, Detectors and Associated Equipment* **2005,** *554*, 114-131.

Chapter 5 Experimental setup

The technique of generating superfluid helium droplets doped with various charged particles has recently been developed for many research applications. We began our pursuit with the ultimate goal of chilling protein ions for laser induced alignment and then electron diffraction. To minimize the technical barrier, we started with a continuous ion source of cesium ions from a thermionic source (chapter 6), and then progressed to the pulsed ion source of our electrospray ionization mass spectrometer (chapter 7). Along this quest, we have learned the key factors in affecting the doping efficiency of helium droplets, and we have also measured the size distribution of the resulting ion doped droplets. After learning that the doped droplets contain too many helium atoms, we have also devised a method to size-reduce the doped droplets (chapter 8).

This chapter starts with a general description of the fundamental idea of our experimental setup, followed by a detailed description of our pulsed superfluid helium droplet source and the two types of detectors for measuring pure cesium ions and doped droplets. At the end of the chapter, an introduction to the two experiments of doping cesium ions and doping ions from the ESI source will be given.

5.1 General description

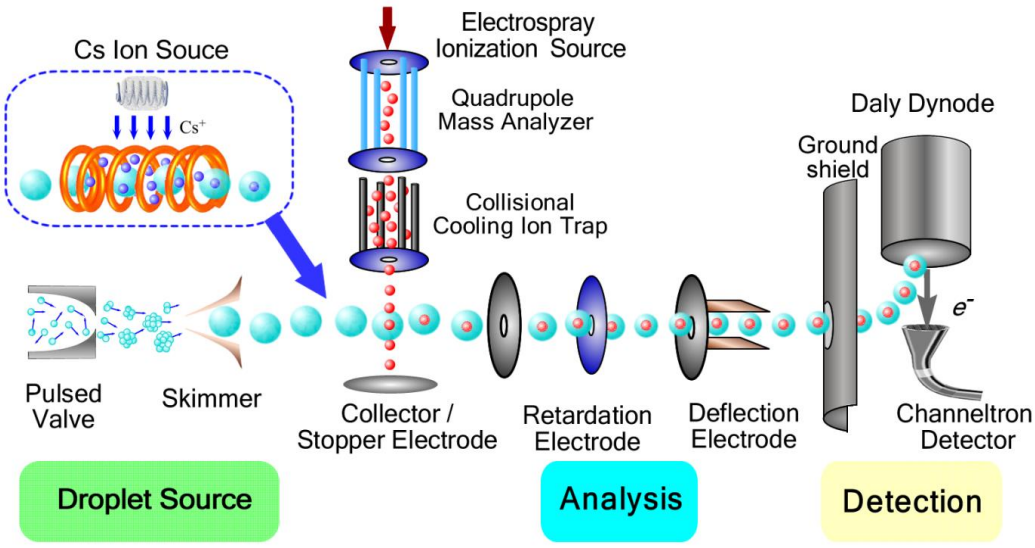

Fig.5.1. Experimental setup for doping cesium cations and ions from an ESI source. The characterization methods including deflection and retardation are also illustrated.

Figure 5.1 shows the general setup of the experiment, including two different ion sources: the continuous thermionic cesium ion source in the inset, and the ESI source. In the experiment of cesium ions, the electrospray ionization source only offered a vacuum chamber for the cesium ion source, and the Daly-type dynode detector was replaced by a copper target wired to an operational amplifier and a giga-Ohm resistor. The abundant number of doped ions generated voltage pulses on the copper target of more than several milliVolts, sufficient for an oscilloscope and computer to digitize and record. For the doping experiment of ESI ions, the cesium ion source was removed and the Daly-type dynode detector was mounted downstream from the deflection electrodes. The gain of the Daly-type dynode detector was necessary to record less than 10,000 doped ions. In both experiments, after picking up the species of interest, all internal and kinetic energies of the charged particles

would be released into the helium droplet and ultimately removed by evaporation of helium atoms on the surface of the droplet. Therefore, compared with the pure helium droplet, the size and the size distribution of doped droplet should change.

To investigate the size distribution of the doped droplets, two different setups were used. The first one was a deflection experiment as shown in Figure.5.1. A set of deflection electrodes was positioned downstream from the doping region but upstream from the detectors. One of the electrodes was grounded, while the other was biased from -3 kV to +3 kV. With increasing voltage on the second deflector, small doped droplets with small kinetic energies were driven away from the detector. Therefore, we can set up a correlation between the detected doped droplets and a lower size limit at each deflection voltage. The second experiment of determining the size distribution of doped droplets was an energy filter experiment where a mesh-covered retardation electrode is biased. Similar to the principle of the deflection experiment, different sized droplets would have different kinetic energies assuming all doped droplets have a constant group velocity. Only those ions with sufficient kinetic energies can pass through the biased retardation electrode and hit the target.

5.2 Pulsed superfluid helium droplet source

We used a highly pressurized pulsed valve cooled down by a cryogenic cryostat to produce superfluid helium droplets. Six major components constitute the droplet source: a cryogenic pulsed valve, a closed-cycle helium cryocooler, a temperature sensing and regulating system including a heater that can actively

stabilize the temperature of the pulsed valve, a skimmer which collimates the droplet beam, high purity (99.999%) high pressure (60 bar) helium (Airgas, UHP 300) with a pressure regulator (Airgas, Y11-N114G), and a high vacuum system evacuated by appropriate pumps.

We used a solenoid pulsed valve (Parker Hannifin Corp, Series 99) to generate superfluid helium droplets. The cross sectional schematic drawing of the valve is shown in Fig.5.2. Unique to this valve is the poppet made of PCTFE (Polychlorotrifluoroethylene), which had a low coefficient of thermal expansion and was able to satisfy repetitive use at extreme low temperatures. In addition, a copper gasket (instead of an O-ring) was used for sealing between the face plate and the valve body. Generally, the pulsed valve was operated at 10 Hz with a duration of 130-145 μs driven by its own controller (Parker Hannifin Corp, IOTA One), and the controller provided a voltage of 12 Vdc and a current of 1000 mA.

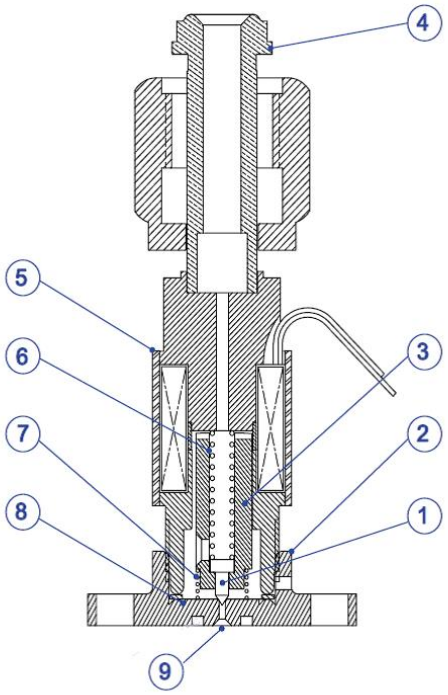

Fig.5.2. Interior of a solenoid pulsed valve series 99. (1) poppet, (2) valve body, (3) armature, (4) VCR fitting, (5) coil assembly, (6) main spring, (7) buffer spring, (8) gasket, (9) orifice in the nozzle.

The faceplate of the pulsed valve was home-made. One configuration of the commercial nozzle had a channel of 0.5 mm dia. that tapers to a constriction of 0.25 mm dia. on the exit side, as shown in Fig. 5.3(a). The straight channel constricted the acceleration of the subsonic flow into the sonic beam before the free-jet expansion, which also limited the control of the droplet size, particularly for large sizes droplets. This design would cause destruction of droplets and limit droplet sizes by heating. *Slipchenko et al*[1] used a 3 mm long cone shaped hole with a short conical opening toward the poppet and a ~90º opening for the exit, shown in Fig. 5.3(b). This modification increased the intensity of their fluorescence signal by a factor of 10 and also allowed for operation in temperatures between 12 and 20 K. Yang *et al*[2] further flattened the sharp junction into a short constriction as shown in Fig. 5.3(c), and the

result was more efficient control of the droplet size and size distribution. We took the original faceplate from Parker Hannifin and machined a ~90^{o} 2 mm long conical opening on the exit side of the faceplate, starting from the 0.5 mm dia. channel, as shown in Fig. 5.3(d). The resulting droplet beam had been stable and intense enough for doping of cations, as will be shown in the following chapters.

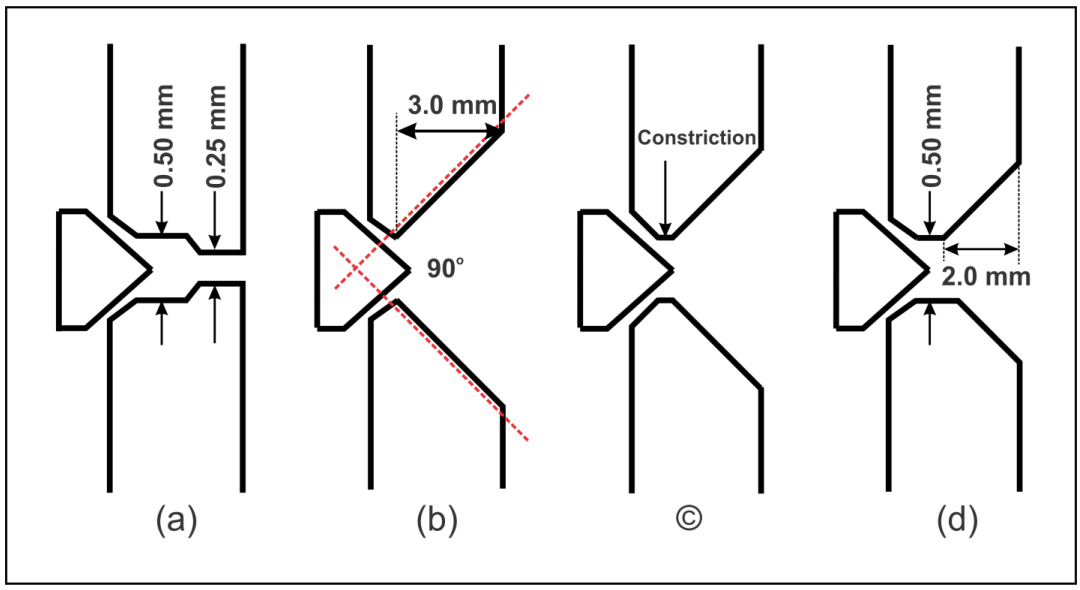

Fig.5.3. Four different shapes of the nozzle of pulsed valves. (a) Original face plate from Parker Hannifin, General valve, series 99. (b) Nozzle with a 3 mm long conical cone of 90^{o}.[1] (c) Conical entrance and exit openings with a short constriction.[2] (d) Nozzle with a 0.5 mm dia. constriction and 2 mm long 90^{o} conical cone.

Figure 5.4 shows the pulsed valve mounted on a cold head (DE-204SL, APF cryogenics). A homemade U-shaped copper adaptor with an internally sealed channel was mounted on the bottom of cold head. One end of the sealed channel was connected to a 1/8”copper tube which was coiled around the cold head, and the other end of the channel was connected to the entrance of the pulsed valve by a short 1/16”

stainless steel tube. Helium gas was routed into the coiled tube around the cold head for precooling before being sent to the pulsed valve. Both the cold head and the pulsed valve were encased inside a heat shield to reduce the heat exchange with the environment. In order to improve the thermal contact between the pulsed valve and the cold head, indium sheets were applied among copper supporting plates and holders for the pulsed valve body and faceplate.

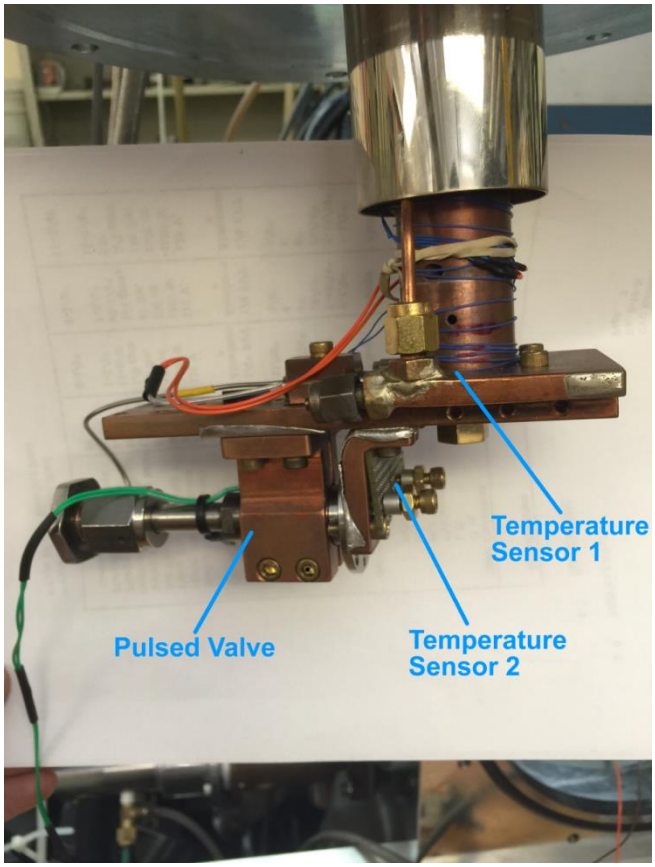

Fig.5.4. Pulsed valve assembly attached to a cold head to generate superfluid helium droplets.

In Fig. 5.5, the cold head was mounted on a flange that can be adjusted in one direction, and this smaller flange was sitting on a larger 12” flange of the vacuum

chamber. The distance between nozzle and skimmer can be adjusted by shifting the smaller flange along the direction of the droplet beam.

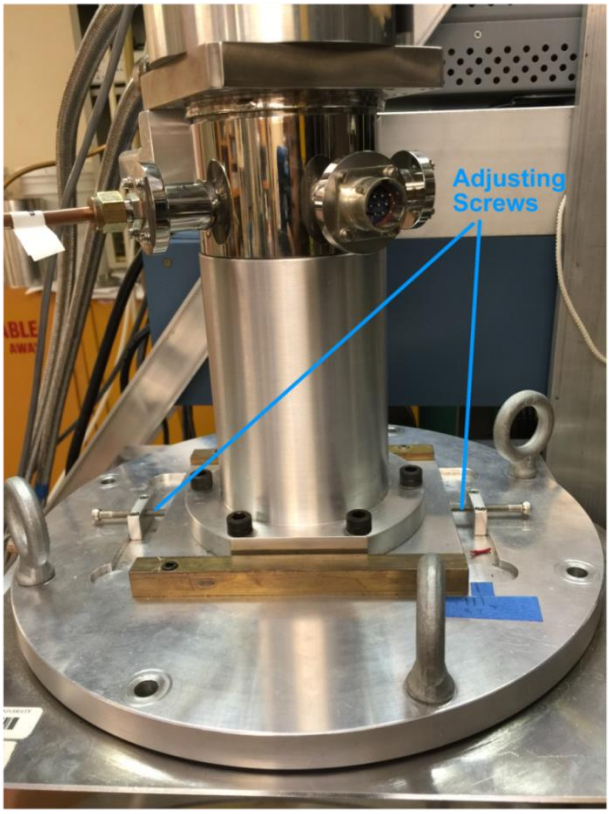

Fig.5.5. The cold head is mounted on a smaller flange whose position can be adjusted by shifting its position on top of the larger 12” flange.

A two-stage cryogenic refrigerator (compressor model: HC-4 MK1, APF cryogenics) with a cooling capacity of 17 W at 77 K for the first stage and of 9 W at 20 K for the second stage was used for cooling of the pulsed valve. The specified total cool-down time for the second stage from room temperature to 20 K was approximately 30 minutes. However, because of the heat load of the pulsed valve and

heat loss in the chamber, the actual cool-down time was about 3 hours to obtain a final temperature of 13 K.

In Fig. 5.4, two silicon diode temperature sensors (Lake Shore, DT-470 SD) were used to monitor the performance of the cryostat, one attached to the faceplate of the pulsed valve and the other inserted into the bottom of the second stage of the cold head. A heater (Lakeshore, H712-25) was mounted on the top of the supporting plate to adjust the nozzle temperature between 13 K and 20 K. The temperature sensors and heater were driven by a temperature controller (CryoCon, 32 B). When set at a temperature between 13 K and 20 K on the controller, the temperature fluctuation read from the controller was up to 0.5 K. Although the two sensors should read about the same temperature, occasionally a difference of up to 10 K between the two sensors had been observed. Insufficient thermal contact might be a reason for the difference. In our experiment, the source temperature T_0 was read from the sensor attached to the second stage of the cold head.

A commercial skimmer (Beam Dynamics) of 5 cm length and 2 mm diameter was located 12 cm downstream from the nozzle for collimation of the helium droplet beam. The skimmer sat in a short aluminum tube and its position was adjusted by two vacuum compatible picomotor actuators (Newport, 8302-V) which were driven by a picomotor ethernet controller (New Focus, 8752-kit). The skimmer assembly is shown in Figure 5.6.

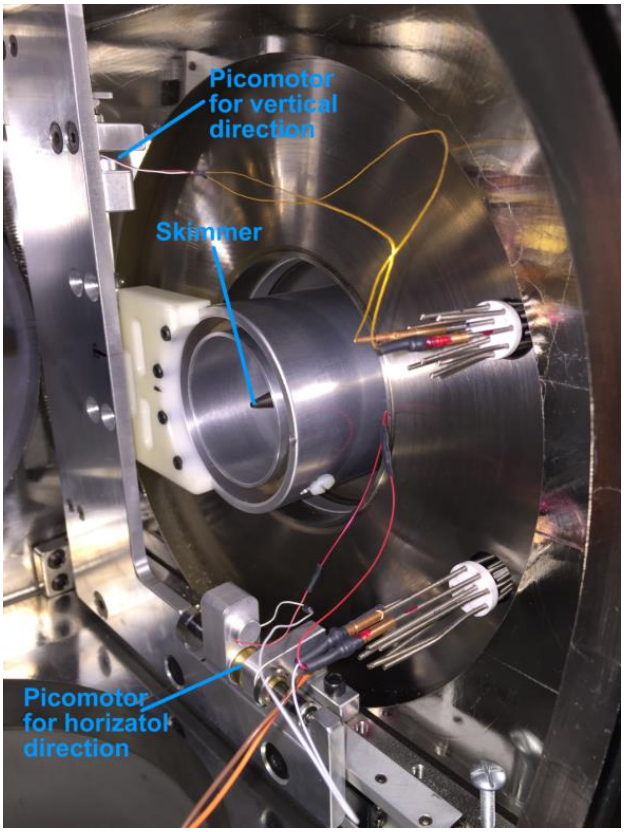

Fig.5.6. The skimmer sits inside a short tube and its position in the plane perpendicular to the beam can be controlled by two picomotors.

The source chamber of the droplet beam consisted of two interconnected high vacuum chambers pumped by two diffusion pumps (VHS-6 and Edwards-160) backed up by two mechanical pumps (Edwards, E2M28 and Alcatel, M2012A). One chamber (connected to the VHS-6 pump) housed the pulsed valve assembly, while the other was equipped with a hot cathode high vacuum gauge, and its function was only to offer an extra volume for the released gas load. The pumping speed of the VHS-6 for helium was ~3000 l/s, while the pumping speed of the Edwards-160 was 700 l/s for nitrogen and 1300 l/s for hydrogen. At a foreline pressure of 10^{-2} Torr, we turned on both diffusion pumps and after 4 hours, the source chamber reached a

pressure of 4×10^{-7} Torr. When the pulsed valve was on, the vacuum level read from the ionization gauge in the adjacent chamber dropped to 4×10^{-6} Torr. Although the opening time of the pulsed valve at different source temperatures can be modified to optimize the properties of the droplet beam, we typically limited the vacuum level in the source chamber to be better than 2×10^{-4} Torr.

5.3 Ion detectors

Our experiment required absolute ion counts, and our charged species have large masses, on the order of megaDaltons and higher. These two special conditions rendered typical microchannel plate or channeltron detectors inadequate, because these detectors had unknown magnifications, and their sensitivities diminish with increasing particle masses. A specially designed high mass detector from Ardara Technologies failed to detect any doped droplets, and no other commercial detectors were readily available. We had used two different types of detectors for our application, and detailed operational principles of these detectors are explained in the following sections.

5.3.1 A metal target for absolute ion count

The absolute number of ions or ion doped droplets hitting a conductor can be measured by wiring it to a home-made circuit including resistors and operational amplifiers (op-amp). Throughout the work of this thesis, we used two different versions of this type of detectors, and Fig. 5.7 shows the version with a lower gain. This circuit had been used to measure the number of cesium ions hitting the grid in

the ion source (Fig. 5.10), or the number of ions from an ESI source. During operation, when cations hit the target, the corresponding current would flow through the 1.0 megaOhm resistor, generating an input voltage V_{in}. Since the op-amp was connected as an output-follower, its output voltage V_{out} was equal to V_{in}. If the ion source was continuous, the output from the op-amp should be a DC voltage, and it can be directly measured using a digital voltmeter.

During the experiment, the conductor can be biased to any negative voltage up to -400 V to attract cations. The switchable 68 kOhm resistor allowed the measurement of higher target currents due to the limited output swing of the op-amp. The +/-6V power supply powered the op-amp, and it also floated at the bias voltage. The 100 kOhm resistor on the positive input of the op-amp was to prevent accidental damage to the op-amp.

The total absolute number of cesium ions can be derived from V_{out}. For example, when V_{bias} was -100 V and V_{out} was1.5 V, the target current was 1.5×10^{-6} A, which equals to 10^{13} ions/second.

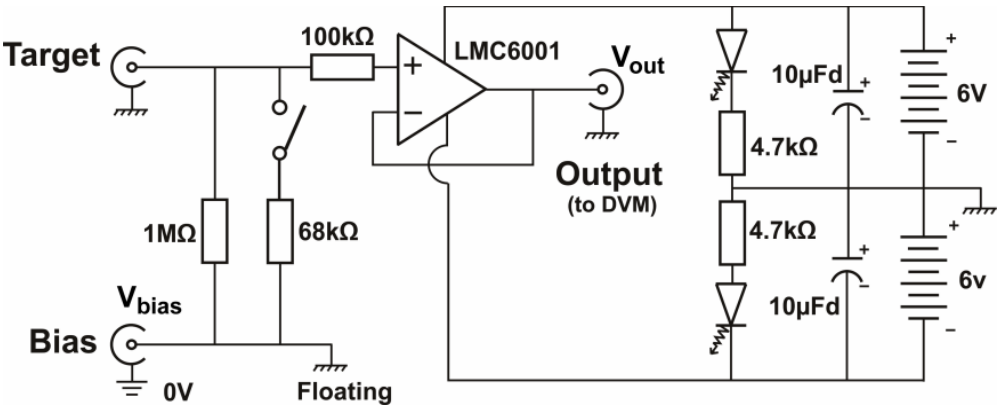

Fig.5.7. Circuit diagram for measuring the absolute number of cations hitting a conductor.

For doped droplets, a higher detection sensitivity was needed because of the lower number of ions. We therefore use a bigger resistor with an amplification circuit, as shown in Fig. 5.8. Ion-doped droplets hitting the copper target create a current which flows through the 1.0 gigaOhm resistor. The positive input of the LMC6001 op-amp was grounded and the negative input allowed the copper target to be held at virtual ground. The output buffers the voltage drop due to the current going through the 1.0 gigaOhm resistor. Hence, the voltage at output_1 was 1.0 Volt/nanoA.

The middle part of the circuit was a DC filter, which amplified only the time-varying component of the signal. The two integrated circuits on the right side of the diagram used op-amp LF353 to achieve an inverted amplification of 100 fold. The output voltage at Output_2 can be described as

$$V_{out} = -\frac{R_f}{R_i} \cdot V_{in} \,. \tag{3.1}$$

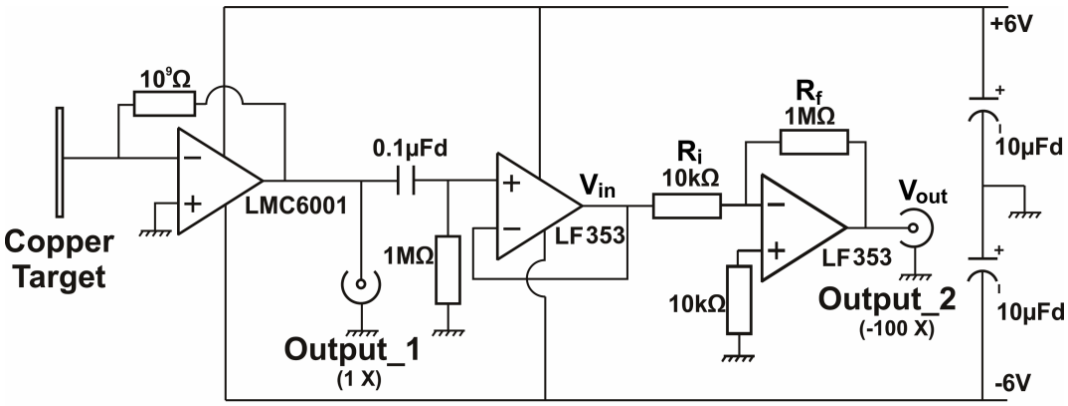

Fig.5.8. Circuit diagram for detecting ion pulses with a gain of x100.

Advantages of this type of detectors included adjustable sensitivity, absolute ion number reading, and mass-independent detection. Since the number of doped-

droplets was much smaller than the number of pure cesium ions, we can use a bigger resistor (1.0 gigaOhm instead of 1 megaOhm) to improve the sensitivity of the detector. The detector directly provided the ion current, without any calibration. Lastly but not the least, the detector was compact and portable, and it can be easily located anywhere suitable in the vacuum chamber. However, a major drawback of this type of detectors was their slow time response, limited by the large resistors. Consequently, the magnitude of the voltage pulse was limited, and the calculation of total ions required integration of the whole trace, and the time resolution was on the order of milliseconds, a far cry from the typical microsecond time scale of ion movements.

5.3.2 Daly-type dynode detector

For even lower ion counts, more magnification was needed. The Daly-type dynode detector offered a much higher magnification capability than our own circuit, and it was the only known detector that could potentially detect megaDalton ions. It consisted of an off-axis stainless steel (SS) block with a concave cutting on the bottom biased at a high voltage, and a channeltron detector opposite the SS block as shown in Fig. 5.9. The detector was typically shielded by a half can fabricated in stainless steel to prevent the ion beam from being deflected too quickly by the high voltage, and all metal parts inside the shield were highly polished to prevent electrical discharge. During operation, doped droplets passing through the circular aperture of 12 mm in diameter on the shield were accelerated and deflected toward the SS block, and secondary electrons were emitted and detected by the channeltron. The bias

voltage on the SS block, typically set to -20 kV, was introduced into the detection chamber by a HV power feedthrough. The bias on the channeltron was typically at +2500 V. This detector had a higher detection sensitivity with a better signal-to-noise ratio than the copper target with an op-amp. However, the detector assembly was bulky and requires several inches of space perpendicular to the beam path. In our system, it was mounted in the center of a six-way cross, which meant that its location was not easily changeable. Most importantly, the response of the dynode to the mass of the ions was unknown and probably decreases with increasing mass, and the gain of the whole detector also required calibration.

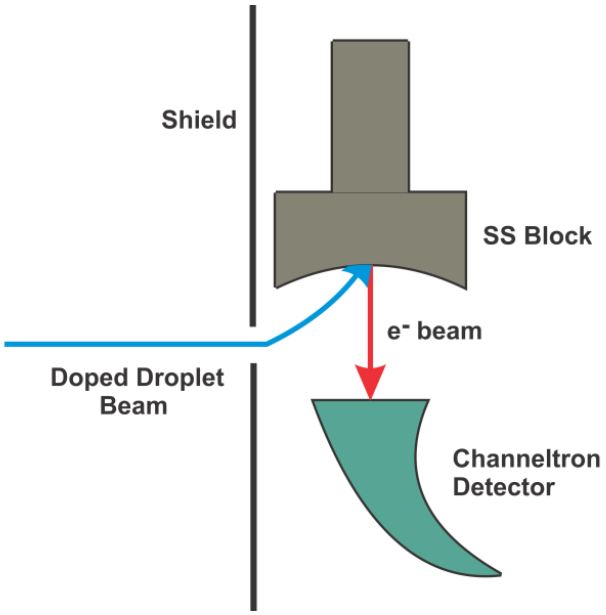

Fig.5.9. Schematic drawing of a Daly-type dynode detector.

5.4 Cesium ion sources

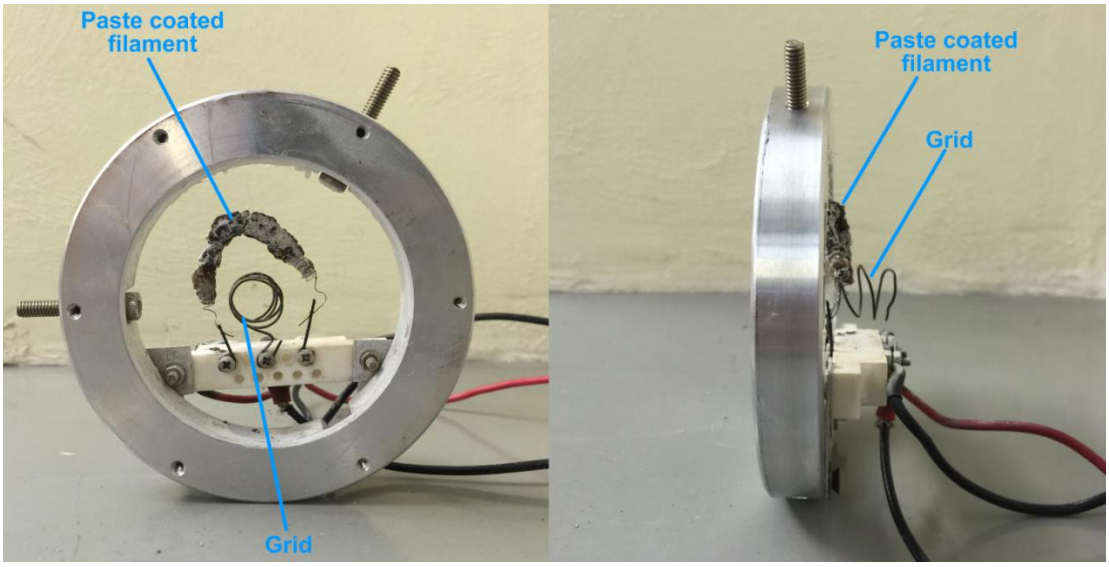

Fig. 5.10. Pictures of the homebuilt cesium ion source.

To generate a continuous supply of cesium ions, we heated a tungsten filament coated with a zeolite paste as describe by Draves *et al*.[3] The homebuilt cesium ion source was shown in Figure 5.10. We started with a commercial zeolite matrix (Sigma-Aldrich Molecular sieves, 13X,

1 Na_2O: 1 Al_2O_3: 2.8 SiO_2: x H_2O) containing both abundant Na and K ions, and enriched the cesium content via an ion exchange reaction. This was achieved by grinding the zeolite into powder, rinsing the powder with a saturated solution of CsCl (18.6g/ml), and stirring the wet zeolite overnight. A tungsten filament of 0.25 mm dia. was shaped into a coil of 3.0 cm in length and 2.0 mm in diameter, bent into a semicircle, and mounted on a ceramic bar by tightening two screws. The filament was then wiped thoroughly with methanol before the wet paste was applied. Once the

filament was coated completely, the ion source was to sit in the air for one day to drive away any moisture before being placed in the doping chamber. To eliminate impurities and to improve the intensity and consistency of the ion source, a current of 2 A was passed through the filament to heat it into a bright glow in a vacuum chamber. After baking for 8 - 10 hours, the filament with paste was ready for use. Under normal working conditions, a current of ~2.8 A was applied to the filament, but slight variations were possible because of the different length of the filament wire and the different amount of paste on the filament.

The ion collector was another copper grid of 2 cm long and 1 cm in diameter, which was roughly concentric with the semi-circular filament coil (Fig. 5.10). It was wired according to Fig. 5.7, hence the absolute number of ions hitting the grid can be measured. When the grid was biased negative relative to the filament, cesium ions would be extracted into and oscillate through the space inside the grid at a constant and defined kinetic energy. In Fig. 6.1, a simulation trace of a cesium ion in the vicinity of the filament and grid is shown

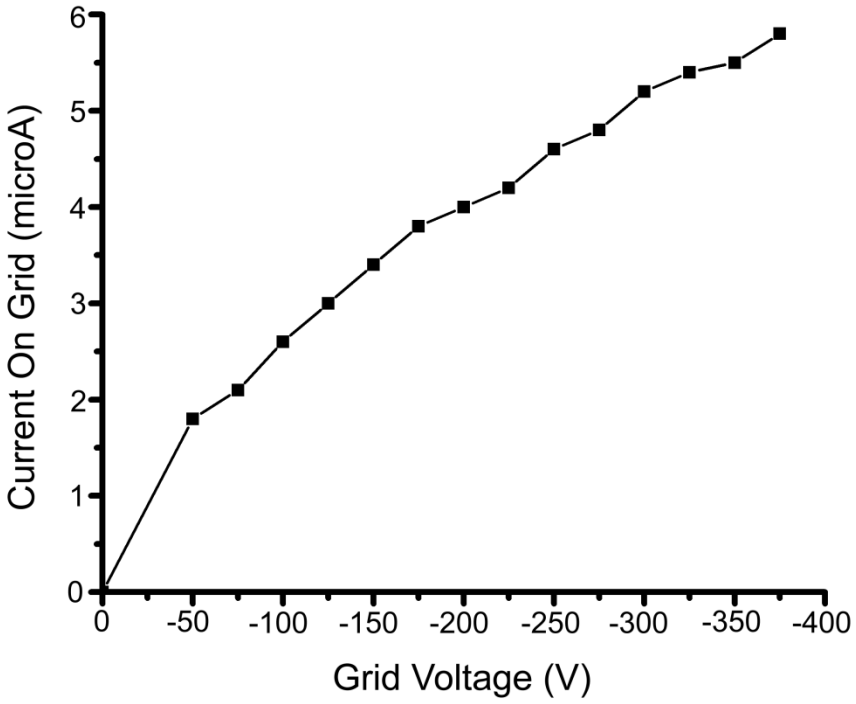

Fig. 5.11. Current on grid increased with grid voltage.

At a fixed heating condition for the filament, the total cesium ion emission current should be constant. When the grid was grounded, cesium ions were emitted in all directions. With increased grid voltage, more ions were attracted to the grid and we could detect an increased current on the grid. Fig. 5.11 shows the variation of the detected grid current as a function of the grid bias. Limited by the range of the power supply of -400 V, the measurement did not reach saturation – when all the emitted ions were attracted to the grid. However, based on Fig. 5.11, the emission current should be above 6 μA.

5.5 Reference

1. Slipchenko, M. N.; Kuma, S.; Momose, T.; Vilesov, A. F., Intense pulsed helium droplet beams. *Rev. Sci. Instrum.* **2002,** *73*, 3600-3605.
2. Yang, S.; Brereton, S. M.; Ellis, A. M., Controlled growth of helium nanodroplets from a pulsed source. *Rev. Sci. Instrum.* **2005,** *76*, 104102.
3. Draves, J. A.; Luthey-Schulten, Z.; Liu, W.-L.; Lisy, J. M., Gas-phase methanol solvation of Cs+ : Vibrational spectroscopy and Monte Carlo simulation. *J. Chem. Phys.* **1990,** *93*, 4589.

Chapter 6 Effect of Kinetic Energy on the Doping Efficiency of Cesium Cations into Superfluid Helium Droplets

Lei Chen, Jie Zhang, William M. Freund, and Wei Kong*

Department of Chemistry, Oregon State University, Corvallis, OR 97331

Manuscript for submission to the Journal of Chemical Physics, June 22, 2015

*Corresponding author, 541-737-6714, wei.kong@oregonstate.edu

Abstract

We present an experimental investigation of the effect of kinetic energy on the ion doping efficiency of superfluid helium droplets using cesium cations from a thermionic emission source. The kinetic energy of Cs^+ is controlled by the bias voltage of a collection grid collinearly arranged with the droplet beam. Efficient doping from ions with kinetic energies from 20 eV up to 480 V has been observed in different sized helium droplets. The relative ion doping efficiency is determined by both the kinetic energy of the ions and the average size of the droplet beam. At a fixed source temperature, the number of doped droplets increases with increasing grid voltage, while the relative ion doping efficiency decreases. This result implies that not all ions are captured upon encountering with a sufficiently large droplet, a deviation from the near unity doping efficiency for closed shell neutral molecules. We propose that this drop in ion doping efficiency with kinetic energy is related to the limited deceleration rate inside a helium droplet. When the source temperature changes from 14 K to 17 K, the relative ion doping efficiency decreases rapidly, perhaps due to the lack of viable sized droplets. The size distribution of the Cs^+-doped droplet beam can be measured by deflection and by energy filtering. The observed doped droplet size is about 5×10^6 helium atoms when the source temperature is between 14 K and 17 K.

6.1 Introduction

Doping of superfluid helium droplets offers the advantage of investigating isolated particles under cryogenic temperatures in a non-perturbing medium.[1-6] The technology of doping neutral particles has evolved from volatile molecules to thermally labile biomolecules to radicals and clusters.[7-13] The superfluid environment and the unique properties of the quantum fluid have also inspired generation and investigation of esoteric species.[14-24] Even the possibility of producing nanomaterials with controlled properties in superfluid helium droplets has been explored.[15, 17, 21, 25] For example, in the mass spectrum of metal vapor-doped droplets, silver clusters are observed to contain up to 100 Ag atoms,[15, 17] and magnesium clusters can even reach several thousands of atoms.[16] The photoabsorption of Ag clusters in helium droplets shows that the transition from compact to multicenter aggregates increases with the growth of droplet sizes.[21] In the work of Gomez *et al*,[22] silver clusters desolvated from helium droplets have been captured and imaged via electron microscopy. The authors have observed evidence of single and multiple vortices longer than 300 nm. To explore the dynamic properties of individual droplets, recently, Gomez *et al*[23] have further recorded Bragg diffractions of neat and xenon-doped droplets via x-ray scattering from a free-electron laser.

Efforts have also been devoted in doping cations in helium droplets, partly motivated by studies of helium snowballs.[26-36] Direct ionization of helium atoms or embedded neutral molecules has proven the most straightforward approach.[16, 28-29, 32, 36-38] Schöbel *et al*[37] have reported the mass spectrometry of pure helium droplets and

droplets doped with krypton using electron impact ionization. Döppner *et al*[32] have ionized metal clusters embedded in helium droplets using a femtosecond laser and studied the size distribution of metal ion-helium clusters. For $Mg^{+}He_N$, the first solvation shell closes at N = 19 - 20, and for $Ag^{+}He_N$ N = 10 and 12. Using synchrotron radiation, Kim at al[28] have reported an indirect mechanism of dopant ionization via excitation transfer or charge transfer from the surrounding helium atoms. Subsequently, the same group[29] has reported efficient cooling of fragments from photoionization and fragmentation of SF_6 in helium droplets. Following the lead of Ghazarian, Eloranta, and Apkarian in using laser ablation in the presence of cold helium vapor for injection of molecular species into a liquid helium beam,[39] Claas, Mende, and Stienkemeier have reported doping of alkali and alkaline metal ions from the plasma produced by a focused laser beam on a rotating and translating metal rod.[40] Since the ablation spot is close to the expansion and nucleation region of the droplet beam, the authors have attributed the unusually large size of the doped droplets and the temperature dependence of the droplet size to the nucleation effect of the ablated atomic and ionic species. Direct doping of cations in helium droplets has been reported by Bierau *et al*.[41] using an electrospray ionization (ESI) source. Biological ions stored in a quadrupole ion trap have been doped in helium droplets when a pulsed droplet beam traverses the trap. Only heavy doped droplets with high kinetic energies can escape the trap to hit the detector. In the work of Falconer *et al*,[11] sodium cations from a thermionic emission source have been introduced into the path of a helium droplet beam via an electric field, and $[Na(H_2O)_n]^{+}$ cluster-doped helium droplets have been confirmed.

Most results of ion-doped droplets have focused on the size distribution of the ion-doped droplet beam. The deflection and acceleration experiments of Bierau *et al*[41] have demonstrated that doped droplets containing the protein cytochrome C (CytC) have on average 10^{12} helium atoms per ion, and when the charge of CytC shifts from +9 to +17, the droplet size slightly increases. In the work of Falconer *et al*,[11] although no direct measurement of doped droplets has been observed, based on simulation and mass spectrometry, the authors have estimated a mean size of 3×10^5 helium atoms per droplet.

An open question related to doping of charged species in superfluid helium droplets is the effect of kinetic energy on the ion doping efficiency. Superfluid helium droplets have been considered scavengers for neutral closed shell species with a pickup efficiency of near unity.[42] In many experiments involving doping of neutral molecules, the thermal energy of the gaseous molecules is below 0.1 eV with a velocity less than 500 m/s. Ions on the other hand typically have kinetic energies over 10 eV with velocities over 5000 m/s, and many head-on collisions with helium atoms inside a droplet are probably necessary to decelerate and stall the fast moving ions. In this work, we present our investigation of the effect of kinetic energy on the ion doping efficiency of superfluid helium droplets. We use a thermionic source of cesium cations Cs^+ as dopant because of its high ion abundance and its ease in operation; both factors contribute to the reproducibility and high signal-to-noise (S/N) ratios of the experimental result. We introduce a relative ion doping efficiency to reveal the anti-correlation between the kinetic energy of bare ions and the number of

doped droplets, and we offer a tentative model for the observed effect. Within the temperature range of 14 K to 17 K (limited by our experimental apparatus), we have also discovered that the final size distribution of the doped droplets is independent of the source temperature, although the ion doping efficiency decreases with increasing source temperature.

6.2 Experimental setup

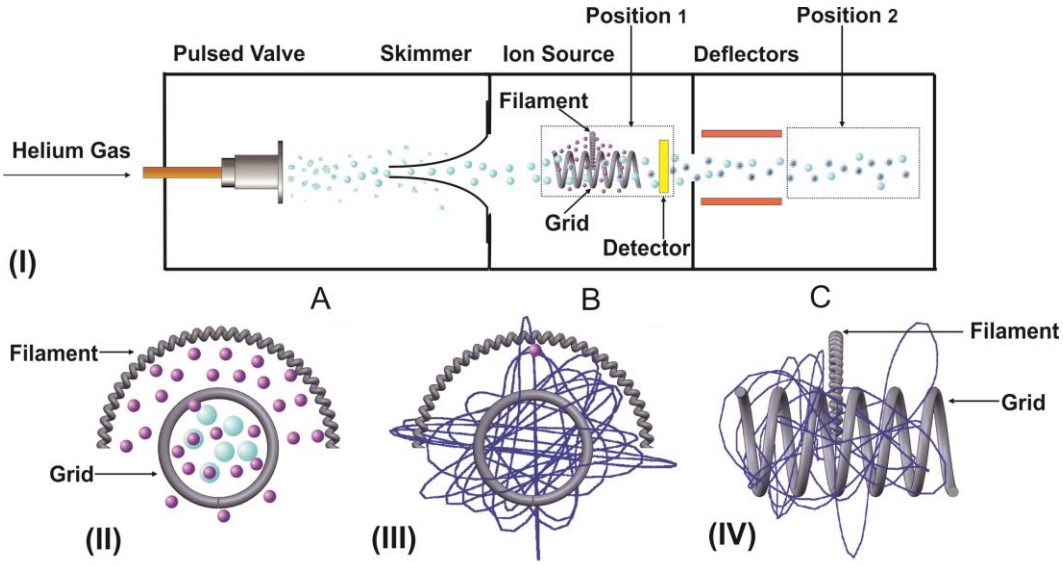

Fig.6.1. Experimental setup. In part (I), (A) Droplet source chamber: superfluid helium droplets were generated by a pulsed valve and collimated by a skimmer. (B) Doping Region: Cesium ions were produced from a thermionic emission source and were accumulated in the coil shaped grid to overlap with the droplet beam for doping. (C) Analysis region: a metal target was directly in-line with the droplet beam for detection of only charged (doped) droplets. We placed the ion source and the detector in two different positions (Position 1 and Position 2) to determine the velocity of the pure droplet beam. Light blue dots/drops represent pure helium droplets, the dark purple dots represent cesium cation, and dark centered light blue drops represent doped droplets. Part (II) shows the end view of the ion source/doping region, part (III) shows a simulated trajectory of one ion emitted from the top of the filament traversing the doping region multiple times, and part (IV) is the side view of the same trajectory. The starting position of the ion is noted by a dark purple dot in part (III).

The experimental setup is shown in Fig.6.1. Superfluid helium droplets were generated in the source chamber labeled A, and the droplet beam passed through the ion source region and arrived ultimately at a copper target detector. The droplet

source chamber and the chamber for regions B and C were separated by a skimmer, while the two regions B and C were separated by a copper plate with a 1 cm central hole. The droplet source chamber was pumped by two diffusion pumps (Varian VHS-6 and Edwards Diffstack 160 mm) and was usually at $4 \times 10^{-7}/4 \times 10^{-6}$ Torr when the pulsed valve was off/on. The ion source and analysis chamber (regions B and C) were pumped by a turbo molecular pump (Varian V551) and was typically at $7 \times 10^{-7}/4 \times 10^{-6}$ Torr when the pulsed valve was off/on.

We used a pulsed valve (Parker Hannifin Corp, Series 99) to produce superfluid helium droplets by supersonic expansion of ultrapure (99.999%) helium at about 30 - 50 bar into vacuum. The pulsed valve had a homemade nozzle with a diameter of 500 μm. It operated at 10 Hz with a duration of 130 - 145 μs powered by its own driver (Parker Hannifin Corp, IOTA One). The nozzle was cooled by a closed-cycle helium cryocooler (APF cryogenics, HC-4 MK1), and it could be set at any temperature above 13 K. The helium droplet beam was further collimated by a 5 cm long skimmer of 2 mm in diameter (Beam Dynamics) located 12 cm downstream from the nozzle.

Cesium ions were produced by heating a tungsten filament coated with a zeolite paste as detailed by Draves *et* al.[43] The filament was a tungsten coil of 3.0 cm in length and 2.0 mm in diameter, and the wire itself was 0.25 mm in diameter. The coil was shaped into a semicircle surrounding the droplet beam, and its side view is shown in Fig.6.1(I) and the end view in Fig.6.1(II). For illustration, the light blue dots/drops represent pure helium droplets, the dark purple dots represent cesium

cation, and dark centered light blue drops represent doped droplets. Under normal working conditions, a current of about 2.8 A was passed through the filament, and the total emission current was 2.8 μA. Concentric with the filament on the end view (Fig.6.1(II)) is the ion collector, a copper grid (referred to as the grid in the following) of 2 cm long and 1 cm in diameter, and its side view is shown in Fig.6.1(I). The grid was biased negative relative to the filament, thereby facilitating the oscillation of cesium ions through the space inside the grid at a constant and defined kinetic energy. In Fig.6.1(III), a simulated trajectory of one ion emitted from the top of the filament (the initial position of the emitted ion is indicated by a dark purple dot) is shown viewed from the end, and in Fig.6.1(IV), the same trajectory is shown from the side. The grid was connected to an operational amplifier and a megaOhm resistor, which converted the ion current into a voltage signal. We could treat this current to be representative of the total number of available ions for doping, although the true number of ions inside the grid was unknown. Both the grid and the filament could be independently biased, and the current on the grid increased with the bias voltage on the grid. Typically when the grid was at -100 V and the filament was at 10 V, the voltage signal was about 1.5 V, corresponding to an ion count of 10^{13} ions/second on the grid.

The copper target detector measuring 4 mm × 10 mm was not biased intentionally and was directly attached to an operational amplifier and a gigaOhm resistor, converting a single charge into a voltage pulse. The copper target was only sensitive to charged species; hence neutral undoped droplets generated no detectable

signal. The ion source and the detector could be placed in two different positions as labeled “Position 1” and “Position 2” in the figure, so the group velocity of the droplet beam could be determined by monitoring the different arrival times of the doped droplets on the target. In the analysis region C, a set of electrodes could be used to deflect the charged particles away from the detector, with the intention of resolving the kinetic energy of the charged species. For this purpose, the copper target was placed at Position 2 while the ion source remained at Position 1.

6.3 Experimental results

6.3.1 Doping of cesium ions into helium droplets

Doping of cesium ions into helium droplets was confirmed by varying the experimental conditions. When only the filament and the grid were in operational conditions, no ions could be detected on the copper target. When the pulsed valve was turned on but was kept at room temperature, there were still no ions arriving at the detector. Only when we cooled down the nozzle below 20 K could there be any observable ion signal. The ion signal disappeared when the ion source was turned off.

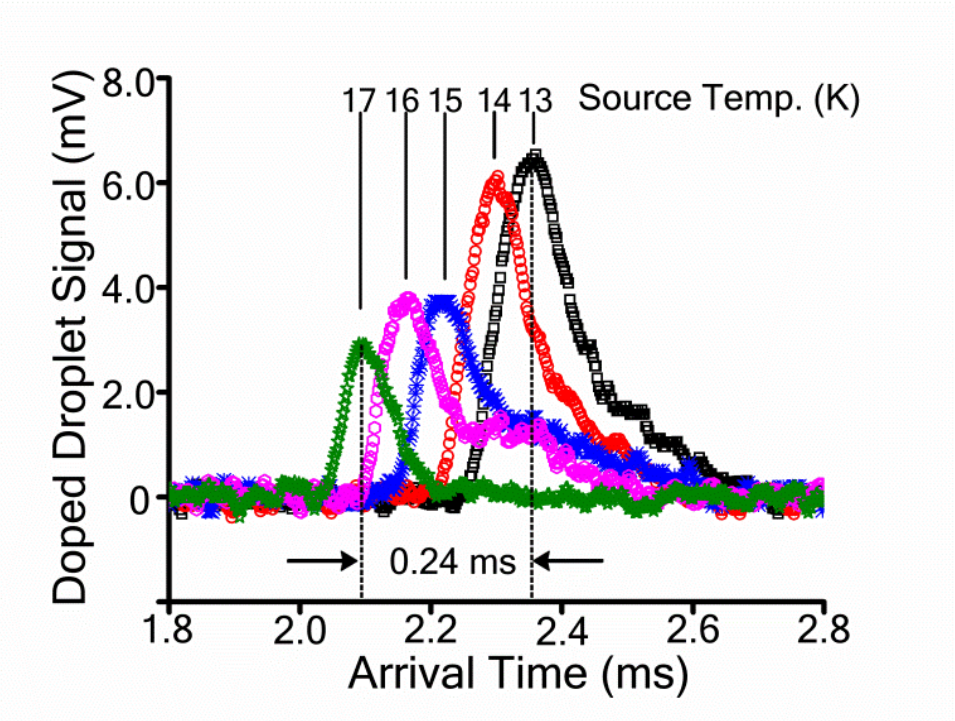

Fig.6.2. Arrival times of doped helium droplets with varying nozzle temperatures, from 13.2 K to 17.0 K. With increasing nozzle temperature, the ion signal decreases and shifts to an earlier time. Shoulder peaks are visible under all different nozzle temperatures; they were results of the rebound of the pulsed valve. The ion detector was in position 2 during this experiment.

Figure 6.2 shows the time profile of the detected doped droplet signal under different nozzle temperatures recorded at Position 2 in Fig.6.1. Both the magnitude and timing of the ion signal depend on the temperature of the droplet source. From 13.2 K to 17.0 K, the arrival time of the ion signal shifts by 0.24 ms and the total signal decreases by over 50%.

Without any acceleration field along the flight path, the arrival time of the doped droplets was determined by the group velocity of the neutral droplet beam. Although the response time of our gigaOhm resister was limited, with sufficient

distance between the two measuring points (Positions 1 and 2 in Fig.6.1), we could still use the onset of the ion signal to measure the velocity of the droplet beam. In Fig.6.1, Position 1 was 37 cm away from the pulsed valve, and Position 2 was 74 cm away from the pulsed valve. From the difference in the arrival time between the two positions, we determined that the droplet speed was 371 m/s at 13.2 K and 422 m/s at 17.0 K. In comparison, the theoretical speed of an ideal helium gas from a supersonic expansion should be 375 m/s at 13.2 K and 419 m/s at 17.0 K, in general agreement with our measurements.

6.3.2 Effects of fringe fields and space charges

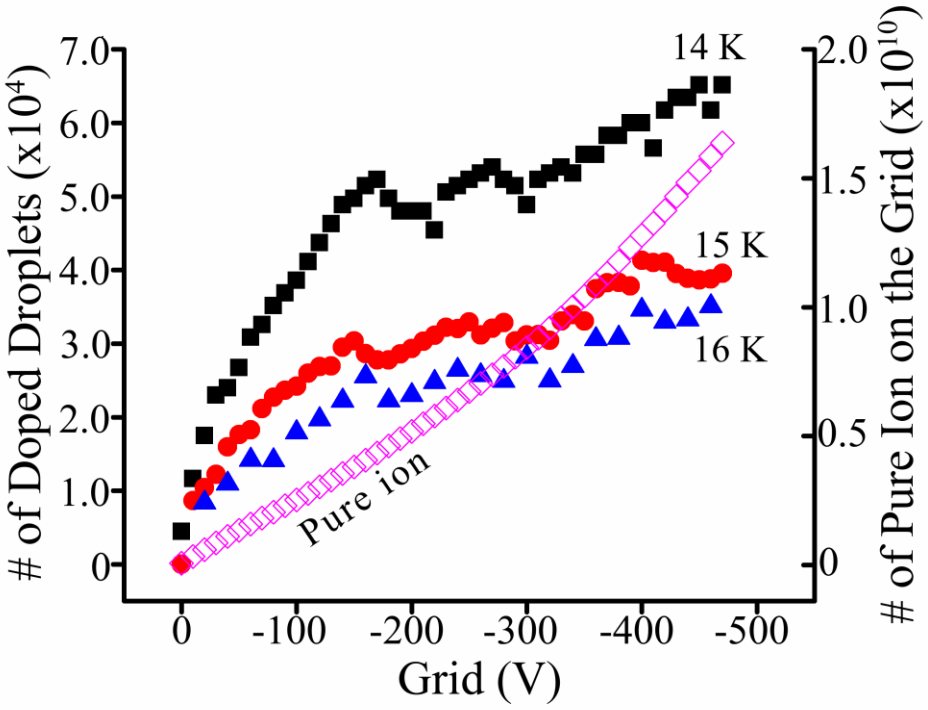

Fig.6.3. Dependence of both the number of doped droplets (left axis, filled symbols) and the number of ions hitting the grid (right axis, open squares) on the grid voltage at different source temperatures.

Fig.6.3 shows the total number of ion-doped droplets and the total number of ions hitting the grid at different grid voltages. In calculating the number of ions hitting the grid, we took the duty cycle of the droplet beam into consideration, so the DC ion current on the gird was chopped to 140 μs to match the duration of the pure droplet beam. We calculated the total number of ion-doped droplets by changing the voltage signal from Fig.6.2 to a current through the gigaOhm resister and then integrating the peak area for the number of charges. While the number of bare ions hitting the grid grows with the grid voltage following a power law-like behavior, the number of doped droplets also increases but with a clear "bend" – an abrupt change in the rate of increase – when the grid voltage reaches -150 V. Fig.6.3 also shows that with increasing source temperature, the number of doped droplets also drops. At 16 K when the grid voltage is -100 V, the number of doped droplets is less than half of that at 14 K.

The bias on the grid in the ion source affected not only the number and movement of bare ions, but also those of doped droplets, both as a trapping field and in terms of fringe fields at the exit of the grid downstream from the doping region. The group velocity of the pure droplet beam was 388 m/s at a source temperature of 14 K, and at a grid voltage of -180 V, a doped droplet had to consist of at least 5.7×10^4 helium atoms to have enough kinetic energy to escape from the negative trapping field of the grid. Downstream, some escaped doped droplets would be affected by the fringe field of the grid thereby veering too far off-axis along the path to the target. Using Lorentz-EM (Integrated Engineering Software, Winnipeg, Manitoba, Canada),

a software package specially designed for magnetic analysis and for analysis of charged particle trajectories in the presence of electric and magnetic fields, we simulated this fringe effect and obtained a cutoff size of ~10^5 helium atoms per droplet, below which a doped droplet would fail to arrive at the target. Experimentally, the actual cutoff size was probably even bigger, at ~10^6 atoms/droplet, because of unaccounted loss mechanisms in the simulation, such as the non-ideal vacuum level and stray fields due to other electrodes or even turbomolecular pumps. As the grid voltage increases, the cutoff size also increases. In the meantime, from Fig.6.3, the number of bare ions traveling into the grid seems to also increase. The increase in the number of doped droplets, however, slows down at the "bend" when the grid voltage is more than -150 V.

One possible explanation of the "bend", i.e. the change in slope for the doped droplets at -150 V, is the space charge limit. In Fig.6.3, the number of ions hitting the grid is on the order of 10^{10}, and given the fact that the volume inside the grid is a few cubic centimeters, this value is way above the space charge limit of $10^7/cm^3$.[44] The actual number of ions inside the grid should then be much smaller, at most on the order of 10^7. Once the space charge limit is reached, further increase in the negative bias of the grid has the effect of expanding the retention region, determined by the negative potential of the grid, further out to the vacuum chamber (fixed at ground potential). The ultimate effect is therefore an increase in the volume of the "ion trap", determined by the dimension of the grid and its extended field upstream and downstream along the droplet beam. However, this effect should be rather limited given the available physical space for expansion, so the increase in the number of

bare ions for doping with increasingly more negative bias on the grid would be at a much lower rate after the system reaches the space charge limit. On the other hand, the cutoff size will increase with increasing bias, preventing small doped droplets from reaching the detector. The change in the number of doped droplets is then determined by the balanced effect of the cutoff size and the doping volume. The "bend" in Fig.6.3 could be the point where the space charge limit is reached, and the slow rise after -150 V is the predominant effect of the increasing doping volume with increasing grid bias.

If we assume that the total number of bare ions in the doping region is limited by the space charge at a grid bias of -150 V to 10^7 ions, the absolute ion doping efficiency, defined as the ratio of the number of ion-doped droplets and the number of total ions available for doping, should be on the order of 5‰ at a source temperature of 14 K when the number of doped droplets is 5×10^4. On the other hand, if the "bend" is not representative of the space charge limit, then the actual ion doping efficiency should be higher since the number of ions inside the doping region is smaller.

6.3.3 Droplet size distribution

6.3.3.1Deflector test

To determine the size distribution of the doped droplets, we first used a set of deflectors to steer the doped droplet beam away from the detector, similar to the method of Bierau *et al.*[41] As the voltage on the deflector increases, small doped droplets are driven away from the detector, thus a correlation between the detected doped droplets and a lower size limit can be established at each deflection voltage. In

Fig.6.1, the deflector electrodes were 40 mm long and were separated by 40 mm. These electrodes were positioned 38 cm downstream from the ion source, and the detector (4 mm along the deflection direction) was located 60 mm downstream from the deflectors. These geometric parameters and the voltage on the deflector determine a lower size limit for the detected doped droplets. During the experiment, one of the deflector electrodes was grounded, while the other was biased from -2200 V to 2200 V. The left of Fig.6.4 shows the number of doped droplets arriving at the target under different deflection voltages (bottom axis), and the top axis shows the corresponding lower size limit for the detected droplets. At -300 V, the signal drops to 54% of that without the deflection voltage. The corresponding lower size limit for the doped droplets arriving at the detector is 4.3×10^6 helium/droplet.

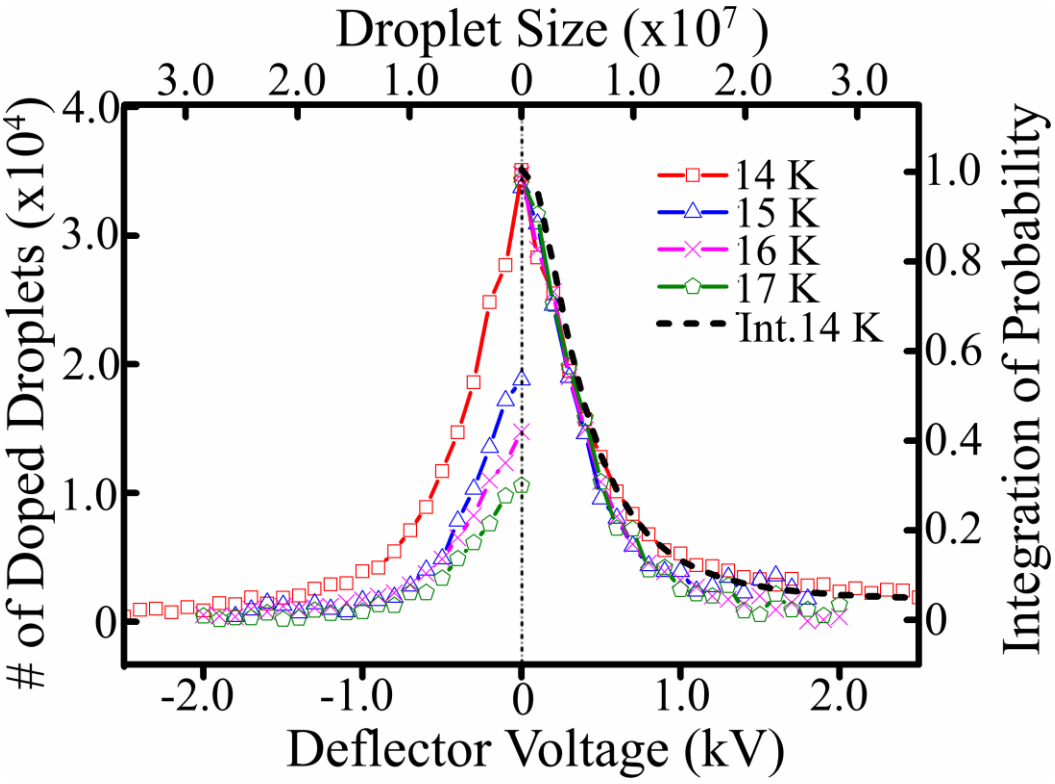

Fig.6.4. Deflection of doped droplets. Left panel: absolute number of doped droplets arriving at the target under different deflection voltages. Right panel: normalized ion signal by setting the maximum ion intensity under a fixed nozzle temperature to unity. The black dashed line is the integrated result from a log-normal distribution of pure droplets at 14 K using parameters obtained from Fig.6.5.

The source temperature of the pulsed valve determines the average size of the droplet beam, which in turn affects the doping efficiency. After doping, we anticipate that perhaps the size distribution of the resulting doped droplet should also reflect this difference. To emphasize the size distribution at different source temperatures, on the right of Fig.6.4, we plotted the normalized ion signal by setting the maximum ion intensity under a fixed nozzle temperature to unity. Surprisingly, all traces overlap. We therefore conclude that within the temperature range of 14 and 17 K, the doped droplets had a similar size distribution, independent of the initial nozzle temperature.

According to reference [45], the size distribution from a continuous superfluid helium droplet source can be modeled using a log-normal function when the nozzle temperature is higher than 14 K,

$$P_N(N) = (N\sigma\sqrt{2\pi})^{-1}\exp[\frac{-(\ln N-\mu)^2}{2\sigma^2}], \quad (6.1)$$

where $P_N(N)$ is the probability of a droplet consisting of N helium atoms, and the parameters σ and μ are the standard deviation and the mean of lnN. The size distribution of the doped droplets could be obtained by differentiating the number of doped droplets arriving at the detector by the corresponding minimum droplet size (the top axis of Fig.6.4). In Fig.6.5, black squares represent the resulting differentiation from the experimental data at 14 K (Fig.6.4), and the continuous trace is a log-normal fit to the experimental data. The mean size from this fitting was 7×10^6 helium/droplet. Similar treatments of data from other source temperatures also resulted in similar size distributions and mean sizes. The resulting values of σ and μ were about 0.77 and 15.45. These values were then used to calculate the number of doped droplets at each deflection voltage by integrating Eq.6.1 from the lower size limit determined from the experimental geometry to infinity, and the result is shown by the dashed line of Fig.6.4 labeled as "Int. 14 K". This trace overlaps with our experimental data. Although it is known that in the range of the current source temperatures (≥ 14 K), neutral helium droplets follow a log-normal function, apparently the doping process did not alter this size distribution substantially. However, the consistency in size and distribution within our temperature range also implies that the size distribution of the doped droplets was insensitive to the initial

size distribution of the neutral droplet beam. This could be due to the small limited temperature range of our cryostat, and the fact that we were only fitting the tail part of a log-normal distribution. In the work of Filsinger *et al*,[46] a similar conclusion was obtained within the temperature range of 14 K to 18 K.

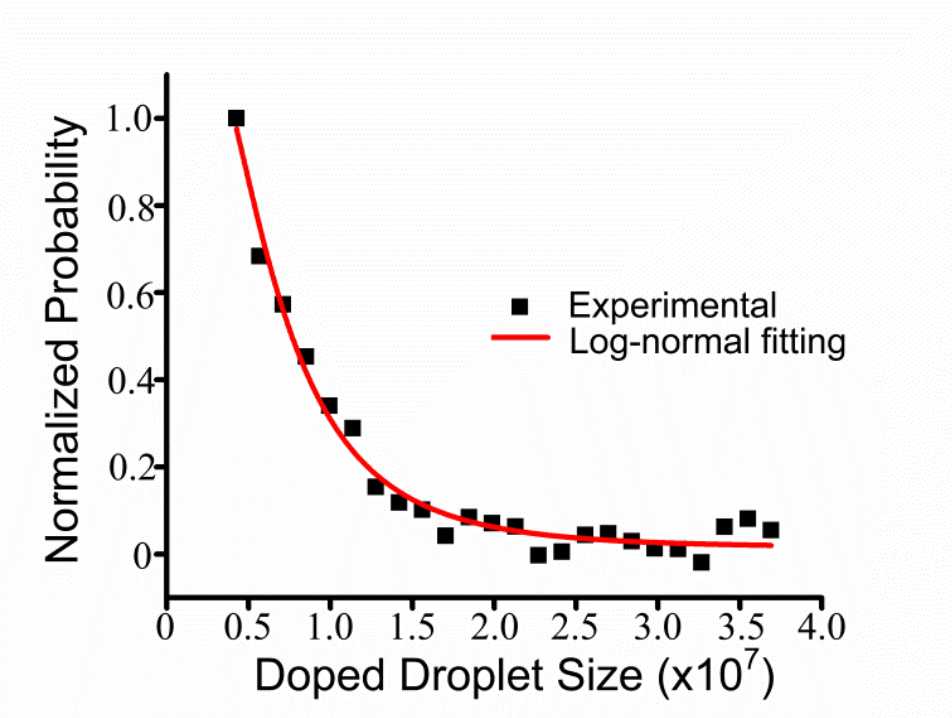

Fig.6.5. Size distribution of doped droplets at a source temperature of 14 K.

6.3.3.2 Energy filter experiment

Another possible approach to determine the size distribution of doped droplets is to introduce an energy filter using a biased mesh. If the doped droplets move at a constant group velocity, different sizes will have different kinetic energies, and only ions with sufficient kinetic energies can pass through the biased retardation electrode. For this purpose, we replaced the deflector electrodes with a planar electrode that had a circular hole of 38 mm in diameter. The hole was covered with a fine mesh of 50 ×

50 mesh plain and 0.025 mm in wire diameter. To further shield the copper target from the field of the retardation electrode, another coarse mesh of 16 × 16 mesh plain and 0.25 mm in wire diameter was placed 2 mm in front of the copper target. The planar electrode and detector were positioned 142 cm downstream from the ion source.

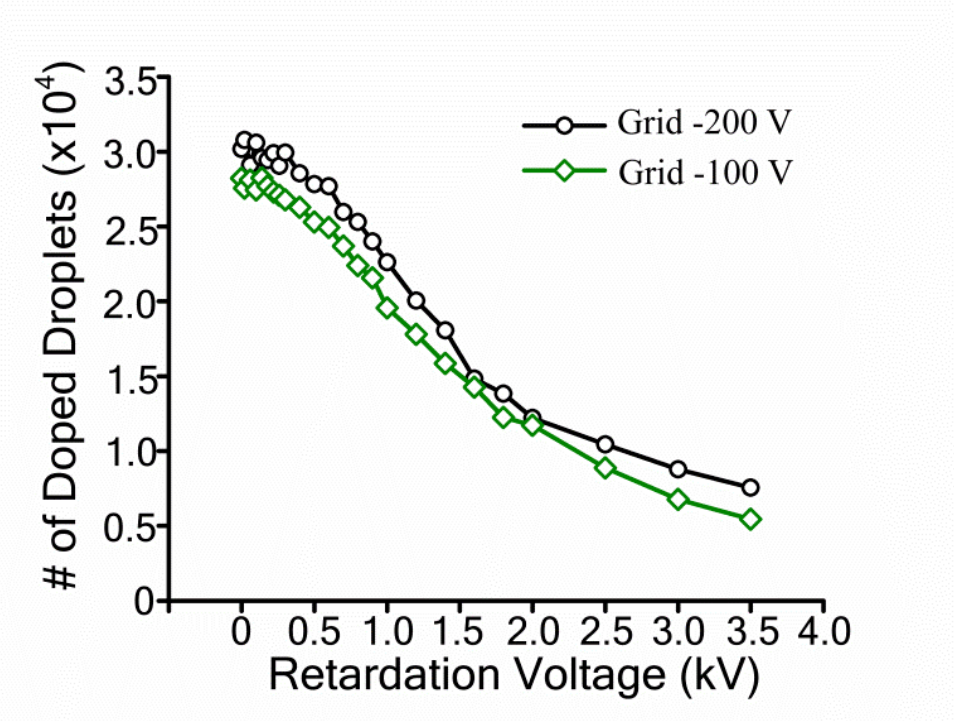

Fig.6.6. Doped droplets passing through a retardation electrode. The trace with open circles was obtained with a grid voltage of -200 V, and the trace with open squares was with a grid voltage of -100 V.

Fig.6.6 shows the variation of the ion signal as a function of the voltage on the retardation electrode when the source temperature was 14.5 K. We performed the experiment under two different voltages on the grid of the ion source, -200 V and -100 V, and in both cases, the trend was the same. The uncertainty of each data point

is about 10%, so the "bend" in the experimental data at a retardation voltage of 1500 V when the grid voltage was -200 V is most likely due to a variation in the experimental condition. From Fig.6.6, even when the retardation voltage reaches 3500 V, there are still more than 28% of the doped droplets reaching the target, and the corresponding droplet size is 1.1×10^6 helium/droplet.

A mean size of doped droplets can be obtained from Fig.6.6. When the grid in the ion source was biased at -200 V, the ion signal dropped to 54% of its peak value at a retardation voltage of 1500 V. Assuming a group velocity of 390 m/s for each droplet, each helium atom in the droplet has a kinetic energy of 3.18 meV, and to obtain a total kinetic energy of 1500 V, the corresponding size of the doped droplet is 4.4×10^5 helium/droplet. Thus we conclude that about 54% of the doped droplets were larger than 4.4×10^5 helium/droplet.

The average size of doped droplets from this retardation experiment was about one tenth of that from the deflector experiment (Fig.6.4). One factor for this discrepancy could be the position of the detector: in this experiment, the detector was placed 68 cm further downstream from the ion source. Continued evaporation due to collisions with ambient molecules in the flight path would result in a decreased droplet size. At a vacuum level of 4×10^{-6} Torr and a source temperature of 14 K, the average radius of a droplet was about 17 nm, and the average collision rate was 3×10^5 /s. If each collision consumed about 42 helium atoms by evaporation, the total loss of helium atoms after a path length of 68 cm was 2.2×10^4. This value was too small to account for the one order of magnitude decrease in droplet size from this

energy filter experiment. Another possibility was the additional collisions between the small doped droplets stopped in the path of the larger droplets at the retardation electrode (the fine mesh). Since this effect was size dependent, particularly detrimental to large sized droplets, it could play a significant role in reducing the average size of the droplet beam from this retardation experiment.

6.4 Discussion

6.4.1 Size distribution of doped droplets

The size distribution of ion-doped droplets has been measured by Bierau *et a1*[41] in 2010. The authors used a pulsed helium droplet beam to catch a protein cytochrome C in different charge states and singly charged protonated phenylalanine (Phe) produced by electrospray ionization. The ions were trapped in a linear hexapole ion trap coaxial with the droplet beam. The authors reported 10^4 ion-doped droplets per pulse with a duration of 200 μs. Using electrostatic deflection, they fitted a log-normal distribution for the resulting doped droplets, with mean sizes 10^{12} helium atoms for CytC +17, and 10^{10} for Phe. These unusually large sizes, compared with those from Slipchenko *et al,*[47] were attributed to the large nozzle diameter of 800 μm of the pulsed valve. Subsequently, the group replaced the pulsed valve with a different model and measured the size distribution of hemin$^+$-doped droplets via an acceleration experiment.[46] The resulting median size of the doped droplet was reported to range from 1.6×10^6 to 8.3×10^4 helium atoms when the source temperature was varied from 6 K to 18 K.

Falconer *et al*[11] employed a different approach to dope cations into superfluid helium droplets, although no direct characterization of the size distribution of the doped droplets was reported. After traversing a pickup chamber filled with sodium cations generated from a thermionic source, a droplet would pick up a Na^+ ion and several neutral H_2O molecules to form a $[Na(H_2O)_n]^+$ cluster inside. The doped droplet was desolvated along the flight path before the bare cation was deflected into a mass spectrometer. Based on the mass distribution of $[Na(H_2O)_n]^+$ and pickup statistics, the authors derived a mean droplet size by fitting the probability curve using a log-normal and linear-exponential distribution function. At 13.2 K, the resulting mean droplet size was about 3×10^5 helium atoms. They also pointed out that based on their simulation; only doped droplets with greater than 10^6 helium atoms would be able to escape the potential well of the grid at -200 V. This cutoff size was one order of magnitude bigger than the mean droplet size, so the explanation was that only the tail of the droplet distribution was being sampled in the experiment.

Using laser vaporization of alkali and alkaline metal rods near a cryogenic nozzle, Claas, Mende, and Stienkemeier have observed ion-doped droplets due to surface plasma formation.[40] However, the authors proposed that the formation mechanism of ion-doped droplets was related more to the seeding of ions as a nucleation center during condensation of helium atoms near the exit of the nozzle than to the migration of ions into already formed droplets. For this reason, the authors observed a variation in droplet size when the source temperature changed from 19.6 K to 23 K. Moreover, the observed size of nearly 5×10^4 atoms/droplet at

a source temperature of 19.6 K was substantially larger than the corresponding theoretical value.

Our droplet size is in general agreement with those from Bierau *et al* and Falconer *et al*.[11, 46] Limited by the capacity of our cryostat, we can only vary the source temperature in the range of 14 K to 17 K, and our resulting doped droplet sizes are similar in all cases, with an average value of 7×10^6 helium atoms. The discrepancy of our value from that of Claas, Mende, and Stienkemeier can be attributed to the different mechanisms of droplet formation.[40] On the other hand, our observation of the decrease of doped droplets with increasing nozzle temperature as shown in Fig.6.3 agrees with that of Claas, Mende, and Stienkemeier. Our design of the ion source is the same as that of Falconer *et al*[11], but the additional grid in the doping region has been observed to triple the doping signal. More importantly, the bias on the grid offers control over the kinetic energy of the incident ions, which allows observation of the effect of kinetic energy on the ion doping efficiency.

6.4.2 Relative ion doping efficiency

To determine the absolute ion doping efficiency, we need to take the ratio of the total number of doped droplets and the total number of ions in the doping region. The absolute number of doped droplets is affected by the temperature of the droplet source and by the grid voltage of the ion source. Without a bias voltage on the grid of the ion source, only thermal ions were present around the region of the filament, and no doping was observable when the source temperature of the droplet beam was above 14 K. As the bias on the grid increased, more ions were pulled into the region

of the droplet for doping, and more doped droplets were observable. However, the number of ions in the doping region was limited by the space charge effect while the measured current on the grid was not.

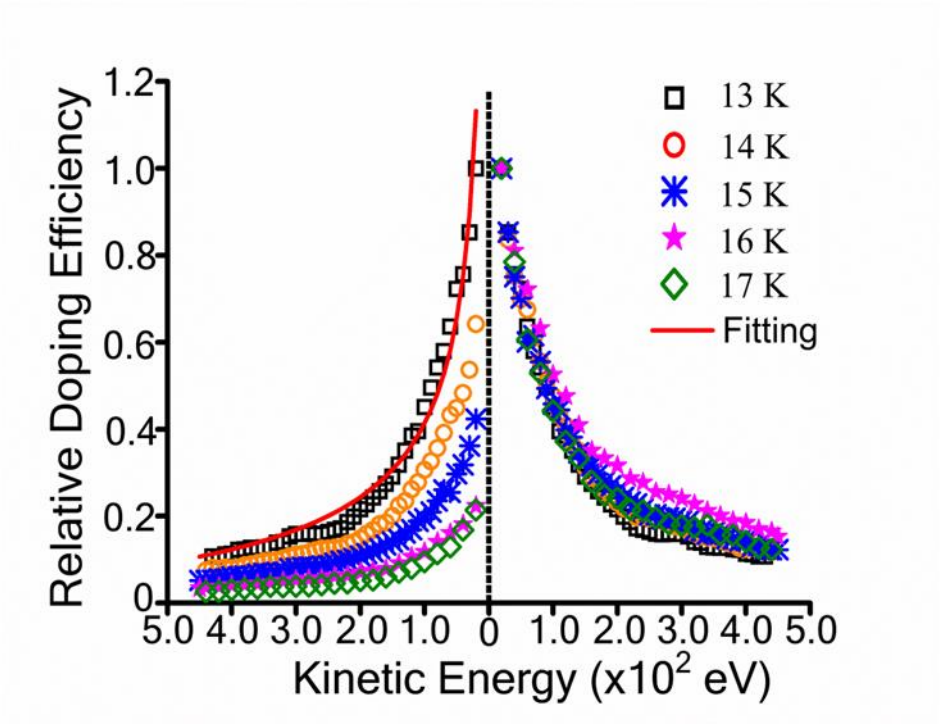

Fig.6.7. Relative ion doping efficiency at different kinetic energies and source temperatures. The left panel is normalized relative to the efficiency at a source temperature of 14 K and a kinetic energy of -20 V, and the right panel is normalized for each source temperature. The solid line on the left panel is a fitting result assuming an inverse relation between the ion doping efficiency and the velocity of the incident ions.

To avoid the above difficulties, we define a relative ion doping efficiency by setting the ratio of doped droplets to the ions on the grid to unity at a kinetic energy

(grid voltage) of -20 V and a source temperature of 14 K. This choice of the kinetic energy corresponds to the lowest bias when doped droplets were observable at all source temperatures between 14 K and 17 K. The left side of Fig. 7 shows the relative ion doping efficiency at different kinetic energies and different source temperatures. At a fixed source temperature, the size distribution of the droplet beam is fixed. With the increase in grid voltage, the absolute number of doped droplets increases, but the relative ion doping efficiency actually decreases. With the increase in source temperature, the droplet distribution shifts to smaller sizes, and the relative ion doping efficiency also decreases. However, if we renormalize the maximum of each trace, as shown on the right side of Fig.6.7, all traces overlap. This result implies that lowering the source temperature uniformly increases the ion doping efficiency in the temperature range of 14 K and 17 K, with no effect on the final size distribution of the doped droplets.

The decrease in the relative ion doping efficiency from 14 K to 17 K can be explained from the following numerical analysis. The binding energy of each helium atom is about 5 cm^{-1} in a droplet. To cool down a single Cs^{+} ion with a kinetic energy of 400 eV, it would take more than 10^{6} helium atoms with a minimum droplet radius of 20 nm. To further escape the potential well of the grid at -400 V, the cooled ion has to retain another10^{6} helium atoms (see discussions of Fig.6.3). The total number of droplets in this size range from a pure droplet beam can be obtained by integrating Eq. 1 in the appropriate size range. If we assume the same gas flux, the theoretical number of droplets at 17 K is about 1.8 times of that at 14 K. This means that if all

droplets larger than 10^6 have the same probability of doping, we should observe 1.8 times more doped droplets at 17 K than at 14 K. Even if we take into consideration the higher gas flux at lower nozzle temperatures, based on the ideal gas law, the ~20% increase in gas flux at 14 K can only reduce the ratio to 1.4. On the other hand, if we change the lower limit of integration from 10^6 to 10^7, the calculation reveals that the total number of droplets for pickup at 17 K is only ¼ of that at 14 K. This value agrees with our experimental observation where the number of doped droplets at 17 K is about 1/3 of that at 14 K. We thus conclude that the actual pickup cross section of a droplet is probably less than half ($10^{1/3}$)of its geometrical cross section, and that the lower relative ion doping efficiency at higher nozzle temperatures is most likely due to the lack of viable sized droplets.

6.4.3. Effect of kinetic energy on ion doping efficiency

The decrease in ion doping efficiency with increasing grid voltage shown in Fig.6.7 demonstrates the adverse effect of kinetic energy of the bare ions for doping. However, the situation is complicated by the fact that bare ions can oscillate in and out of the grid during the doping process. In Fig.6.1, the grid of the ion source attracts the emitted Cs^+ ions into the field free central region where the droplet beam traverses. Without collision with a droplet, a cation can pass through the grid and move towards the chamber wall before turning back. We have simulated this oscillatory motion under different grid voltages using Lorentz-EM, and parts (III) and (IV) in Fig.6.1 show a typical trajectory of one ion emitted from the top of the filament. Within the duration of the droplet beam (140 μs), the number of round trips

of a Cs^+ ion passing through the centre of the grid is 15, a value essentially independent of the grid voltage. Upon further inspection, we realize that higher energy ions are more prone to be affected by fringe fields because of their deeper penetration into the outside region of the grid. Even though they have a higher frequency of oscillation, their stable oscillatory periods are limited. We therefore conclude that the rapid decrease in the relative ion doping efficiency with grid voltage on the left of Fig.6.7 is indeed the adverse effect of kinetic energy.

The decrease in ion doping efficiency with increasing kinetic energy is a clear indication that the capture rate of cations upon collision with a sufficiently large helium droplet can be much lower than unity. If we assume the "bend" in Fig.6.3 at a bias of -150 V is related to the space charge effect, we could ignore the drop in the ion doping efficiency beyond -150 V, because the number of available ions for doping remains more or less constant instead of increasing as shown in Fig.6.3. However, a clear drop between -20 V and -150 V is still evident. When the kinetic energy varies from 20 eV to 100 eV, the velocity of the cesium ions varies from 5000 m/s to 10000 m/s, and the ion doping efficiency drops by 60%.

A detailed modeling of the ion doping efficiency is beyond the scope of our current work. However, we propose a crude qualitative interpretation of the experimental observation. When an approaching ion has a sufficiently high velocity, its trajectory can be considered ballistic, and the charge-induced dipole interaction can be ignored at first. The helium atoms inside the droplet can be considered stationary in a lattice separated by an interatomic distance of 3.5 Å. In a head-on

collision between a cesium ion (atomic mass = 133) and a free helium atom, the Cs^+ loses 6% of its velocity. It thus takes nearly 40 such collisions to reduce the velocity of a Cs^+ from 5000 to 500 m/s – a velocity in the range of thermal neutral molecules for doping. If the mean free path of a Cs^+ is 3.5 Å, the overall time of the 40 collisions for speed reduction is about 13 ps and the overall distance travelled by the ion is 14 nm – almost halfway through a droplet of 10^6 atoms. If side-on collisions are included and we average over the whole range of impact parameters, the effect of deceleration is even less effective: each collision results in a loss of energy (instead of velocity) of 6%. We therefore suspect that many fast ions can directly penetrate through the droplet simply because of the slow deceleration of helium atoms inside the droplet. Following this logic, the ion doping efficiency should be inversely proportional to the velocity of the incident ions. The solid line in the left panel of Fig.6.7 shows a fitting of all the data at 14 K using the function:

$$y = \frac{a}{E} + b, \tag{6.2}$$

where y represents the relative ion doping efficiency, E is the kinetic energy of the ions, and a and b are fitting coefficients. The agreement between the fitting and experimental data is quite remarkable considering the simplicity of the model. Given the possibility of reaching the space charge limit when the grid voltage reaches 150 V, the minor discrepancy in the high energy range is surprisingly small.

Doping of closed shell neutral molecules has been considered to follow the Poisson distribution determined by the geometric cross sections of the helium

droplets.[42] However, studies on refractory metal atoms and the open shell oxygen molecules have revealed much lower pick up efficiencies or smaller pickup cross sections of helium droplets.[48-49] Although atoms of refractory metals and alkali and alkaline metals are all open shell, refractory metals are typically heated to much higher temperatures thereby having much higher thermal energies for doping. We suspect that perhaps the high velocity of refractory metal atoms is partially responsible for the lower sticking probability with helium droplets. In several photofragmentation studies of doped droplets, the inability of the helium droplet in trapping the newly formed energetic fragments has also been documented and simulated using a ballistic model.[29, 50-51] Effect of the kinetic energy on the trapping efficiency has also been explored based on the same principle as our current work with ions. Different from our case of ion doping, on the other hand, neutral molecules have a much weaker interaction with the helium environment. It is therefore surprising that even with the strong ion-neutral interaction, the ballistic model is still qualitatively acceptable, under the current experimental conditions.

Our proposal of a fast ion directly passing through a droplet upon collision is unrelated to the superfluidity of the droplet and unrelated to the ion-neutral attraction inside the droplet. This crude model is therefore only applicable to fast ions; at some point along the deceleration path, the intermolecular interactions will become too important to ignore. More importantly, our simple model only includes head-on collisions, while a more complete model with varying impact parameters would predict an inverse relation with the energy of the cesium ions instead of the velocity

as implied in Eq.6.2. However, fitting using an inverse relation with energy was statistically unacceptable. Our current investigation is limited to kinetic energies above 20 eV due to practical issues with the thermionic source and the temperature range of our cryostat. In an ongoing experiment, we have used an electrospray ionization source to extend the investigation to essentially zero kinetic energies, and the results will be reported in the future. Unlike the doping process of neutral species, with special care in the experimental design, the doping process of ions has advantages in controlling the kinetic energy and in measuring the absolute number of ions and ion-doped droplets. Hence studies of ion doping are of a particular value in revealing the detailed physics inside superfluid helium droplets.

6.5 Conclusions

We have characterized the cation doping process into superfluid helium droplets using cesium cations from a thermionic emission source. By performing two different types of measurements including deflection and energy filtering, the size distribution of Cs^+-doped droplet beam was measured. Our experimental data could be fitted by a log-normal distribution, with a mean size of 5×10^6 helium atoms, more or less independent of the source temperature between 14 K and 17 K. At a fixed source temperature, we observed increased number of doped droplets with increasing grid voltage, but the rate of increase had a sudden drop at a grid voltage of -150 V, perhaps due to the space charge effect. The absolute ion doping efficiency was difficult to measure, but it should be on the order of 5‰ based on the space charge limit in the doping region and the number of doped droplets. When the source

temperature was changed from 14 K to 17 K, a rapid decrease in the relative ion doping efficiency was observed, and the reason was attributed to the lack of viable sized droplets in the droplet beam. The relative ion doping efficiency decreased with increasing kinetic energies of the bare ions, and the decrease was inversely proportional to the velocity of the incident ions. We suggest that for fast moving ions, the ion doping efficiency was far from unity, and many ions simply penetrated through the droplet without being captured due to insufficient deceleration inside the droplet.

Acknowledgement

This work is supported by the National Institute of General Medical Sciences (1RC1GM092054-01 and 1R01GM101392-01A1) from the National Institutes of Health. The content is solely the responsibility of the authors and does not necessarily represent the official views of the National Institutes of Health. Additional support from the Murdock Charitable Trust, the Oregon Nanoscience and Microtechnologies Institute, and the Environmental Health Science Center at Oregon State University funded by the National Institute of Environmental Health Sciences (ES000240) are also deeply appreciated. We also thank Dr. Joe Beckman for his unwavering support and Dr. Joseph Nibler for his generous donation of the cryostat and the vacuum chamber.

6.6 References

1. Toennies, J. P.; Vilesov, A. F.; Whaley, K. B., Superfluid helium droplets: An ultracold nanolaboratory. *Phys. Today* **2001,** *54*, 31-37.
2. Higgins, J. P.; Reho, J.; Stienkemeier, F.; Ernst, W. E.; Lehmann, K. K.; Scoles, G., Spectroscopy in, on, and off a Beam of Superfluid Helium Nanodroplets. In *Atomic and Molecular Beams*, Campargue, R., Ed. Springer Berlin, Heidelberg: 2001; pp 723-754.
3. Toennies, J. P., The fascinating quantum characteristics of helium and their use. *Phys. J.* **2002,** *1*, 49-55.
4. Toennies, J. P.; Vilesov, A. F., Matrix techniques: Superfluid helium droplets: A uniquely cold nanomatrix for molecules and molecular complexes. *Angew. Chem., Int. Ed.* **2004,** *43*, 2622-2648.
5. Slenczka, A.; Toennies, J. P., Chemical dynamics inside superfluid helium nanodroplets at 0.37 K. In *Low Temperatures and Cold Molecules*, Smith, I. W. M., Ed. World Scientific Press: Singapore, 2008; pp 345-392.
6. Callegari, C.; Jäger, W.; Stienkemeier, F., Helium nanodroplets. In *Handbook of Nanophysics*, Sattler, K. D., Ed. CRC Press: 2011; p 4.1.
7. Grebenev, S.; Hartmann, M.; Lindinger, A.; Portner, N.; Sartakov, B.; Toennies, J. P.; Vilesov, A. F., Spectroscopy of molecules in helium droplets. *Physica B* **2000,** *280*, 65-72.
8. Grebenev, S.; Lugovoi, E.; Sartakov, B. G.; Toennies, J. P.; Vilesov, A. F., Spectroscopy of OCS-hydrogen clusters in He droplets. *Faraday Discuss* **2001,** *118*, 19-32.
9. Kunze, M.; Markwick, P. R. L.; Portner, N.; Reuss, J.; Havenith, M., Infrared-microwave double resonance spectroscopy of OCS in pure 4He and mixed 4He/3He clusters. *J. Chem. Phys.* **2002,** *116*, 7473-7485.
10. Dong, F.; Miller, R. E., Vibrational transition moment angles in isolated biomolecules: A structural tool. *Science* **2002,** *298*, 1227-1230.
11. Falconer, T. M.; Lewis, W. K.; Bemish, R. J.; Miller, R. E.; Glish, G. L., Formation of cold ion-neutral clusters using superfluid helium nanodroplets. *Rev. Sci. Instrum.* **2010,** *81*, 054101.
12. Morrison, A. M.; Raston, P. L.; Douberly, G. E., Rotational Dynamics of the Methyl Radical in Superfluid (4)He Nanodroplets. *J. Phys. Chem. A* **2012,** *117*, 11640-11647.
13. Raston, P. L.; Liang, T.; Douberly, G. E., Anomalous Λ-Doubling in the Infrared Spectrum of the Hydroxyl Radical in Helium Nanodroplets. *J. Phys. Chem. A* **2013,** *117*, 8103-8110.
14. Stienkemeier, F.; Ernst, W. E.; Higgins, J.; Scoles, G., On the use of liquid helium cluster beams for the preparation and spectroscopy of the triplet states of alkali dimers and other weakly bound complexes. *J. Chem. Phys.* **1995,** *102*, 615-17.
15. Bartelt, A.; Close, J. D.; Federmann, F.; Quaas, N.; Toennies, J. P., Cold metal clusters: helium droplets as a nanoscale cryostat. *Phys. Rev. Lett.* **1996,** *77*, 3525-3528.
16. Döppner, T.; Diederich, T.; Tiggesbaumker, J.; Meiwes-Broer, K. H., Femtosecond ionization of magnesium clusters grown in ultracold helium droplets. *Eur. Phys. J. D* **2001,** *16*, 13-16.
17. Diederich, T.; Tiggesbäumker, J.; Meiwes-Broer, K.-H., Spectroscopy on rare gas–doped silver clusters in helium droplets. *J. Chem. Phys.* **2002,** *116*, 3263-3269.

18. Choi, M. Y.; Miller, R. E., Infrared laser spectroscopy of imidazole complexes in helium nanodroplets: Monomer, dimer, and binary water complexes. *J. Phys. Chem. A* **2006,** *110*, 9344-9351.
19. Douberly, G. E.; Stiles, P. L.; Miller, R. E.; Schmied, R.; Lehmann, K. K., (HCN)m-Mn (M = K, Ca, Sr): Vibrational Excitation Induced Solvation and Desolvation of Dopants in and on Helium Nanodroplets. *J. Phys. Chem. A* **2010,** *114*, 3391-3402.
20. Kuyanov-Prozument, K.; Choi, M. Y.; Vilesov, A. F., Spectrum and infrared intensities of OH-stretching bands of water dimers. *J. Chem. Phys.* **2010,** *132*, 014304.
21. Loginov, E.; Gomez, L. F.; Chiang, N.; Halder, A.; Guggemos, N.; Kresin, V. V.; Vilesov, A. F., Photoabsorption of AgN (N ∼ 6-6000) Nanoclusters Formed in Helium Droplets: Transition from Compact to Multicenter Aggregation. *Phys. Rev. Lett.* **2011,** *106*, 233401.
22. Gomez, L. F.; Loginov, E.; Vilesov, A. F., Traces of Vortices in Superfluid Helium Droplets. *Phys. Rev. Lett.* **2012,** *108*, 155302.
23. Gomez, L. F.; Ferguson, K. R.; Cryan, J. P.; Bacellar, C.; Tanyag, R. M. P.; Jones, C.; Schorb, S.; Anielski, D.; Belkacem, A.; Bernando, C.; Boll, R.; Bozek, J.; Carron, S.; Chen, G.; Delmas, T.; Englert, L.; Epp, S. W.; Erk, B.; Foucar, L.; Hartmann, R.; Hexemer, A.; Huth, M.; Kwok, J.; Leone, S. R.; Ma, J. H. S.; Maia, F. R. N. C.; Malmerberg, E.; Marchesini, S.; Neumark, D. M.; Poon, B.; Prell, J.; Rolles, D.; Rudek, B.; Rudenko, A.; Seifrid, M.; Siefermann, K. R.; Sturm, F. P.; Swiggers, M.; Ullrich, J.; Weise, F.; Zwart, P.; Bostedt, C.; Gessner, O.; Vilesov, A. F., Shapes and vorticities of superfluid helium nanodroplets. *Science* **2014,** *345*, 906-909.
24. Ernst, W. E.; Huber, R.; Jiang, S.; Beuc, R.; Movre, M.; Pichler, G., Cesium dimer spectroscopy on helium droplets. *J. Chem. Phys.* **2006,** *124*, 024313.
25. Tiggesbaumker, J.; Stienkemeier, F., Formation and properties of metal clusters isolated in helium droplets. *Phys. Chem. Chem. Phys.* **2007,** *9*, 4748-70.
26. Atkins, K. R., Ions in liquid helium. *Phys. Rev.* **1959,** *116*, 1339-43.
27. Brindle, C. A.; Prado, M. R.; Janda, K. C.; Halberstadt, N.; Lewerenz, M., Structure and stability of $Ne^{+}He_n$: Experiment and diffusion quantum Monte Carlo theory with "on the fly" electronic structure. *J. Chem. Phys.* **2005,** *123*, 064312.
28. Kim, J. H.; Peterka, D. S.; Wang, C. C.; Neumark, D. M., Photoionization of helium nanodroplets doped with rare gas atoms. *J. Chem. Phys.* **2006,** *124*, 214301.
29. Peterka, D. S.; Kim, J. H.; Wang, C. C.; Neumark, D. M., Photoionization and Photofragmentation of SF_6 in Helium Nanodroplets. *J. Phys. Chem. B* **2006,** *110*, 19945-19955.
30. Chikina, I.; Shikin, V.; Varlamov, A. A., Effective mass of a charged carrier in a nonpolar liquid: Snowball effect in superfluid helium. *Phys. Rev. B: Condens. Matter Mater. Phys.* **2007,** *75*, 184518.
31. Coccia, E.; Bodo, E.; Marinetti, F.; Gianturco, F. A.; Yildrim, E.; Yurtsever, M.; Yurtsever, E., Bosonic helium droplets with cationic impurities: Onset of electrostriction and snowball effects from quantum calculations. *J. Chem. Phys.* **2007,** *126*, 124319.
32. Döppner, T.; Diederich, T.; Göde, S.; Przystawik, A.; Tiggesbaumker, J.; Meiwes-Broer, K.-H., Ion induced snowballs as a diagnostic tool to investigate the caging of metal clusters in large helium droplets. *J. Chem. Phys.* **2007,** *126*, 244513.
33. Mueller, S.; Mudrich, M.; Stienkemeier, F., Alkali-helium snowball complexes formed on helium nanodroplets. *J. Chem. Phys.* **2009,** *131*, 044319.

34. Smolarek, S.; Brauer, N. B.; Buma, W. J.; Drabbels, M., IR spectroscopy of molecular ions by nonthermal ion ejection from helium nanodroplets. *J. Am. Chem. Soc.* **2010,** *132*, 14086-14091.
35. Yang, S.; Ellis, A. M.; Spence, D.; Feng, C.; Boatwright, A.; Latimer, E.; Binns, C., Growing metal nanoparticles in superfluid helium. *Nanoscale* **2013,** *5*, 11545-11553.
36. Bartl, P.; Leidlmair, C.; Denifl, S.; Scheier, P.; Echt, O., On the size and structure of helium snowballs formed around charged atoms and clusters of noble gases. *J. Phys. Chem. A* **2014,** *118*, 8050-8059.
37. Schöbel, H.; Bartl, P.; Leidlmair, C.; Denifl, S.; Echt, O.; Märk, T. D.; Scheier, P., High-resolution mass spectrometric study of pure helium droplets, and droplets doped with krypton. *Eur. Phys. J. D* **2011,** *63*, 209-214.
38. Bartl, P.; Tanzer, K.; Mitterdorfer, C.; Karolczak, S.; Illenberger, E.; Denifl, S.; Scheier, P., Electron ionization of different large perfluoroethers embedded in ultracold helium droplets: effective freezing of short-lived decomposition intermediates. *Rapid Commun. Mass Spectrom.* **2013,** *27*, 298-304.
39. Ghazarian, V.; Eloranta, J.; Apkarian, V. A., Universal molecule injector in liquid helium: Pulsed cryogenic doped helium droplet source. *Review of Scientific Instruments* **2002,** *73*, 3606-3613.
40. Claas, P.; Mende, S. O.; Stienkemeier, F., Characterization of laser ablation as a means for doping helium nanodroplets. *Rev. Sci. Instrum.* **2003,** *74*, 4071-4076.
41. Bierau, F.; Kupser, P.; Meijer, G.; von Helden, G., Catching proteins in liquid helium droplets. *Phys. Rev. Lett.* **2010,** *105*, 133402.
42. Hartmann, M.; Miller, R. E.; Toennies, J. P.; Vilesov, A. F., High-resolution molecular spectroscopy of van der Waals clusters in liquid helium droplets. *Science* **1996,** *272*, 1631-1634.
43. Draves, J. A.; Luthey-Schulten, Z.; Liu, W.-L.; Lisy, J. M., Gas-phase methanol solvation of Cs+ : Vibrational spectroscopy and Monte Carlo simulation. *J. Chem. Phys.* **1990,** *93*, 4589.
44. Li, G.-Z.; Guan, S.; Marshall, A. G., Comparison of Equilibrium Ion Density Distribution and Trapping Force in Penning, Paul, and Combined Ion Traps. *Journal of the American Society for Mass Spectrometry* **1998,** *9*, 473-481.
45. Lewerenz, M.; Schilling, B.; Toennies, J. P., A new scattering deflection method for determining and selecting the sizes of large liquid clusters of helium-4. *Chem. Phys. Lett.* **1993,** *206*, 381-7.
46. Filsinger, F.; Ahn, D.-S.; Meijer, G.; von Helden, G., Photoexcitation of mass/charge selected hemin+, caught in helium nanodroplets. *Phys. Chem. Chem. Phys.* **2012,** *14*, 13370-13377.
47. Slipchenko, M. N.; Kuma, S.; Momose, T.; Vilesov, A. F., Intense pulsed helium droplet beams. *Rev. Sci. Instrum.* **2002,** *73*, 3600-3605.
48. Krasnokutski, S. A.; Huisken, F., Resonant two-photon ionization spectroscopy of Al atoms and dimers solvated in helium nanodroplets. *J. Chem. Phys.* **2015,** *142*, 084311.
49. Krasnokutski, S. A.; Huisken, F., Reactivity of Iron Atoms at Low Temperature. *J. Phys. Chem. A* **2014,** *118*, 2612-2617.
50. Braun, A.; Drabbels, M., Imaging the Translational Dynamics of CF3 in Liquid Helium Droplets. *Phys. Rev. Lett.* **2004,** *93*, 253401.
51. Braun, A.; Drabbels, M., Photodissociation of alkyl iodides in helium nanodroplets. I. Kinetic energy transfer. *J. Chem. Phys.* **2007,** *127*, 114303.

Chapter 7 Effective doping of low energy ions into superfluid helium droplets

Jie Zhang, Lei Chen, William M. Freund, and Wei Kong*

Department of Chemistry, Oregon State University, Corvallis, OR 97331

Manuscript for submission to the Journal of Chemical Physics, March 7, 2016

*Corresponding author, 541-737-6714, wei.kong@oregonstate.edu

Abstract

We report a facile method of doping cations from an electrospray ionization (ESI) source into superfluid helium droplets. By decelerating and stopping the ion pulse of reserpine and substance P from an ESI source in the path of the droplet beam, about 10^4 ion-doped droplets (one ion per droplet) can be recorded, corresponding to a pickup efficiency of nearly 1 out 1000 ions. We attribute the success of this simple approach to the long residence time of the cations in the droplet beam. The resulting size of the doped droplets, on the order of 10^5/droplet, are measured using deflection and retardation methods. Our method does not require an ion trap in the doping region, which significantly simplifies the experimental setup and procedure for future spectroscopic and diffraction studies.

7.1 Introduction

The invention of the superfluid helium droplet beam has triggered an avalanche of research activities involving microscopic superfluidity, optical spectroscopy, and ultrafast dynamics at cryogenic temperatures.[1-9] Unfortunately, the superior advantages of superfluid helium droplets cannot be easily transferred to the investigation of ions, both negatively and positively charged. A particular concern for cations is the possible strong matrix effect due to the heavy snowballs – a term used to describe tightly bound many helium layers to a cation dopant.[10] Studies of small cations formed upon ionization of neutral dopants have found evidence of metastable cluster ions,[11-15] but upon electronic or even vibrational excitation of the putatively doped droplets, non-thermal ejection of a free cation from the droplets has been reported.[16-21] Spectroscopic analysis has further revealed that for aniline, the helium matrix exerts minimal interference to the lineshape and linewidth of the cation in the infrared.[18] More recently, Filsinger *et al* have embedded hemin$^+$ from an electrospray ionization source (ESI) in superfluid helium droplets and reported non-thermal ejection of the dopant upon resonant excitation of the chromophore.[19] In this case, the helium environment has caused a slight blue shift in the electronic transition, and the linewidth of the transition is narrower than that from the gas phase. Filsinger *et al* have also reported that ejection involves more than one photon and the yield depends on the size of the droplet.[19] So far one can conclude that the bonding structure of a cation inside a droplet is far from uniform and simple, and that perhaps

there is a complete spectrum of variations in bonding structure and strength depending on the nature of the cation.

We have been interested in doping of cations in superfluid helium droplets not for spectroscopic studies but for electron diffraction of laser aligned protein ions.[22] Our idea involves embedding protein ions into superfluid helium droplets for laser induced alignment and then electron diffraction of aligned molecules for oversampling, phase retrieval, and structural refinement. The ultracold rotational temperature inside a droplet is ideal for effective field induced orientation.[23-25] However, a unique requirement of our experiment is the size of the doped droplets: although as a light atom, helium has a small diffraction cross section, when more than 1000 helium atoms surround a dopant, diffraction from the helium atoms can overwhelm the signal from the dopant. For this reason, we need to not only maximize the number of cation doped droplets but also minimize the resulting size of the doped droplets for diffraction.

An advantage offered by ion doped droplets, as compared with neutral doped droplets, is the net charge of the doped droplets: one can use electric fields to manipulate and measure charged particles. In a previous study, we have generated cesium cations from a thermionic emission source and measured the size distribution of the resulting doped droplets.[26] An anticorrelation between the doping efficiency and the kinetic energy of the incident ions has been observed. Based on the calculation of the droplet size distribution under different nozzle temperatures, we have attributed the increase in doping efficiency at low nozzle temperatures to the

increase in the number of viable sized droplets. The adverse effect of the kinetic energy on doping was attributed to the limited deceleration of a fast moving ion inside a droplet, resulting in many fast ions directly penetrating through the droplet.

In this report, we describe a simple approach of doping ions from an electrospray ionization source into superfluid helium droplets. Compared with literature reports, our method does not require an ion trap to enhance the interaction between the droplet beam and the incident ions. Instead, a stopper electrode decelerates the incident ions to maximize the doping efficiency. This unique design extends our investigation of doping efficiency to the extremely low kinetic energy regime for the incident ions, below the lower limit of 20 eV from our previous work on cesium cations.[26] We report similar numbers of doped droplets and similar size distributions as those reported from an experiment with an ion trap.[19] The simplicity of our setup, on the other hand, makes it straightforward to integrate with future spectroscopic or diffraction experiments. More importantly, the simple geometry allows qualitative modeling of the doping process.

7.2 Experiment

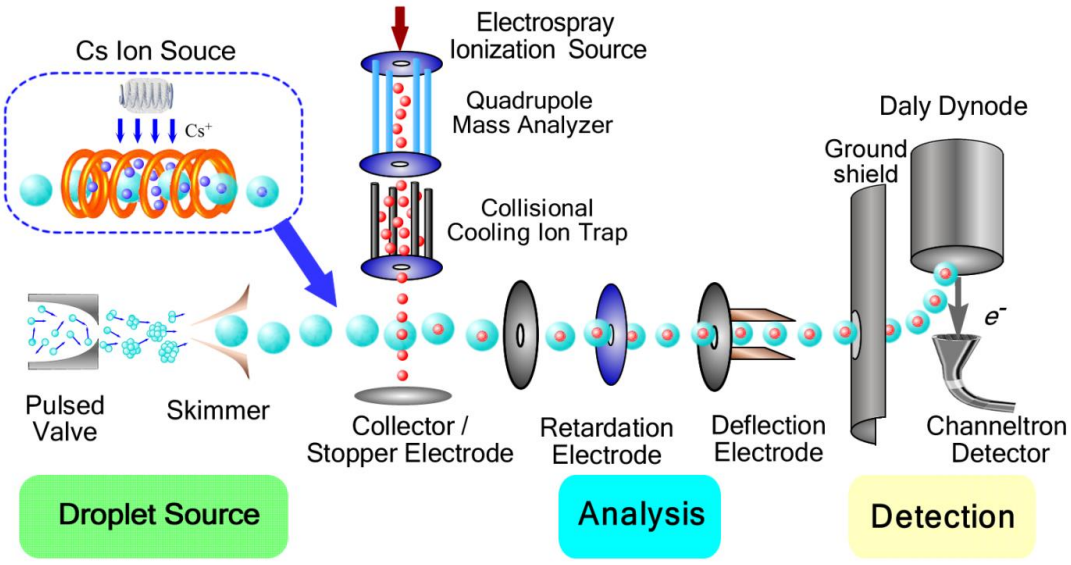

Fig.7.1. Experimental setup showing the arrangement of the electrospray ionization source, the superfluid helium droplet source, and the analysis region of the doped droplets including the Daly dynode detector. The cesium source was temporarily used to calibrate the gain of the Daly dynode, and it was removed for the doping experiment of the ions from the ESI source.

Figure 7.1 shows the schematic of the experimental setup. The droplet source was described in detail in a previous publication.[26] It consisted of a pulsed valve (Parker Hannifin Corp, Series 99) with a nozzle diameter of 500 microns cooled down to a minimum of 15 K using a closed-cycle helium cryostat (APF cryogenics, HC-4 MK1). The helium droplet beam was collimated by a 5 cm long skimmer of 2 mm in diameter (Beam Dynamics) located 12 cm downstream from the nozzle. Ultrapure (99.999%) helium at about 30 - 50 atm was released into vacuum to generate the superfluid helium droplets. The ion source was adapted from a reflectron mass spectrometer with electrospray ionization (Bruker Daltonics, BioTOF), and the reflectron component was removed for this experiment. In addition to the ESI source, the apparatus also included a quadrupole mass selector and a

collisional cooling ion trap with nitrogen as the cooling gas. A pulsed voltage gate at the exit of the ion trap released the ions into the path of the droplet beam. The average kinetic energy of the released ions was controlled by the bias of the ion trap, and it was mostly in the range between 25 – 30 eV.

In the doping region, the ion beam passed through the droplet beam just once, but the ions were slowed down, stopped, and perhaps even returned by the bias voltage on the collector/stopper electrode. The electrode was wired to an operational amplifier and a mega-Ohm resistor, so that the absolute ion count from the ion trap could be obtained when the electrode was not intentionally biased. During the experiment, the bias on the electrode was adjusted to maximize the number of doped droplets.

Downstream from the droplet source, two different setups were used for two different types of measurements, similar to our previous report on cesium cations.[26] In the first experiment, two planar electrodes with one grounded and the other biased between -3 and +3 kV were used to deflect the doped droplets away from the detector. In the second experiment, a retardation electrode was used instead of the deflectors, with the intension of stopping low energy (small doped droplets) thereby resolving the size of the doped droplets.

Further downstream from the analysis region is a Daly dynode detector, similar to the one used by Filsinger et al.[19] A ground shield protected the high voltage dynode biased at -20 kV, and a channeltron facing the dynode recorded the secondary electrons emitted from the dynode. The system functioned in an analogue

mode, and a voltage signal was representative of the number of charged particles hitting the dynode. To obtain the absolute number of doped droplets, we calibrated the gain of the Daly detector using a copper target wired with an operational amplifier and a giga-Ohm resistor. Unfortunately, the ion count from the current experiment with an ESI source was too low to be observable on the copper target, so we resorted to cesium doped droplets using our thermionic source. Also shown in the source region of Fig.7.1 is the thermionic emission ion source for cesium used in a previous experiment.[26] The huge number of cesium ions from this source was sufficient to generate more than 10^4 doped droplets per pulse, large enough for the copper target to respond with voltage pulses in the milliVolt range. We first recorded the voltage pulse, for example 183 mV, from the Daly dynode, and then replaced the dynode assembly by the copper target and recorded a voltage trace on a calibrated oscilloscope. The voltage trace was then converted into a current trace, and integration of the current trace yielded the number of ion-doped droplets of 10^4. We then assumed that a voltage pulse of 183 mV on the Daly dynode should correspond to 10^4 ion-doped droplets. The linearity of the correlation was checked throughout the response range of the copper target. We also tried the integrated peak from the pulse of the Daly dynode and concluded that the peak area was directly proportional to the peak intensity throughout the response range of the dynode. Although we took the liberty of extending the linear conversion between the voltage pulse of the Daly dynode and the number of doped ions to a lower range in the cases of reserpine and substance P, we believe that our numbers should be trustworthy within an order of magnitude.

It is worth noting that in all cases of direct ion doping,[19, 27] including our own, the probability of picking up more than one ion is negligible. This is because of the space charge limit of 10^7ions/cm^3, which is equivalent to a doping pressure of 10^{-9} Torr. For droplets with sizes of 10^6 atoms/droplet, the probability for a first encounter with one ion is less than 0.1%, hence a second encounter is statistically impossible.

Two standard samples in mass spectrometry from Sigma Aldrich were used, with molecular weights of 609 g/mol for reserpine and 1348 g/mol for substance P. Reserpine is an indole alkaloid used as an antipsychotic and antihypertensive drug, and substance P is a neuropeptide containing a chain of 11 amino acid residues. The former only ionizes into a singly charged cation (denoted as R^+ in the following), but the latter has two possible ions, and only the doubly charged ion (denoted as sP^{2+}) was chosen because of its higher abundance from the ESI source. Both samples were dissolved in 1:1 water acetonitrile solution with a final concentration 1.8×10^{-4} M, and to increase the ionization yield, we also added two drops (~ 0.1 ml in total) of 1% formic acid into the ~2 ml solution, with a resulting pH value between 4 and 5. At a flow rate of 200 - 700 µl/hour, the total number of ions released from the ion trap arriving at the collector electrode was ~10^7 ions/pulse.

7.3 Results

With this relatively simple setup for doping, we were surprised when we first released the reserpine ions from the ESI source and directly observed doped droplet signal on the Daly detector. The source temperature of the droplet beam was kept at

15 K. The collector/stopper electrode was unbiased, and the connected resistor was showing a total ion count of ~10^7 ions/pulse. The signal on the Daly dynode showed a dependence on the relative timing of the droplet beam and the ion exit gate, and no signal could be detected when the relative timing was shifted by ±150 μs away from the optimal condition. We then varied the voltage on the stopper electrode, and Fig.7.2 shows the change in the number of doped droplets with the voltage on the stopper electrode. Fast increase in the number of doped droplets is observable when the voltage on the stopper electrode is increased from 40 to 50 V, after which the rise slows down and reaches a peak value. Above 60 V, the doped droplet signal drops precipitously, and no doped signal is observable when the voltage reaches 80 V. Overall, the addition of a deceleration voltage on the stopper electrode has an effect of more than doubling the count of doped droplets, from less than 4000 at no bias to over 10000 doped droplets at 60 V.

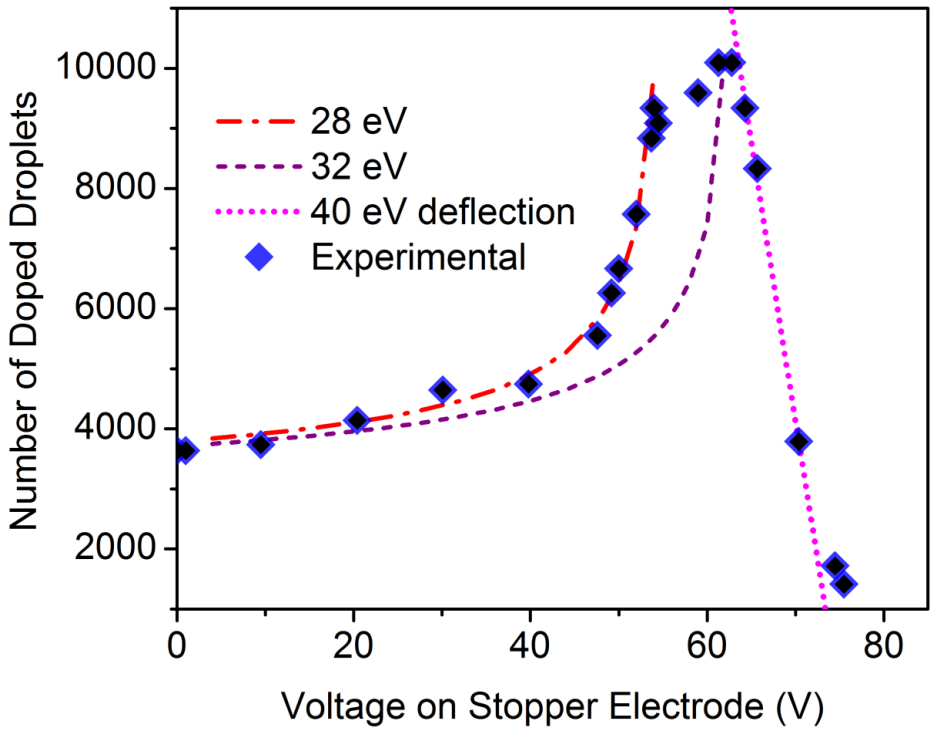

Fig.7.2. Dependence of the number of reserpine doped droplets on the voltage of the stopper electrode. The diamonds represent the experimental data, and the lines are calculations proportional to the residence time of the ions inside the droplet beam (see Discussion): the dashed lines correspond to ions with initial kinetic energies of 28 and 32 eV passing through the droplet beam once, and the dotted line corresponds to an initial kinetic energy of 40 eV and the ions are deflected back inside the droplet beam.

Fig.7.3 shows the results from the deflector experiment where doped droplets were driven out of the system by an increasing deflection voltage. The two types of ions R^+ and sP^{2+} have similar mass-to-charge ratios, but substance P is about twice as heavy as reserpine with twice the number of atoms and twice the heat capacity. At 15 K, the total number of doped droplets of R^+ is almost twice of that of sP^{2+}, both on the order of thousands per pulse. Based on the ion count recorded at the stopper

electrode, the resulting doping efficiency is just below 1‰. This value is about a fraction of that (5‰) from our previous work on doping of cesium ions at a source temperature of 14 K.[26] Limited by the deteriorating performance of the cryostat, unfortunately, we could not consistently lower the source temperature to below 15 K for more measurements, as we did in the cesium experiment. At this stage, we can only qualitatively state that from cesium to reserpine to substance P, with the increase in the complexity and weight of the dopant, the doping efficiency seems to be decreasing.

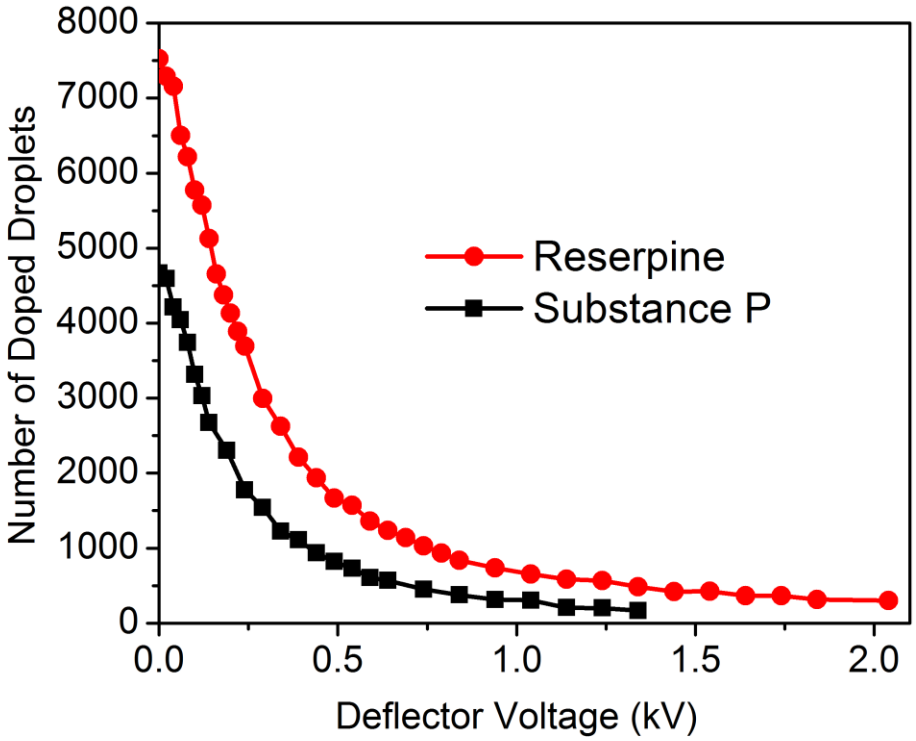

Fig.7.3. Change in the number of doped helium droplets with increasing deflection field.

The voltage on the deflectors determines a lower size limit for the detectable ions if all droplets travel with the same velocity, hence the horizontal axis of Fig.7.3

can be converted to the size limit based on the experimental geometry. Differentiation of the ion signal vs. the droplet size limit should produce the size distribution of the doped droplets. In Fig.7.4, we have fitted the resulting size distribution using the log-normal function,[28]

$$P_N(N) = (N\sigma\sqrt{2\pi})^{-1}\exp[\frac{-(\ln N-\mu)^2}{2\sigma^2}], \quad (7.1)$$

where $P_N(N)$ is the probability of a droplet consisting of N helium atoms, and the parameters σ and μ are the standard deviation and the mean of lnN. The fitting results are similar for both ions, on the order of 10^6 for the mean and 2×10^5 atoms/droplet for the most probable size. These sizes are about 1/10 of those from the experiment on cesium.[26]

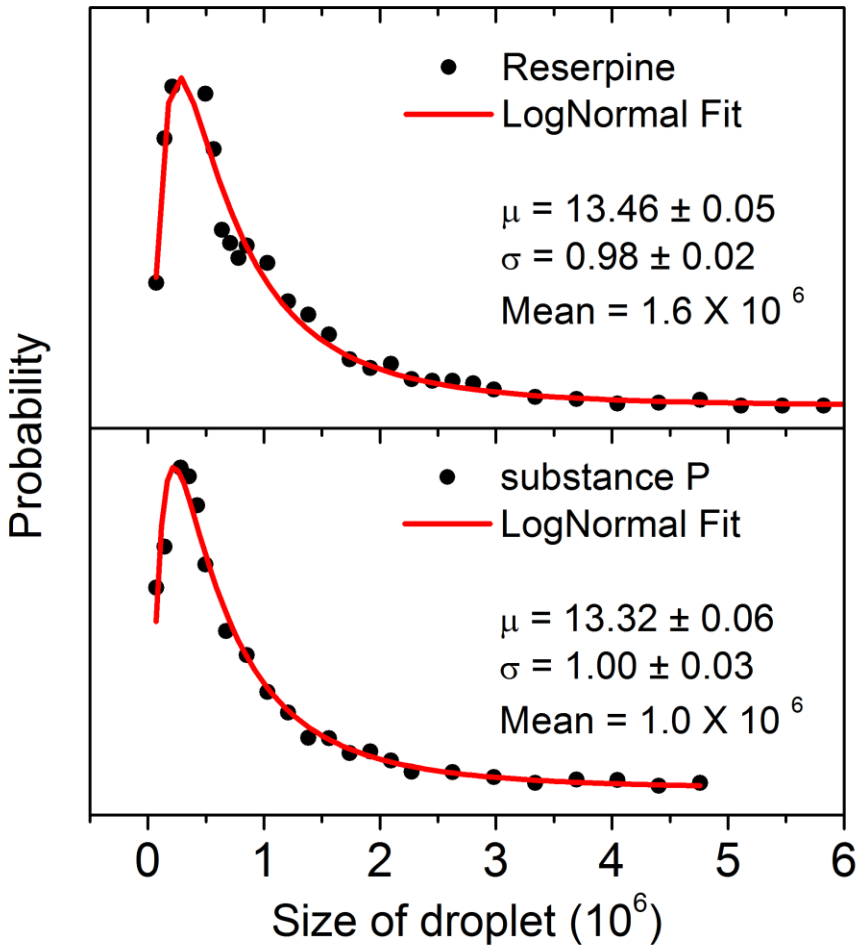

Fig.7.4. Log-normal fitting of the droplet size distributions of R^+ and sP^{2+} doped droplets. The fitting parameters using Eq.7.1 is also shown in the figure.

In another effort, we grounded the deflection electrodes and biased the retardation electrode. The retardation electrode was made of a copper sheet with a central mesh (50 × 50 mesh plain and 0.001 inch in wire diameter) for ion transmission. Only doped droplets with sufficient kinetic energy can overcome the retardation field and reach the detector. Fig.7.5 shows the change in the ion count as a function of the retardation voltage. The smaller initial ion count than that from the

previous deflection experiment (Fig.7.3) is reflective of the fluctuation level of the ESI source on a day-to-day basis.

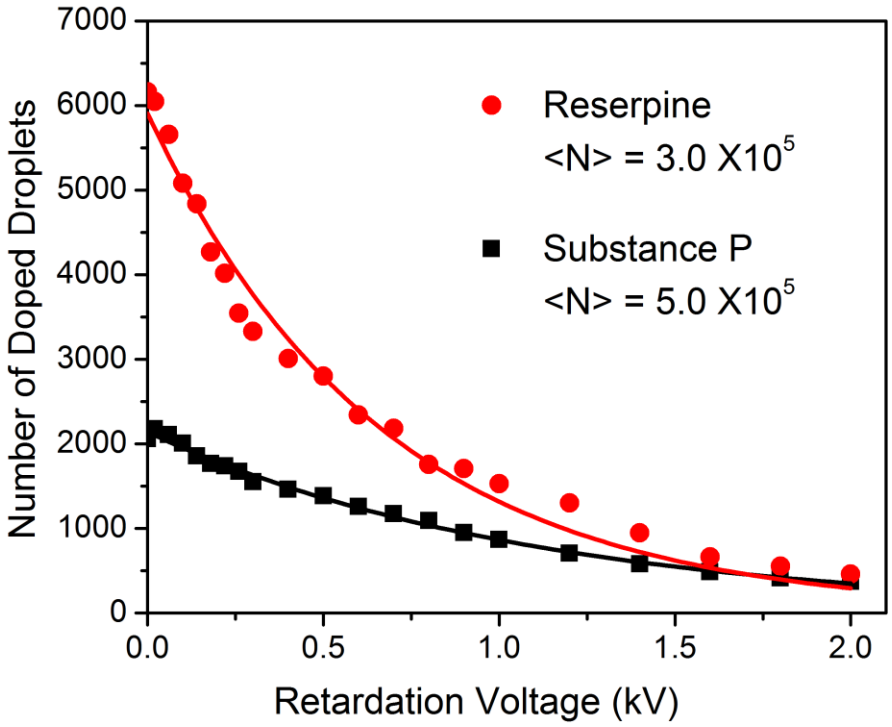

Fig.7.5. Retardation experiment showing the change in the number of doped droplets as a function of a retardation field. A single exponential fitting of the experimental data is also shown.

Although in theory, both the retardation and the deflection experiments should reveal the same size distribution, attempts to fit the data from the retardation experiment to a log-normal distribution were unsuccessful. Instead, we used a single exponential function to fit the experimental data, and the resulting average size from the fitting was on the order of 10^5/droplet . This value is about half to a third of that from the deflection experiment. The discrepancy, as we speculated in the experiment of cesium,[26] is probably related to the different functional modes of the deflection and

the retardation experiment. In the deflection experiment, smaller droplets were steered away from the path of the larger droplets, while in the retardation experiment smaller droplets were turned back towards the incoming larger droplets. At this stage, however, we do not have a good explanation for the discrepancy.

The average droplet sizes from this experiment and that from our previous experiment with cesium ions[26] are more than one order of magnitude larger than those from typical subcritical supersonic expansions.[29] One reason is probably related to the design of the pulsed valve, which has been considered to generate unusually large droplets based on reports from Bierau *et a1* and Filsinger *et al*.[19, 27] Another reason, which applies to all types of sources, is that smaller droplets do not have a high enough pickup efficiency to be doped and hence detected. The resulting measurement based only on charged droplets necessarily shifts to larger sizes. At 15 K and 50 atm for the pulsed valve, the source is close to the isentrope dividing subcritical and supercritical expansions, hence the final fitting result for the droplet size using log-normal and exponential functions could go awry. In fact, the profiles of Fig.7.5 are statistically better represented by bi-exponential functions, and the slower decay component dominates both profiles, corresponding to an average size of ~5×10^5 atoms/droplet for both reserpine and substance P. Attempts to fit the profiles of Fig.7.4 using exponential functions have also been successful, resulting in an average size of 9×10^5 and 6×10^5 atoms/droplet for reserpine and substance P. Although numerically different, these fitting results are in reasonable agreement, and the basic conclusion from this experiment remains the same, i. e., the average size of ion doped droplets is on the order of 10^5 atoms/droplet for reserpine and substance P.

Unfortunately, limited by the much lower level of signal at higher source temperatures and the achievable lowest temperature of the cryostat (15 K), experiments in other temperature ranges were unsuccessful. Variations in the stagnation pressure from 10 atm to 50 atm did not produce substantial improvements at any of the achievable temperatures, since unlike temperature, pressure for a pulsed valve plays a complicated role, and its effect on the droplet size was limited in our case.

7.4 Discussion

A major difference of the current experiment from the work of Bierau *et a1* and Filsinger *et al* is the missing ion trap for doping.[19, 27] Our experiment demonstrates that even without a trap, we can generate doped droplets near 10^4/pulse, comparable with that from Bierau *et a1*[27]. An ion trap typically ensures a high ion concentration -- close to the space charge limit -- for doping, thereby it is favored for increasing the number of doped droplets. However, the operation of an ion trap requires filling of the trap with ions and collision gas and pumping of the collision gas prior to droplet doping. This filling and pumping procedure interrupts the continuity of the experiment. Moreover, depending on the trajectories and the kinetic energies of the ions in the trap, the number of crossings between an ion and the droplet beam and the overall effective interaction time are difficult to model.

The lack of any type of ion trap in the doping region of the current design does not allow oscillatory trajectories of the incident ions in and out of the droplet beam. In the meantime, it also eliminates any potential trap for doped droplets along

the path of the droplet beam. Falconer *et al* used a biased ion collector to pull the sodium ions into the path of the droplet beam for doping.[30] In our own work on doping of cesium ions, a biased grid was used to trap the ions in the doping region, and the incident ions were able to traverse the region ~15 times.[26] However, the biased ion collector or grid can also trap small doped droplets, as discussed in both previous publications.[26, 30] The effect of a potential trap at 20 eV is elimination of doped droplets with less than 10^4 helium atoms from reaching the detector. In our current experiment with the doping region biased slightly positive for the incoming cations, essentially all doped droplets can reach the detector. Upon doping, about 10^4 helium atoms need to be evaporated to absorb a kinetic energy of 25 eV. If half the momentum of the incident ions is transferred to the doped droplet along the same transverse direction perpendicular to the droplet beam – an over exaggeration, the maximum gain in transverse velocity is 30 m/s. Given the distance between the doping region and the detector of 20 cm, the exit ions in the most extreme case would be off axis by 1.5 cm. The diameter of the hole on the shield for the Daly detector is 2.5 cm, thus almost all doped droplets can be detected, without discrimination against small droplets.

7.4.1 Effect of residence time on doping efficiency

A possible reason for the success of this simple setup is the low kinetic energy of the incident ions for doping. We simulated the electrostatic potential of the doping region using Lorentz-EM (Integrated Engineering Software, Winnipeg, Manitoba, Canada), a software package specially designed for magnetic analysis and for analysis

of charged particle trajectories in the presence of electric and magnetic fields. When the voltage on the stopper electrode was 60 V, given the geometry of the doping region, ions with a kinetic energy of 30 eV would be returned near or just pass the center of the doping region. We therefore suspect that perhaps the doping efficiency was related to the residence time of the ions in the droplet beam. Our droplet beam had a duration of 200 – 300 μs, and the ion beam from the exit electrode of the ion trap was ~150 μs. It is therefore reasonable to assume that to the incident ions, the droplet beam was pseudo-continuous. We then performed a crude calculation on the residence time of the ions in the path of the droplet beam based on the geometry shown in Fig.7.6.

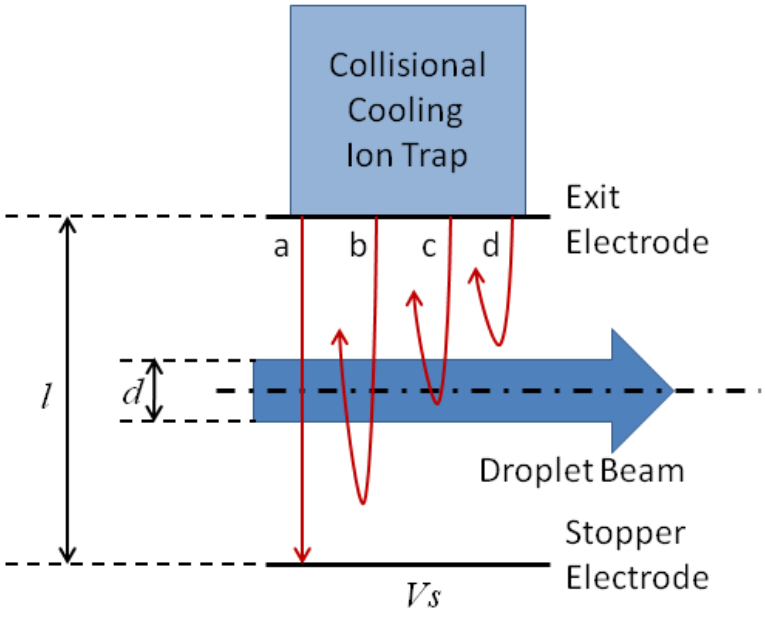

Fig.7.6. A simplified geometry of the experimental setup for modeling the residence time of ions from the ion trap in the droplet beam. The arrows labeled a – d represent four different possible ion trajectories depending on the initial kinetic energy of the ions and the bias on the stopper electrode.

For simplicity, we assumed that the droplet beam was in the midpoint between the stopper electrode and the exit electrode of the ion trap (a slight deviation from our true experimental setup), and the distance between the two electrodes was l = 18 cm. The width of the droplet beam was assumed to be d = 5 mm. By further assuming that when the exit gate opened (grounded), the electric field across the doping region was uniformly determined by the voltage on the stopper electrode V_s, we can calculate the residence time t_1 of the ion beam passing through the droplet beam with an initial kinetic energy E_0:

$$t_1 = \frac{l}{V_s}\sqrt{\frac{2m}{q}}\left(\sqrt{\frac{E_0}{q} - \frac{l-d}{2l}V_s} - \sqrt{\frac{E_0}{q} - \frac{l+d}{2l}V_s}\right), \tag{7.2}$$

where m and q are the mass and charge of the ions. As the stopper voltage increases, some ions will be stopped and returned and perhaps even reenter the region of the droplet beam, as shown by traces b – d in Fig.7.6. If the turning point is outside the droplet beam and the ion reenters the droplet beam (trace b), then the residence time should be simply twice of t_1. If the turning point is within the width of the droplet beam (trace c), the residence time of the ion inside the droplet beam can be calculated by

$$t_2 = \frac{2l}{V_s}\sqrt{\frac{2m}{q}}\left(\sqrt{\frac{E_0}{q} - \frac{l-d}{2l}V_s}\right). \tag{7.3}$$

In a simple-minded approach, we can assume that the number of doped droplets is directly proportional to the residence time of the ions in the droplet beam. We then introduce two adjustable parameters α_1 and β_1 to represent the scaling of the ion

signal (I) with the residence time and a base line. Scenarios a and b can then be fitted using

$$I = \alpha_1 t_1 + \beta_1. \quad (7.4)$$

The dashed lines in Fig.7.2 show the result obtained when $\alpha_1 = 7.7 \times 10^8$ and $\beta_1 = 2500$. The short dashed line was obtained by assuming $E_0 = 28$ eV, while the long dashed line was by assuming $E_0 = 32$ eV. As the stopper voltage increases from 40 to 50 V, ions with higher and higher kinetic energies begin to spend more time in the doping region, resulting in increased signal. This simple model has reproduced the rise edge of the doped droplet, and it also demonstrates that with only 4 eV of extra kinetic energy from 28 to 32 eV, the position of the sharp rise shifts by 8 V. We can therefore deduce that the width of the peak is related to the energy spread of the ion beam.

It is worth noting that this crude fitting made no distinction between traces a and b (Fig.7.6), and it should only be treated as a qualitative interpretation of the experimental result. When the kinetic energy is reduced close to zero at the turning point, stray fields start to play an overwhelming role, and intrinsic divergence of the ion beam will also diminish the number of returned ions. The effective resident time of the returned ions should be much smaller than that of the entering ions. In fact, the agreement between calculation and experiment seems to imply that perhaps none of the returned ions had a chance to interact with the droplet beam.

A similar argument can be used for the calculation of traces c and d: we used $\alpha_2 = ½\ \alpha_1$ but a different β_2 value (-12500) to simulate the effect of deflection of the stopper electrode using the modified formula:

$$I = \alpha_2 t_2 + \beta_2. \tag{7.5}$$

The dotted line in Fig.7.2 was obtained by assuming E_0 = 40 eV. This value can be considered the cutoff energy when all ions are deflected away from the droplet beam, as shown by trace d (Fig.7.6). Although the majority of the ions released from the ESI source have energies in the range of 28 and 32 eV, a high energy tail up to 40 eV is not totally out of reason. We therefore consider that 40 eV is the upper limit in the energy distribution for the ions released from the ion trap.

Crude as it is, this calculation has reproduced all the essential features of Fig.7.2. When the stopper voltage rises to above 50 eV, the residence time of low energy incident ions dramatically increases, resulting in much more effective doping and a sharp rise in the resulting number of doped droplets. As the stopper voltage further increases to 60 eV, lower energy ions can no longer penetrate into the droplet beam, resulting in a fast drop in the doped droplet signal, but in the meantime, higher energy ions begin to have longer resident times in the droplet beam, causing a moderate increase in the total number of doped ions. At even higher voltages on the stopper electrode, even the high energy tail of the bare ions can no longer penetrate into the droplet beam, and no more doped droplets can be generated. The net result of the above process is the peak of Fig.7.2. The width of the peak is determined by both

the energy spread of the droplet beam and the intrinsic rise and fall of even a mono-energetic ion beam within the finite width of the droplet beam.

The implications of the fitting parameters in Eqs.7.4 and 7.5 are worth considering. In Eq.7.4, the value of β_1 corresponds to the existence of doped droplets without any residence time ($t_1 = 0$), i. e., when the droplet beam is infinitely thin (d = 0 mm). This signal accounts for 2/3 of the overall number of doped droplets when the stopper electrode is grounded. Increase in residence time further increases the number of doped droplets, to a degree that it almost quadruples the final yield. This enhancement effect should be intimately related to the pseudo-continuous nature of the droplet beam. In Eq.7.3 for t_2, the factor two implies that the residence time for the return trip is considered to be identical as that of the incoming trip, hence it is an over estimation of the overall residence time. In Eq.7.5, this overestimate is eliminated by using $\alpha_2 = ½\ \alpha_1$. In essence, this approach is assuming that the return trip does not contribute to further doping, regardless of the position of the turning points as represented by traces b or c. The negative β_2 value, on the other hand, represents other unaccounted loss mechanisms when the turning point is inside (trace c) or prior to encountering the droplet beam (trace d). This is somewhat understandable since in the cases of traces c and d, the velocities of the ions are dramatically reduced once outside the ion trap. Stray fields and collisions with ambient residual gases and helium from the droplet beam can steer the ions away from the droplet beam.

In our previous work on doping of cesium cations,[26] we reported that the doping efficiency of Cs^+ rose dramatically with decreasing kinetic energy of incident ions. However, the conditions of the cesium experiment prevented us from investigating the doping efficiency below 20 eV. Since the cesium ion source was continuous, the residence time of the ion beam inside the droplet beam was not a parameter in affecting the doping efficiency. Instead, the resident time of a fast ion inside a droplet was limited because of the high velocity of the incident ion. The small mass of a helium atom is ineffective in slowing down a fast moving cesium ion. The doping efficiency was therefore discovered to be inversely related to the energy of the ions. In essence, the two scenarios of doping, either with a continuous or a pulsed ion source, demonstrate the same common factor in determining the doping efficiency: ions have to be decelerated inside the droplet or the droplet beam to be captured.

7.4.2 Ion size and droplet size

A major motivation of the current experiment is to prepare droplet cooled protein ions for laser alignment and electron diffraction. Our previous work has concluded that for phthalocyanine gallium chloride, there can be no more than 1000 helium atoms surrounding the neutral molecule during diffraction.[22] Otherwise, the background from the helium atoms would overwhelm the diffraction signal of the embedded molecules. Although reserpine and substance P both have more atoms to contribute to the diffraction signal, the current size of doped droplets is still too large.

Methods of size reduction or non-thermal ejection will be necessary to strip the helium atoms before diffraction.

On the other hand, the most probable size from the current experiment at 10^5/droplet is an order of magnitude smaller than that from cesium.[26] Compared with cesium, reserpine and substance P have ~100 times more atoms, which require 10^3 helium atoms to remove the thermal energy of these ions. This amount of helium atoms is negligible compared to that required to absorb the kinetic energy of 25 eV of the bare ions. In this sense, the extra heat capacity of the compound ions is not the reason for the one order of magnitude decrease in size compared with droplets doped with Cs^+. On the other hand, compound ions have larger collisional cross sections and lower velocities than light atomic ions, which could be beneficial for doping of smaller sized droplets. This argument would lead to increased ion count for doped R^+ and sP^{2+} than for doped Cs^+ under the same source temperature and the same number of bare ions. The number of Cs^+ ions in the doping region of our previous experiment was difficult to measure, but the actual numbers of doped droplets from this experiment using an ESI source are lower than that from the experiment with a thermionic cesium source under the same temperatures for the pulsed valve.[26] More investigations using a wider variety of ions are necessary to resolve this issue.

In summary, we have demonstrated a simple approach to effectively dope ions from an electrospray ionization source into superfluid helium droplets. Without employing an ion trap in the doping region, we eliminate the need of trap filling and collision gas pumping, making the setup much simpler to be integrated with

subsequent experiments. The success of this simple approach can be attributed to the low kinetic energy of the incident ions. Using a crude model, we have calculated the residence time of the incident ions in the droplet beam and discovered a direct correlation between the residence time and the doping signal. The resulting doped droplets of R^+ and sP^{2+} are smaller than those of Cs^+, but they are still too big for electron diffraction. The reason for the smaller sized droplets with the compound ions R^+ and sP^{2+} from an ESI source warrants further investigation.

Acknowledgement

This work is supported by the National Institute of General Medical Sciences (1RC1GM092054 -01 and 1R01GM101392-01A1) from the National Institutes of Health. The content is solely the responsibility of the authors and does not necessarily represent the official views of the National Institutes of Health. Additional support from the Murdock Charitable Trust, the Oregon Nanoscience and Microtechnologies Institute, and the Environmental Health Science Center at Oregon State University funded by the National Institute of Environmental Health Sciences (ES000210) are also deeply appreciated. We also thank Dr. Joe Beckman for his unwavering support, and Dr. Valery Voinov for his generous help with the mass spectrometer. Dr. Gert von Helden also provided us with the design of the Daly dynode and offered advice about the experiment.

7.5 References

1. Toennies, J. P., Helium clusters and droplets: microscopic superfluidity and other quantum effects. *Mol. Phys.* **2013,** *111*, 1879-1891.
2. Yang, S.; Ellis, A. M., Helium droplets: a chemistry perspective. *Chem. Soc. Rev.* **2013,** *42*, 472-484.
3. Echt, O.; Mark, T. D.; Scheier, P., Molecules and clusters embedded in helium nanodroplets. In *Handbook of Nanophysics*, Sattler, K. D., Ed. CRC Press: 2011; Vol. 2, pp 20.1-24.
4. Callegari, C.; Jäger, W.; Stienkemeier, F., Helium nanodroplets. In *Handbook of Nanophysics*, Sattler, K. D., Ed. CRC Press: 2011; p 4.1.
5. Kuyanov-Prozument, K.; Skvortsov, D.; Slipchenko, M. N.; Sartakov, B. G.; Vilesov, A., Matrix isolation spectroscopy in helium droplets. In *Physics and Chemistry at Low Temperatures*, Khriachtchev, L., Ed. Pan Stanford Publishing Pte. Ltd.: 2011; pp 203-230.
6. Szalewicz, K., Interplay between theory and experiment in investigations of molecules embedded in superfluid helium nanodroplets. *Int. Rev. Phys. Chem.* **2008,** *27*, 273-316.
7. Slenczka, A.; Toennies, J. P., Chemical dynamics inside superfluid helium nanodroplets at 0.37 K. In *Low Temperatures and Cold Molecules*, Smith, I. W. M., Ed. World Scientific Press: Singapore, 2008; pp 345-392.
8. Tiggesbaeumker, J.; Stienkemeier, F., Formation and properties of metal clusters isolated in helium droplets. *Phys. Chem. Chem. Phys.* **2007,** *9*, 4748-4770.
9. Küpper, J.; Merritt, J. M., Spectroscopy of free radicals and radical containing entrance-channel complexes in superfluid helium nanodroplets. *Int. Rev. Phys. Chem.* **2007,** *26*, 249-287.
10. Atkins, K. R., Ions in liquid helium. *Phys. Rev.* **1959,** *116*, 1339-43.
11. Mudrich, M.; Stienkemeier, F., Photoionisaton of pure and doped helium nanodroplets. *Int. Rev. Phys. Chem.* **2014,** *33*, 301-339.
12. Bartl, P.; Leidlmair, C.; Denifl, S.; Scheier, P.; Echt, O., On the size and structure of helium snowballs formed around charged atoms and clusters of noble gases. *J. Phys. Chem. A* **2014,** *118*, 8050-8059.
13. Mateo, D.; Eloranta, J., Solvation of Intrinsic Positive Charge in Superfluid Helium. *J. Phys. Chem. A* **2014,** *118*, 6407-6415.
14. Leal, A.; Mateo, D.; Hernando, A.; Pi, M.; Barranco, M.; Ponti, A.; Cargnoni, F.; Drabbels, M., Picosecond solvation dynamics of alkali cations in superfluid 4He nanodroplets. *Phys. Rev. B: Condens. Matter Mater. Phys.* **2014,** *90*, 224518.
15. Theisen, M.; Lackner, F.; Krois, G.; Ernst, W. E., Ionization Thresholds of Alkali Metal Atoms on Helium Droplets. *J. Phys. Chem. Lett.* **2011,** *2*, 2778-2782.
16. Lindebner, F.; Kautsch, A.; Koch, M.; Ernst, W. E., Laser ionization and spectroscopy of Cu in superfluid helium nanodroplets. *Int. J. Mass Spectrom.* **2014,** *365-366*, 255-259.
17. Mateo, D.; Hernando, A.; Barranco, M.; Loginov, E.; Drabbels, M.; Pi, M., Translational dynamics of photoexcited atoms in 4He nanodroplets: the case of silver. *Phys. Chem. Chem. Phys.* **2013,** *15*, 18388-18400.
18. Zhang, X.; Brauer, N. B.; Berden, G.; Rijs, A. M.; Drabbels, M., Mid-infrared spectroscopy of molecular ions in helium nanodroplets. *J. Chem. Phys.* **2012,** *136*, 044305.

19. Filsinger, F.; Ahn, D.-S.; Meijer, G.; von Helden, G., Photoexcitation of mass/charge selected hemin+, caught in helium nanodroplets. *Phys. Chem. Chem. Phys.* **2012,** *14*, 13370-13377.
20. Smolarek, S.; Brauer, N. B.; Buma, W. J.; Drabbels, M., IR spectroscopy of molecular ions by nonthermal ion ejection from helium nanodroplets. *J. Am. Chem. Soc.* **2010,** *132*, 14086-14091.
21. Ferreira, d. S. F.; Jaksch, S.; Martins, G.; Dang, H. M.; Dampc, M.; Denifl, S.; Märk, T. D.; Limao-Vieira, P.; Liu, J.; Yang, S.; Ellis, A. M.; Scheier, P., Electron attachment and electron ionization of acetic acid clusters embedded in helium nanodroplets. *Phys. Chem. Chem. Phys.* **2009,** *11*, 11631-11637.
22. Zhang, J.; He, Y.; Freund, W. M.; Kong, W., Electron Diffraction of Superfluid Helium Droplets. *J. Phys. Chem. Lett.* **2014,** *5*, 1801-1805.
23. Kong, W.; Pei, L.; Zhang, J., Linear dichroism spectroscopy of gas phase biological molecules embedded in superfluid helium droplets. *Int. Rev. Phys. Chem.* **2009,** *28*, 33-52.
24. Holmegaard, L.; Nielsen, J. H.; Nevo, I.; Stapelfeldt, H.; Filsinger, F.; Kupper, J.; Meijer, G., Laser-Induced Alignment and Orientation of Quantum-State-Selected Large Molecules. *Phys. Rev. Lett.* **2009,** *102*, 023001.
25. Choi, M. Y.; Miller, R. E., Infrared laser spectroscopy of imidazole complexes in helium nanodroplets: Monomer, dimer, and binary water complexes. *J. Phys. Chem. A* **2006,** *110*, 9344-9351.
26. Chen, L.; Zhang, J.; Freund, W. M.; Kong, W., Effect of Kinetic Energy on the Doping Efficiency of Cesium Cations into Superfluid Helium Droplets. *J. Chem. Phys.* **2015,** *143*, 044310.
27. Bierau, F.; Kupser, P.; Meijer, G.; von Helden, G., Catching proteins in liquid helium droplets. *Phys. Rev. Lett.* **2010,** *105*, 133402.
28. Lewerenz, M.; Schilling, B.; Toennies, J. P., A new scattering deflection method for determining and selecting the sizes of large liquid clusters of helium-4. *Chem. Phys. Lett.* **1993,** *206*, 381-7.
29. Buchenau, H.; Knuth, E. L.; Northby, J.; Toennies, J. P.; Winkler, C., Mass spectra and time-of-flight distributions of helium cluster beams. *J. Chem. Phys.* **1990,** *92*, 6875-89.
30. Falconer, T. M.; Lewis, W. K.; Bemish, R. J.; Miller, R. E.; Glish, G. L., Formation of cold ion-neutral clusters using superfluid helium nanodroplets. *Rev. Sci. Instrum.* **2010,** *81*, 054101.

Chapter 8 Getting the right sized droplets

To achieve electron diffraction of macromolecular ions doped in superfluid helium droplets, two conflicting requirements on the droplets size have to be compromised. Due to the background from helium atoms, electron diffraction of doped droplets is only observed in small sized droplets.[1] However, to successfully dope protein ions and to cool them down to 0.38 K via helium evaporation, large droplets are required. In this chapter, we test one possible resolution to this conflict by first producing large droplets for doping and then by collisional size reduction for diffraction. Unfortunately, limited by the available temperature range of the cryostat, only small sized droplets can be produced for this exploratory work. More quantitative experiments are required for a conclusive assessment. A unintended consequence of size reduction via collision is the loss of small droplets, and the net effect of size reduction has to be evaluated against the initial abundance of small sized droplets.

8.1 Simulation of collisional size reduction

The idea of collisional size reduction was initially based on two previous reports. In the work of Gomez *et al*[2], the authors measured the size distributions of helium droplets by "titrating" the droplet beam. Room temperature helium gas was introduced into a droplet beam, and from the disappearance of droplet related signal and the pressure dependence of the signal, they derived the size distribution of the droplet beam. One caveat of this experiment was the low transmission rate of small

sized clusters, since with the exception of collisions along the direction of the flight path, all other collisions introduce a velocity perpendicular to the flight axis. Smaller droplets are more prone to deviate from the flight path simply because of their smaller masses and hence higher velocity gains due to momentum conservation. To alleviate this problem and to take advantage of the charges of ion doped droplets, we turned to ion mobility spectroscopy (IMS)[3]. In a typical IMS experiment, a short flight region with a uniform field is generated by a stack of electrodes biased at increasing (or decreasing) voltages. Ions with larger cross sections experience more collisions and hence are slowed down by the colliding gas, and the flight time through the drift tube is indicative of the cross section. The uniform acceleration field is to increase the transmission of ions colliding with neutral gaseous species.

To design an effective collision cell and to understand the behavior of ion collisions with neutral particles, we built up a collision model as shown in Fig. 8.1 and analyzed the ion mobility in two different scenarios: a uniform field or a uniform potential inside the cell. The former setting is to imitate an ion mobility experiment, but the latter is experimentally simpler to achieve.

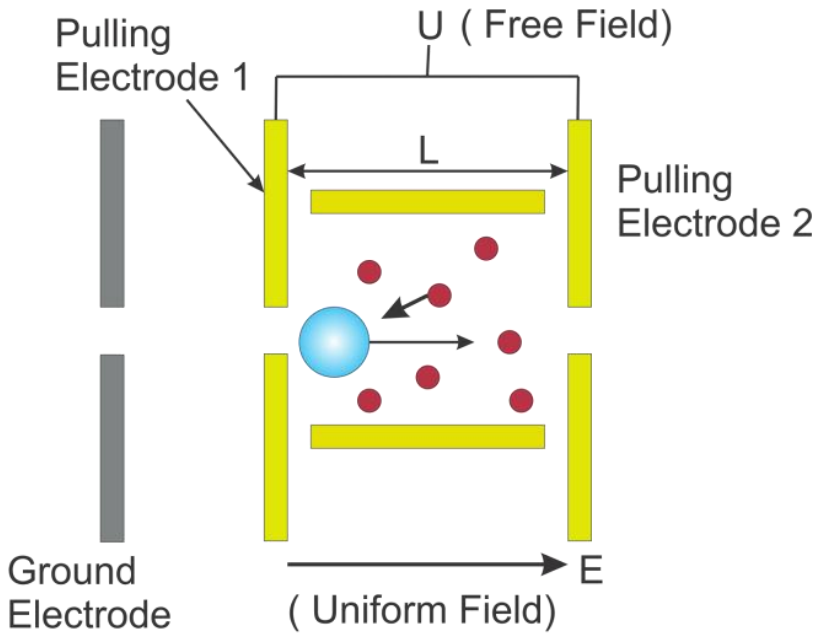

Fig.8.1. Simulation model of the collision cell. Two different scenarios are modeled: a uniform pulling field E through the collision cell or a uniform potential bias (free field) at potential U on the cell.

In Fig.8.1, a helium droplet with an original size N_x travels through a collision cell of L in length filled with neutral particles (helium or other inert gases). Assuming the collision gas is an ideal gas, its number density ρ is determined by,

$$\rho = \frac{P}{k_B T} \tag{8.1}$$

where P is the pressure and T is the ambient temperature of the collision cell. In our simulation, multiple collisions are considered sequentially, and each step removes a fixed number of helium atoms N_e from the droplet. Initially, the mean free path of a droplet is λ_0:

$$\lambda_0 = \frac{1}{\pi R_0^2 \rho} \quad , \tag{8.2}$$

where R_0 is the radius of the droplet. After the first collision with a neutral atom, the droplet evaporates a number of helium atoms and its radius reduces to $R_1 = 2.22\ (N_x - N_e)^{\frac{1}{3}}$ Å. Consequently, the new mean free path is increased to $\lambda_1 = \frac{1}{\pi R_1^2 \rho}$. The process continues for a number of times *s* before the droplet leaves the collision cell; hence, the sum of the mean free path of each step should be the same as the length of the cell. The final size of the droplet becomes N_{final}:

$$N_{final}(N_x) = N_x - \frac{1}{N_e}(N_x - (N_x^{\frac{1}{3}} - \frac{\pi \cdot 2.22^2 \cdot \rho \cdot N_e L}{3})^3). \quad (8.3)$$

In Eq. 8.3, the net effect of collisions is determined by $\rho \cdot L$. However, to limit the spatial spread due to velocity slip, a shorter collision cell with a higher internal pressure should be beneficial.

To limit the loss of small ions ($<10^5$) from collisions, we use electric fields for acceleration through the collision cell. Two different schemes are considered: the first involves accelerating the doped droplets before they enter the collision cell, but inside the cell there is no acceleration field – the uniform potential scenario. The other is to create a uniform field inside the cell and accelerate the droplets during collision. In this latter case, the final speed of a droplet coming out of the collision cell is :

$$V_{final}(N_x) = [V_0^2(N_x) + \frac{3 \cdot q \cdot E}{\pi \cdot 2.22^2 \cdot \rho \cdot m_{He} \cdot N_e}(-N_x^{-\frac{2}{3}} + N_{final}^{-\frac{2}{3}}(N_x))]^{\frac{1}{2}}. \quad (8.4)$$

with $V_0(N_x)$ the initial speed. In the case of uniform potential where doped droplets are accelerated by a negative voltage V before entering the collision cell, the final speed is written as:

$$V'_{final}(N_x) = (V_0^2(N_x) + \frac{2 \cdot q \cdot U}{m_{He} \cdot N_x})^{\frac{1}{2}} \quad (8.5)$$

A particularly important requirement for the next phase of the experiment, i. e. electron diffraction in a laser field, is spatial and temporal focusing of the ion doped droplets. For this, we have also simulated the speed distribution in the two different scenarios assuming L = 10 cm, P = 1mbar, and $V_0(N_x)$ = 400 m/s. To compare the effect of the two different scenarios, we chose a uniform field E = 100 V/cm and hence an acceleration voltage U = 1000 V. The resulting speed distributions are shown in Fig. 8.2. In the case of a uniform potential, the speed range is from 2271.6 m/s to 406.2 m/s for droplets with sizes between 10^4 and 10^7, while in the same size range, the speed distribution in a uniform field is about twice as large. Increasing both E and U increases the difference in speed distribution between these two scenarios. Therefore, for our purpose, we used the simpler approach of biasing the collision cell at a uniform potential.

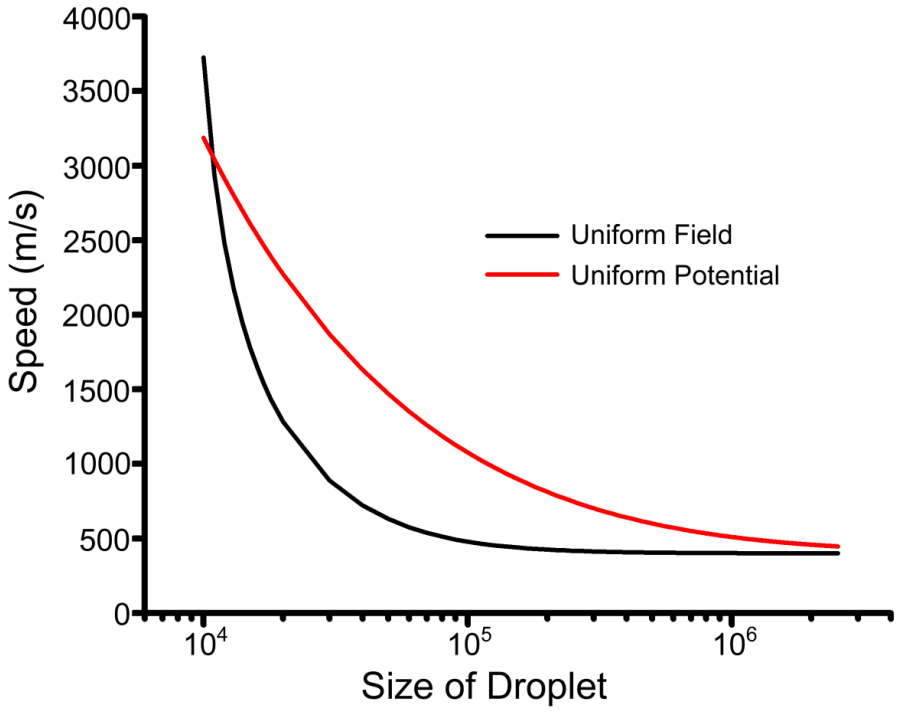

Fig.8.2. Velocity distributions under two different scenarios: uniform field and uniform potential

We have also simulated the trajectories of ion doped droplets using Lorentz-EM (Integrated Engineering Software, Winnipeg, Manitoba, Canada), and the result is shown in Fig.8.3. In the simulation, the collision cell and the acceleration electrodes are set at -2000 V and the flight tube at -4000 V. Unfortunately, we could not vary the size of the droplets in Lorentz, so we set the size to 10^5 with a constant kinetic energy of 100 eV. We assumed a diverging angle of 5^o and after passing through the flight tube, the droplet beam was observed to converge to the detector.

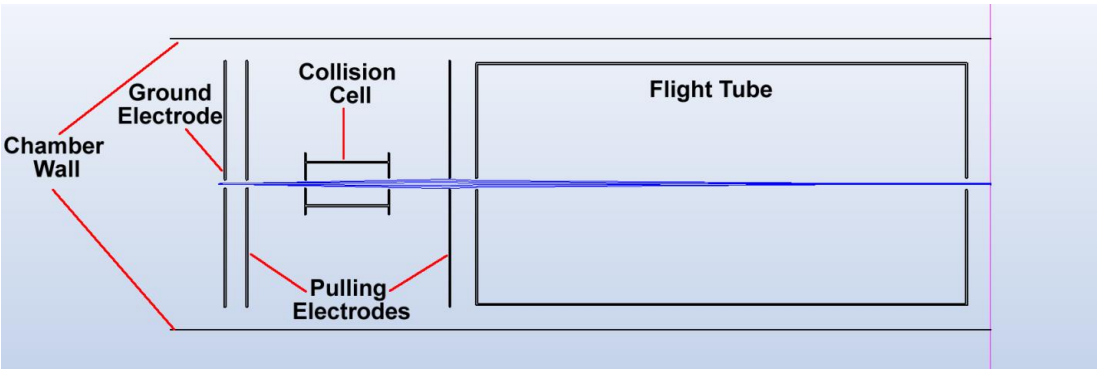

Fig.8.3. Simulation of the ion trajectories from Lorentz shows the focusing effect of the second acceleration electrode and flight tube.

Not considered in our calculation is the effect of collisions on the trajectories of the ion doped droplets. Side-on collisions not along the flight path introduce a velocity component perpendicular to the flight path. To minimize the deviation from this velocity component, we can accelerate the ions and reduce their overall flight time. In general, we expect that with increased bias on the collision cell and the flight tube, more ions should be transmitted into the detector. With increasing collisions, however, the ion count should demonstrate a monotonic decay.

8.2 Experimental setup

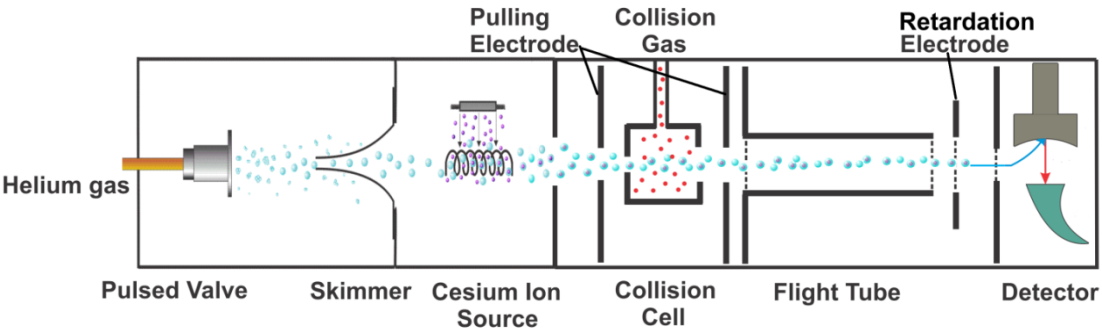

Fig. 8.4. Experimental setup of the size reduction experiment.

Fig.8.4 shows the setup of this collision experiment. Limited by the performance of our cryostat and the resulting low number of peptide doped droplets, we have resorted to cesium ions as our dopant. Further experiments with peptides will be performed after the upgrade of the cryostat. In this experiment, cesium ion doped droplets enter into a collision cell filled with a low pressure room temperature collision gas. Two extra large acceleration (pulling) electrodes separated by 130 mm with diameters of 90 mm and central openings of 7 mm are used to sandwich the cell. These plates are electrically connected with the collision cell to create uniform electric fields into and out of the collision cell, thereby minimizing the fringe fields from the collision cell. The collision cell and the two pulling electrodes are biased at 0 V~ -5000 V to attract doped droplets into the collision region. Between the ion source and the first pulling electrode, a ground electrode is used to prevent the negative voltage from the collision chamber into the ion source chamber. To characterize the resulting size of the doped droplet, a flight tube with a Daly-type dynode detector is arranged downstream from the collision cell.

The collision cell is housed in a six-way cross directly connected to the ion source. It is made of a copper tube of 28 mm in diameter and 50 mm in length. Both ends of the cell are sealed by a copper plate: the entrance plate has a central opening of 7 mm in diameter and the exit plate has a central opening of 9 mm diameter. For the convenience of physical support and supply of the collision gas, a copper tube of 28 mm in diameter and 76 mm in length is welded onto the collision cell in the perpendicular direction, and it is inserted into a PVC tube mounted on a 6” conflat flange with a central opening. A pressure transducer (MKS, 631) is mounted on the

other side of the same flange and can measure the pressure in the collision cell through the PVC tube as shown in Fig. 8.5. The collision cell is hermetically sealed from the ambient via the pressure transducer and the vacuum flange, but it is not sealed from the collision chamber because of the non-hermetic seal between the PVC tube and the copper tube.

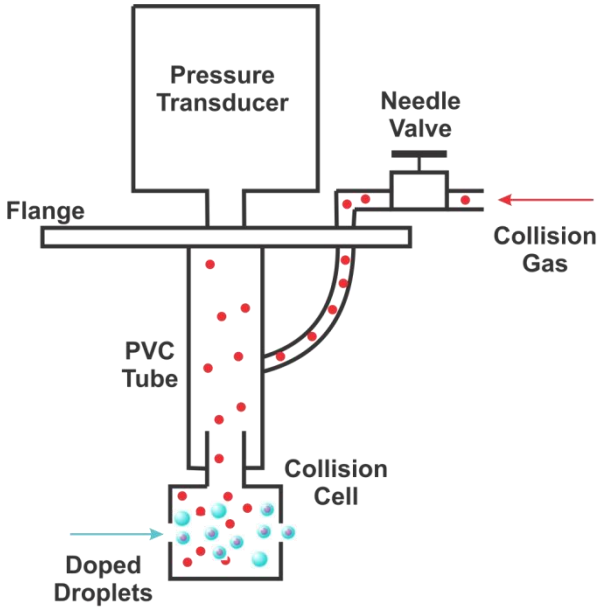

Fig.8.5. Schematic of the collision cell with the pressure transducer.

The collision gas is introduced through a plastic tube into the PVC tube to fill the collision cell. The flow rate of the collision gas can be controlled by a needle valve (Swagelok, B-S34-VH). The collision chamber is pumped by a Turbo molecular pump (Agilent, TV551NAV) and the internal pressure is indicated by an ionization gauge (Varian, 0571-K247-304). We used three different collision gases: helium (99.999%), nitrogen, and argon (99.5%~99.7%), and depending on the

response of the ion gauge for each gas, the pressure reading from the ionization gauge has to be corrected individually. During the experiment, the pressure inside the collision cell can be directly measured by the MKS pressure transducer, but the response range of the transducer is limited to 2×10^{-4} – 2 torr. Therefore, to read into the high vacuum range from 10^{-7} torr to 10^{-3} torr in the collision cell, we need to correlate the Varian ion gauge P_{ion} mounted inside the collision chamber but outside the collision cell to the readings of the MKS pressure transducer P_{MKS}. For this purpose, we performed a calibration experiment by adding different amounts of helium collision gas in the cell and recorded the corresponding pressures from the pressure transducer and the ion gauge. A linear relation between these two gauges has been established as:

$$P_{MKS} = 500(P_{ion} + 2 \times 10^{-7}) \tag{8.6}$$

in units of Torr. For example, when the chamber pressure is 3×10^{-6} Torr from the ionization gauge, the inside pressure of the collision cell is 1.6×10^{-3} Torr from the pressure transducer.

A flight tube is used to transport the size reduced ion doped droplets to the Daly-type dynode detector and to provide some size information. The flight tube is made of copper of 28 mm in diameter and 145 mm in length, and both ends of the tube are covered by fine meshes. Bias voltages from 0 V to -5000 V can be applied to the tube during the experiment. We also placed a retardation electrode before the detector (see chapter 6) to obtain more information on the size of the resulting droplets.

8.3 Results

8.3.1 General observation

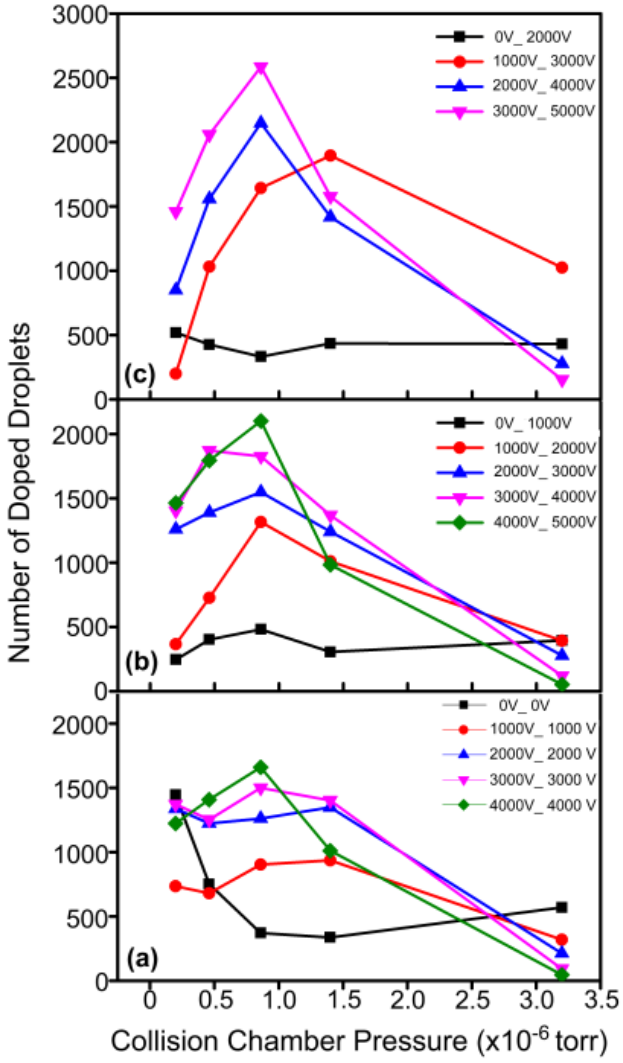

Fig.8.6. The number of doped droplets varied with both voltages applied on the collision cell and the flight tube at different collision pressures. In the annotation, the first voltage represents the bias on the collision cell and the second voltage shows the bias on the flight tube. The experimental uncertainty is about 5%.

Fig. 8.6 shows the variation of the number of doped droplets with the voltages on the collision cell and the flight tube under different pressures of helium in the collision cell. Panel (a) shows the results when the collision cell and the flight tube have the same voltage, panel (b) shows the results when there is a 1000 V difference between them, and panel (c) represents this voltage difference reaches 2000 V. When the collision cell is grounded, the number of doped droplets does not vary consistently with increasing pressure in the cell: without additional collisions, the signal in panel (c) with a bias of 2000 V on the flight tube is only one third of that in panel (a) with the flight tube grounded. While the fast decay of the ion count with increasing collisions in panel (a) is expected, the much smaller number of ions and its independence on the pressure of the collision cell in panels (b) and (c) with a biased flight tube are puzzling. The focusing effect from the flight tube predicted by the simulation of Fig. 8.3 is not obvious. On the contrary, the experimental data seem to suggest that the voltages on the flight tube are diverging the ion beam. Moreover, this divergence effect seems to diminish with increasing collision pressures, resulting in the seemingly independence of the ion signal on the collision pressure. Perhaps the increased transmission under higher bias voltages is largely canceled out by the divergence effect of the accelerating field.

The pulling effect of the bias voltage on the collision cell and the TOF tube is observable with the exception of panel (a) at a bias of 1000 V: the rest of the profiles consistently display increased number of doped droplets with increasing bias on the collision cell in the low pressure region. At the highest bias in panel (c), the ion count is 60% more than that under no bias without any added collision gas. In addition,

panel (c) with a higher bias on the flight tube does show a consistent higher ion count than that from panel (b) when the collision cell is biased below 3000 V (the highest bias achievable with our power supply under this setting).

In panels (b) and (c), the ion count increases with increased collision pressures from 2.0×10^7 Torr to 8.0×10^7 Torr. Our only plausible explanation for this surprising result is that the detection efficiency of our Daly detector is more sensitive to smaller masses.

These results reveal a complex situation in performing collisional size reduction. Simulations based on the same mass-to-charge ratio are clearly inadequate to capture the essence of the ion movement, as revealed by the surprising effect of the electric field on the collision cell and the flight tube. Moreover, the non-uniform sensitivity of the ion detector also adds another layer of complication. A more detailed calibration of the Daly detector, particularly its dependence on the mass of the incident ions, is necessary to fully interpret the experimental results. During the experiment, we have also discovered that some details of the result are dependent on the exact condition of the ion source, since after recoating the filament with a new paste, some of the profiles are shifted. At this stage, we hesitate to make quantitative statements about the results.

8.3.2 Size characterization of doped droplets after collision

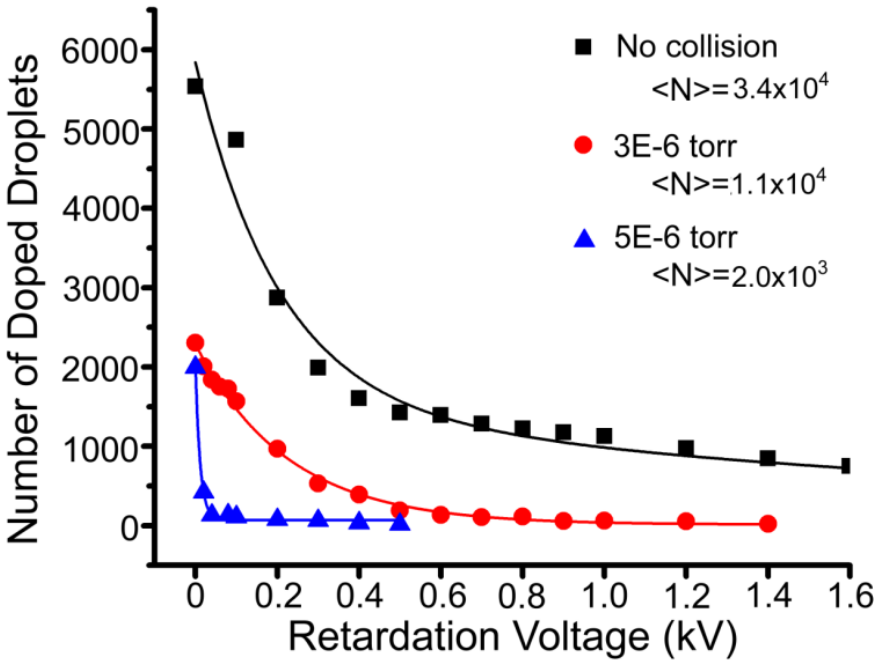

Fig.8.7. Size distribution of doped droplets from the retardation experiment. Without added collisions, the experimental data is fitted by a bi-exponential function. After collision, the data can be fitted by a single exponential function. The average sizes of the droplets are calculated based on the experimental data range only (no extrapolation to smaller and larger sized regions).

To measure the average size and size distribution of the doped droplets after collision, we performed the retardation experiment (Chapter 6 and 7). Since the bias voltages on both the collision cell and the flight tube are not fully understood, in this work, we grounded both to just observe the effect of collision. Fig. 8.7 shows the change in the number of doped droplets with the retardation voltage at different pressures in the collision cell. This experiment was performed with a new paste for the ion source, hence the number of doped droplets without added collision is now increased to 5500. After adding helium for collisions, this number decreases to 2400 at 3×10^{-6} Torr and 2000 at 5×10^{-6} Torr. Under all three conditions, the numbers of doped droplets decrease with increasing retardation voltages.

To evaluate the effectiveness of size reduction, we calculate the number of doped droplets in the size region below 1.2×10^5 atoms/droplet – the desired size for electron diffraction. Without the collision gas, the size distribution can be fitted by a bi-exponential function with an average size of 3.4×10^4 atoms/droplet. At 3×10^{-6} Torr and 5×10^{-6} Torr, both distributions can be fitted by a single exponential decay, with average sizes 1.1×10^4 atoms/droplet and 2.0×10^3 atoms/droplet. Table 8.1 lists the number of droplets within the desired size region for diffraction. Without added collisions, this number is about 3930, which accounts for 70% of total doped droplets. With increasing collision pressures, the fraction of the number of doped droplets in the desired size increases, but the actual number decreases. Similar results have also been obtained using either nitrogen or argon as collision partners.

Table.8.1 Total number of doped droplets and the number of doped droplets within the desired size range of $< 1.2 \times 10^5$ atoms under different conditions.

	No added collision	1.6×10^{-3} Torr	2.6×10^{-3} Torr
Total number of doped droplets	5536	2304	1994
Droplets in the desired range	3930	1912	1961
Experimental Ratio	71%	83%	98%
Calculated upper limit	1.2×10^5	2.8×10^5	4.8×10^5
Fitted lower limit	0	1.0×10^5	1.2×10^5
Calculated ratio	65%	78%	93%

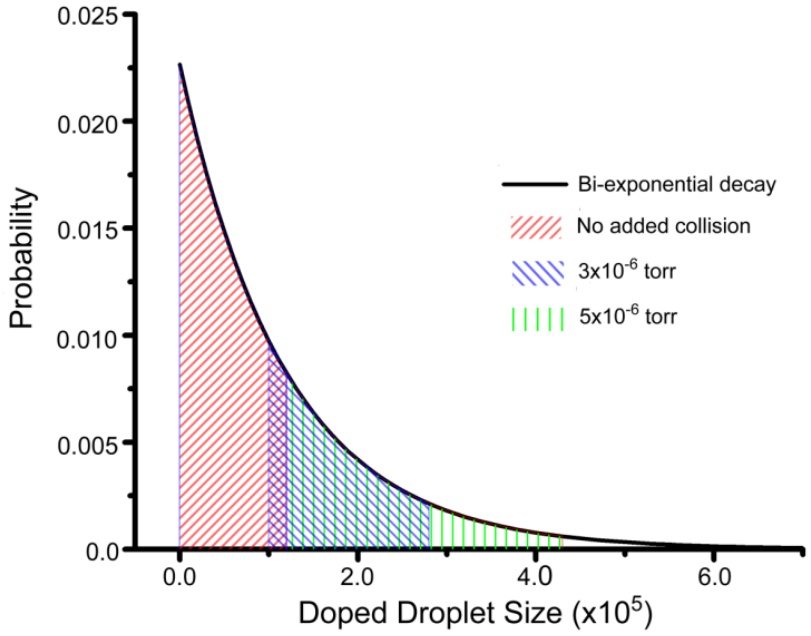

Fig. 8.8. Simulation results under three different pressures in the collision chamber.

The above results can be qualitatively reproduced by considering the physical parameters of the experiment. Without collision, the doped droplet beam could be fitted by a bi-exponential decay function as shown in Fig. 8.8. The red shaded region represents the doped droplets in the size range from 0 to 1.2×10^5, which accounts for 65% of total doped droplet. In the experiment, this ratio is about 70% as listed in Table 8.1. At a collision pressure of 1.6×10^{-3} Torr, some smaller sized droplets will be deflected and lost by collision, while some bigger sized droplets will shrink into the desired size range due to collisions. This upper size limit, "Calculated upper limit" in Table 8.1, can be obtained by solving Eq. 8.3. To find the lower limit, "Fitted lower limit" in Table 8.1, we used the ratio of the total number of transmitted droplets under the same collision pressure and the number of droplets with no added collisions (2^{nd} row of Table 8.1). From the experiment, only 42% (= 2304/5536) of the ion

doped droplets survived the collision process. Assuming 100% transmission for the doped droplets above the lower size limit, we should be able to reproduce this ratio by varying the lower size limit. We then calculated the number of droplets between the two limits and compared it with the total number of transmitted ions under the same collision pressure. The resulting ratios are about 78% at 1.6×10^{-3} Torr and 93% at 2.6×10^{-3} Torr, both of which are in qualitative agreement with those of the experimental data.

8.4 Conclusion and future work

In trying to reach a conclusion from the results of Table 8.1, we need to take into consideration the limited data and the limited scope of the experiment. From Fig. 8.7, the average sizes of the ion doped droplets in all three cases are below the desired upper limit, hence most of the ions from the current experiment are acceptable for electron diffraction. In this sense, the experiment can only serve as a guide for future tests with larger droplets after upgrading the cryostat. From Table 8.1, the fraction of small sized droplets can be substantially increased with increasing collisions, although the absolute number of ion doped droplets is reduced by ~50%. Based on this result, under the current setting, we should be better off by just selecting the small sized droplets in the original beam without any size reduction. However, based on the work of Chapter 6, the current setting of the droplet source (16 K) is not optimal for doping, and lower source temperatures and hence larger droplets are required for larger ions. It is therefore unclear at this stage how much larger the

droplets have to be for a green fluorescing protein, and if size reduction is necessary under optimal doping conditions.

We are currently in the process of updating the cryostat, the ion source, and the experimental design to further improve the ion count. A more powerful cryostat can produce larger droplets, and with the much improved range of sizes available from the upgrade, implementation of the collision cell with peptide ions and protein ions will be straightforward. In the meantime, we are also upgrading the ion source for a higher ion throughput under milder spraying processes. This upgrade is necessary for the introduction of proteins, the next step along the path of progress. Another concern of the current experimental design is the divergent effect of the system, which seems to have eliminated any enhancement by the bias voltage on the collision cell. Adding meshes on the entrance and exit apertures of the collision cell should remove any focusing or defocusing effect of the electrodes, simplifying the interpretation of the experimental data.

In collaboration with the Pacific Northwest National Laboratory, our next plan for the collision cell is to introduce an ion funnel as a means of size reduction.[4] An ion funnel consists of a stack of equally spaced ring electrodes with decreasing internal diameters. The electrodes are biased both with DC and RF voltages, and the net effect is focusing of the ion beam for efficient ion transmission. The operation of the ion funnel also requires buffer gases, which simultaneously functions as the collision. The exit gate of the ion funnel will be triggered by a pulsed signal for synchronization with the subsequent laser alignment and electron diffraction.

The result from this experiment needs to be interpreted in the context of electron diffraction. At a space charge limit of 10^7 ions/cm^3 and for an effective diffraction volume of 10^{-6} cm^3, only 10 ions are needed for diffraction. The current result, with and without the collisional size reduction, provides a sufficient platform for electron diffraction. On the other hand, more ions allow for more stringent size selection and focusing, hence more favorable conditions for electron diffraction. Hence the need for a strong ion source remains highly desired at this stage.

8.5 Reference

1. Zhang, J.; He, Y.; Freund, W. M.; Kong, W., Electron Diffraction of Superfluid Helium Droplets. *J. Phys. Chem. Lett.* **2014,** *5*, 1801-1805.
2. Gomez, L. F.; Loginov, E.; Sliter, R.; Vilesov, A. F., Sizes of large He droplets. *J. Chem. Phys.* **2011,** *135*, 154201/1-154201/9.
3. Clemmer, D. E.; Jarrold, M. F., Ion mobility measurements and their applications to clusters and biomolecules. *J. Mass Spectrom.* **1997,** *32*, 577-592.
4. Ryan R. Julian, S. R. M., and Martin F. Jarrold, Ion funnels for the masses: experiments and simulations with a simplified ion funnel. *J.Am.Soc.Mass Spectrom* **2005,** *16*, 1708-1712.

Chapter 9 Conclusion and Outlook

9.1 Conclusion

This thesis presents experiments on investigations of doping metal ions and mass-to-charge selected molecules into superfluid helium droplets. The goal is to embed much bigger species such as proteins or macromolecule assemblies into droplets for cryogenic cooling and thereby field induced alignment and orientation. Ultimately, the supercooled field aligned isolated molecules will be used in electron diffraction for structural determination.

The experimental setup involves a pulsed superfluid helium droplet source, two different types of ion sources, and two different types of size analyzers with two different detectors for ion doped droplets. Compared with the design of Falconer *et al*[1]., our system has tripled the ion count of the doped droplets, thanks to the grid surrounding the droplet beam. This multipass doping region has further enabled studies of the relation between kinetic energy and doping efficiency. Instead of storing ions in an ion trap,[2] our electrospray ionization source with the mass-selective capability has delivered extremely low energy ions of reserpine and substance P into helium droplets via a stopper electrode. By wiring a copper target to a big resistor of megaOhm or gigaOhm with an amplification circuit, we can measure the absolute number of ions independent of the mass of the charged species. For further amplification, we have also used a Daly-type dynode detector. The high sensitivities of these detectors have further enabled us to characterize the size of the doped

droplets by electrostatic deflection and reflection. This information is crucial in preparing the doping droplets for electron diffraction.

Throughout these exercises, we have developed models to interpret the experimental results and predict outcomes of future experiments with larger heavier species. Our ballistic model for the high speed cesium ions emphasizes the importance of decreasing the kinetic energy and increasing the droplet size for effective doping. Further extensions of this model to the extremely low energy ions from the ESI source have established a direct correlation between the residence time of the ions in the droplet beam and the doping efficiency. We therefore conclude that to maximize the production of ion doped droplets, large droplets and slow ions are the most preferred conditions.

Unfortunately, the above result is not ideal for the ultimate goal of electron diffraction since too many helium atoms surrounding a single dopant molecule could mask the diffraction signal from the dopant molecule. To obtain small size doped droplets ($<10^5$ helium atoms), we have devised a collisional control experiment. Limited by the deteriorating performance of our cryostat, the result from this experiment is still inconclusive. However, our preliminary data have indeed confirmed our calculation model.

9.2 Outlook

The logical step forward is to dope protein ions, such as green fluorescing proteins, into superfluid helium droplets for characterization. Composed of 238 amino

acids with a β barrel structure, GFP is much bigger and more complicated than reserpine and substance P. To accommodate the much larger heat capacity of GFP ions, we need to update our cyrostat therefore to cool down the droplet source to much lower temperatures for much larger droplets.

Once GFP is successfully doped into superfluid helium droplets, more experiments will ensue. A unique property of GFP is its green fluorescence after exposure to ultraviolet light. Therefore, observation of fluorescence after laser excitation is an indication of the conformation of GFP after ESI. The answer to this experiment bears extreme importance to this project and other relative fields including native protein mass spectrometry.[3-4]

Further effort is to use the fluorescence of GFP as an indicator of laser alignment. The principle of this experiment is linear dichroism in the gas phase.[5] A polarized laser can align the β barrel, and excitation by another UV laser should have different yields depending on the relative orientation between the transition dipole of the chromophore and the polarization direction of the laser. Consequently, after the alignment laser is off, the GFP ions should still remain largely aligned for the next few nanoseconds when the probe laser excites the chromophore. The yield of LIF should therefore be reflective of the degree of alignment in the alignment field. We try to avoid temporal overlap between the alignment laser and the probeo laser to avoid potential complications of mulitphoton effects between the two laser beams.

To further the experiment of collisional size reduction, we need to perform more measurements with larger sized clusters. In addition, we have also explored the

idea of implementing an ion funnel in place of the collision cell. An ion funnel consists of a stack of equally spaced ring electrodes with decreasing internal diameters. A voltage divider introduces a linear DC voltage gradient between electrodes and a RF voltage of equal amplitude but opposite phase is added to adjacent electrodes. The funnel is typically operated at a relatively higher pressure than an ion trap, and collisions with the ambient gas remove possible gains in kinetic energy during the transport through the funnel. Fig. 9.1 shows the results of 50 simulated ion trajectories through an ion funnel from Julian *et al*.[6] In the ring electrodes system with RF field, the ion confinement region can be divided into an effective field-free region and a strong field region. Most ions remain within the confines of the field-free region (inside the dash lines), because in this region, field contributions from each lens can be canceled out by the two adjacent lens. At a pressure range from several torr to ~50 millitorr, the calculated transmission efficiency is about 94%. The last two thick lines work as an exit of ion funnel and show the DC extraction region without RF field. To interface with the electron diffraction experiment, a trigger pulse can be applied on the exit electrode of the ion funnel, to synchronize with the alignment laser and electron beam.

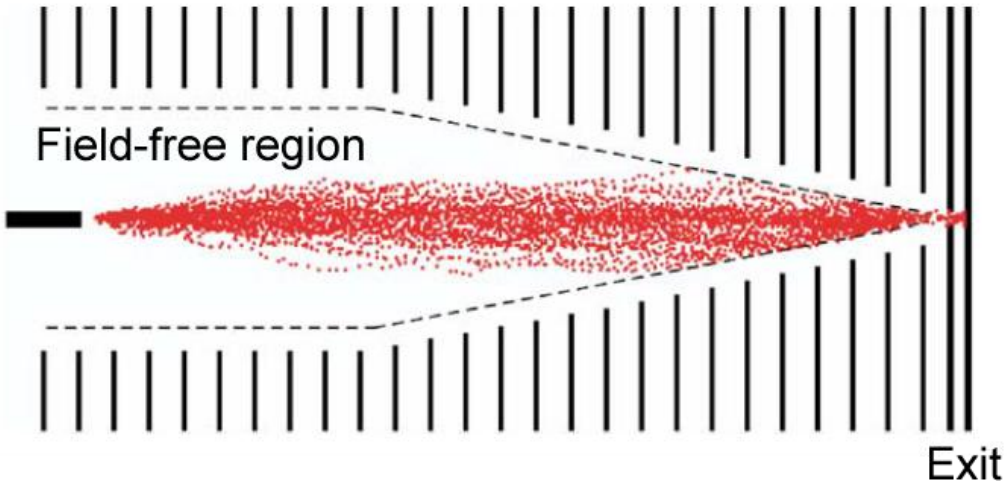

Fig.9.1. Simulation of ion trajectories through an ion funnel.[6]

9.3 Reference

1. Falconer, T. M.; Lewis, W. K.; Bemish, R. J.; Miller, R. E.; Glish, G. L., Formation of cold ion-neutral clusters using superfluid helium nanodroplets. *Rev. Sci. Instrum.* **2010,** *81*, 054101.
2. Bierau, F.; Kupser, P.; Meijer, G.; von Helden, G., Catching proteins in liquid helium droplets. *Phys. Rev. Lett.* **2010,** *105*, 133402.
3. van, d. H. R. H. H.; Heck, A. J. R., Native protein mass spectrometry: From intact oligomers to functional machineries. *Curr. Opin. Chem. Biol.* **2004,** *8*, 519-526.
4. Kaddis, C. S.; Loo, J. A., Native protein MS and ion mobility: Large flying proteins with ESI. *Anal. Chem.* **2007,** *79*, 1778-1784.
5. Kong, W.; Pei, L.; Zhang, J., Linear dichroism spectroscopy of gas phase biological molecules embedded in superfluid helium droplets. *Int. Rev. Phys. Chem.* **2009,** *28*, 33-52.
6. Ryan R. Julian, S. R. M., and Martin F. Jarrold, Ion funnels for the masses: experiments and simulations with a simplified ion funnel. *J.Am.Soc.Mass Spectrom* **2005,** *16*, 1708-1712.